DEUTSCHES ELEKTRONEN-SYNCHROTRON

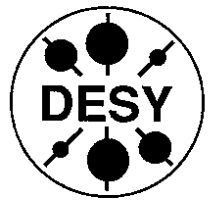

DESY 96-090
May 1996

The Partonic Structure of the Photon: Photoproduction at the Lepton-Proton Collider HERA

M. Erdmann

Physikalisches Institut, Universität Heidelberg

ISSN 0418-9833

NOTKESTRASSE 85 - 22607 HAMBURG

To be sure that your preprints are promptly included in the
HIGH ENERGY PHYSICS INDEX,
send them to (if possible by air mail):

DESY
Bibliothek
Notkestraße 85
22607 Hamburg
Germany

DESY-IfH
Bibliothek
Platanenallee 6
15738 Zeuthen
Germany

DESY 96-090
May 1996

ISSN 0418-9833

The Partonic Structure of the Photon: Photoproduction at the Lepton–Proton Collider HERA

Martin Erdmann

Universität Heidelberg, Physikalisches Institut

Philosophenweg 12, D-69120 Heidelberg

e-mail: erdmann@dice2.desy.de

to be published in Springer Tracts

Abstract

The knowledge of the interactions of photons with hadrons has considerably improved with the study of high energy lepton–proton collisions at HERA. The results on the partonic interactions of photons are summarized in comparison with photon–nucleon, two–photon, and proton–anti-proton experiments.

Contents

Part I

Introduction

The interaction of high energy photons with leptons is very well described by the electro-weak theory. The interaction with hadrons on the other hand is full of surprises and has developed into an interesting field of QCD.

The first generation of photon–nucleon fixed target scattering experiments revealed that to a very good approximation the photon behaves like a hadron which is quantitatively summarized by the Vector Meson Dominance Model (VDM) (for a review refer to [BAU-78]). In this model, the photon has a well defined probability of fluctuating into vector mesons with the quantum numbers of the photon, e.g. $\rho, \omega, \phi, ...$ with $J^{PC} = 1^{--}$ (Fig.1: vdm). The VDM gives relations between photon–nucleon and meson–nucleon reactions which are well satisfied in interactions with small transverse energy in the final state.

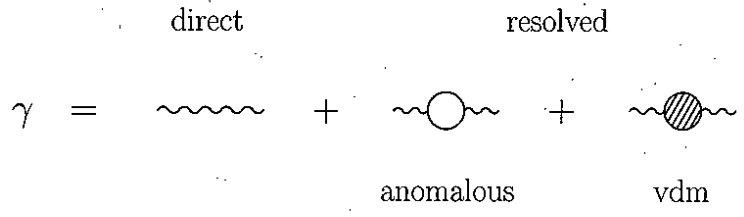

Figure 1: Different states of the photon are shown: apart from the bare photon state (direct), the photon can fluctuate into quark–anti-quark pairs without forming a hadronic bound state (anomalous), or form a vector meson (vdm). The photon can interact therefore directly, or through its resolved states.

The advent of QCD theory gave interesting and significant modifications to the VDM and its predictions. QCD predicts processes where the photon couples directly to quarks leading to hard parton scattering and jets in the final state (Figs.1, 2). The measurement of these processes was the goal of several fixed target experiments at CERN and FNAL with center of mass (CM) energies up to $\sqrt{s_{\gamma p}} = 27$ GeV (for a review refer to [PAU-91]). They found significant deviations from the VDM model by observing an excess of final state hadrons with large transverse momenta which can be quantitatively explained by direct photon–nucleon interactions. Also in recent years evidence for jet structure in the final state was reported [E683-94]. The CM energy was however too small to make definite QCD tests.

A second QCD prediction is that at sufficiently high transverse energy $q\overline{q}$ fluctuations without the formation of a hadronic bound state will dominate the vector meson contribution (Fig.1: anomalous). These contributions can be quantitatively calculated within perturbative QCD, e.g. the photon structure function for the anomalous part is predicted. The existence of the

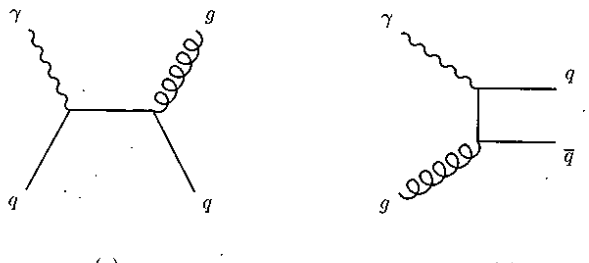

Figure 2: Diagrams of direct photon–nucleon interactions are shown in leading order QCD: a) the QCD Compton and b) the photon-gluon-fusion processes.

anomalous coupling was first shown in measurements of the photon structure function. This was achieved in two photon reactions at the e^+e^- colliders (Fig.3) at PETRA/PEP (for reviews refer to [KOL-84, BER-87, KOL-87]) and recently at TRISTAN and LEP. Hard scattering reactions involving resolved photons were observed in the interactions of two quasi-real photons by the measurement of particles with large transverse momentum and jet formation (TRISTAN and LEP).

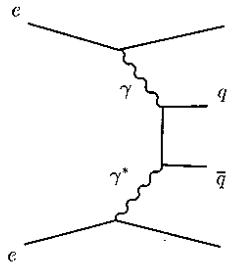

Figure 3: Deep inelastic electron–photon scattering: a highly virtual photon γ^* ($Q^2 \gg 1$ GeV^2) probes the quark content of a quasi-real photon γ ($Q^2 \approx 0$ GeV^2).

The new HERA ep collider has been operational since 1992. This facility offers the possibility of studying photon–proton interactions at CM energies up to 300 GeV which is an order of magnitude larger than in fixed target experiments so far (Fig.4). At these energies, the total γp cross section is still dominated by processes where the photon fluctuates into a vector meson (Fig.5). A fraction of the events shows hard γp scattering processes which manifest themselves in jets with high transverse energies. Both the direct photon and the resolved photon interactions

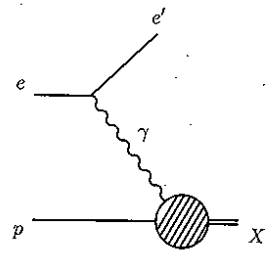

Figure 4: The photoproduction regime in lepton–proton scattering corresponds to quasi-real photons ($Q^2 \approx 0$ GeV^2) interacting with protons.

can be extensively studied and quantitatively compared to QCD predictions. The parton content of the photon – gluons and quarks – can be probed.

This review summarizes the HERA results from the first four years on the parton interactions of quasi-real photons and puts them in relation to the results from other experiments.

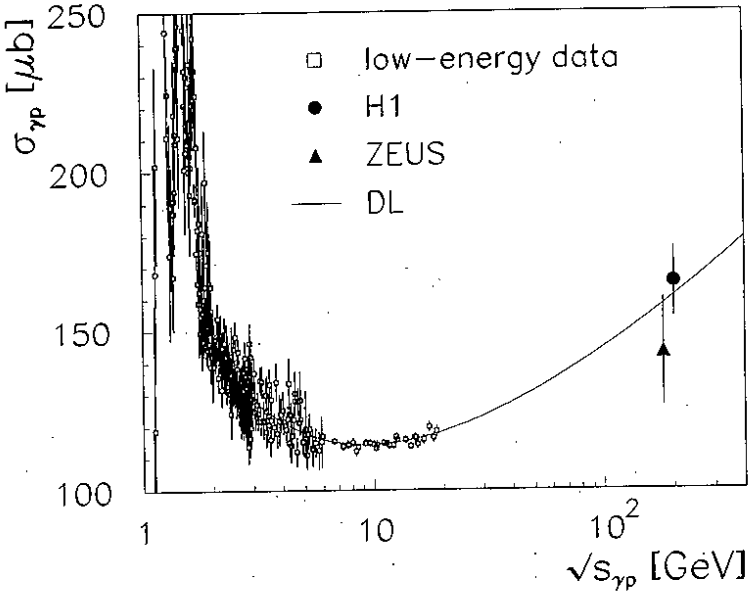

Figure 5: Measurements of the total photon–proton cross section at different center of mass (CM) energies (full circle: H1 [H1-95E], full triangle: ZEUS Collab. [ZEU-94A], open squares: fixed target data [BAL-88]). The energy dependence is compatible with the same moderate rise towards high CM energies as found in hadron-hadron total cross section measurements (full curve from [DON-92]).

Part II

Predictions for hard photon interactions

In this section we want to introduce predictions for photon–target interactions which involve constituents of the photon and a target particle which can be e.g. a nucleon or another photon. In current experiments, the photons are produced by highly energetic leptons. The photons carry fractional energies

$$0 < y \equiv \frac{\gamma\tau}{e\tau} = 1 - \frac{E_{e'}}{E_e}\cos^2(\frac{\theta_e}{2}) < 1 \qquad (1)$$

Here e and τ are the four vectors of the beam lepton and the target particle, and γ is the photon four vector (Fig.4). The lepton beam energy is denoted by E_e, and $E_{e'}$ (θ_e) is the energy (angle) of the scattered lepton. The squared four momentum of the photon is negative, and can be calculated from

$$0 < -\gamma^2 = -(e-e')^2 \equiv Q^2 = 4\,E_e E_{e'}\sin^2(\frac{\theta_e}{2}) \qquad (2)$$

Q^2 is the virtuality of the photon. The topics, which we want to discuss in the following sections, are:

1. How many photons are radiated by the electrons ?
2. How long does a fluctuation of the photon into a quark–anti-quark pair last ?
3. What are the predictions for the direct and resolved photon contributions ?
4. Which predictions exist for particle and jet production in photon-target interactions ?

1 Photons

1.1 Time of $e \to e\gamma$ and $\gamma \to q\bar{q}$ fluctuations

A typical time of a quark–anti-quark fluctuation of a highly energetic real photon is in the rest frame of a target nucleon large compared to the size of the nucleon. At e^+e^- and ep colliders the photons are emitted by the leptons which implies a two step process for the creation of a $q\bar{q}$ pair: first, the electron fluctuates into an electron–photon state $e\gamma$, then the photon fluctuates into a $q\bar{q}$ pair. As a result of the Heisenberg uncertainty relation [1],

$$\Delta t \approx 1/\Delta E, \qquad (3)$$

the life time $t(e \to e\gamma)$ of the electron–photon state is required to be larger than that of the $\gamma \to q\bar{q}$ fluctuation.

In the target rest frame the time of fluctuation can be calculated from the uncertainty relation and relativistic kinematics (for a review see e.g. [HOY-95]). The energy difference between the

[1] The convention $\hbar = c = 1$ is used for convenience.

initial state i with energy E_i and the state f of the fluctuation with constituents j and total energy E_f is given by

$$E_f - E_i = \frac{1}{2E_i}\left(\sum_j \frac{m_j^2 + p_{t,j}^2}{z_j} - m_i^2\right) \tag{4}$$

where longitudinal particle momenta are large compared to the transverse momenta. m_i and m_j are the masses of the initial particle and of the constituents. The transverse momenta $p_{t,j}$ of the constituents and their energy fractions z_j are measured with respect to the initial state particle. In the following we discuss several applications of eq.(4):

1. By emission of a highly virtual photon ($Q^2 \gg 1$ GeV^2) from an electron, transverse momenta are generated according to $p_{t,\gamma}^2 = Q^2(1-y)$. Such $e\gamma$ fluctuations require the energy

$$E_{e\gamma} - E_e = \frac{1}{2E_\gamma}Q^2. \tag{5}$$

The corresponding time of fluctuation for $E_\gamma = 1$ TeV and $Q^2 = 400$ GeV^2 is $t(e \to e\gamma) = 1$ fm (Fig.6a: full curve)[2].

2. The emission of a quasi-real photon (virtuality $Q^2 \approx 0$ GeV^2) by an electron involves no transverse momentum in the collinear limit. The energy requirement for the $e\gamma$ fluctuation is

$$E_{e\gamma} - E_e = \frac{1}{2E_\gamma}\frac{m_e^2 y^2}{1-y} \tag{6}$$

where E_e is the initial energy of the electron with mass m_e, and y is the energy fraction carried by the photon which is here $y = E_\gamma/E_e$. The ratio

$$Q_{min}^2 \equiv \frac{m_e^2 y^2}{1-y} \tag{7}$$

gives the smallest virtuality of photons which are generated by electrons: $Q_{min}^2 \approx 10^{-7}$ GeV^2. At photon energies of $E_\gamma = 1$ TeV the time of an $e\gamma$ fluctuation is $t(e \to e\gamma) \approx 4$ μm (Fig.6a: full curve).

3. Fluctuations of the photon into a $q\bar{q}$ pair depend on the energy fraction x_γ which is carried by the quark relative to the photon energy E_γ. For quasi-real photons the required energy is

$$E_{q\bar{q}} - E_\gamma = \frac{1}{2E_\gamma}\frac{m_q^2 + p_{t,q}^2}{x_\gamma(1-x_\gamma)} \tag{8}$$

where m_q and $p_{t,q}$ are the mass and transverse momentum of the (anti-) quark (Fig.6b). Symmetric configurations between the quark and anti-quark, i.e. $x_\gamma = 0.5$, give the longest life time for such a $q\bar{q}$ state. Using light quarks with small $p_{t,q}$, e.g. setting $m_q^2 + p_{t,q}^2 = \Lambda_{QCD}^2$, and a symmetric energy sharing at $E_\gamma \doteq 1$ TeV results in a time $t(\gamma \to q\bar{q}) = 1000$ fm for the fluctuation [dotted curves in Fig.6: a) $Q^2 < 10^{-2}$, b) $x_\gamma = 0.5$].

[2] In deep inelastic electron–nucleon scattering the time of an $e\gamma$ state can also be expressed by the momentum fraction x_{Bj} of the struck parton of the proton. Using $x_{Bj} = Q^2/(2m_N E_\gamma)$ results in $t(e \to e\gamma) = (m_N x_{Bj})^{-1} \equiv 2L_i$, where m_N is the mass of the nucleon, and L_i is the so-called Ioffe length. A parton momentum fraction $x_{Bj} = 0.2$ corresponds to $t(e \to e\gamma) = 1$ fm. Within this time, a subsequent fluctuation $\gamma \to q\bar{q}$ can happen.

As mentioned above, the formation of a $q\bar{q}$ pair from an electron via a photon is only allowed, if the time of the $q\bar{q}$ fluctuation lies within the life time of the $e\gamma$ state. At large $Q^2 \gg 1$ GeV^2 the time $t(\gamma \to q\bar{q})$ is therefore limited by the time $t(e \to e\gamma)$ (Fig.6a: dotted and full curves).

4. A subsequent formation of a gluon from the (anti-) quark $q \to qg$ has a lifetime which is suppressed by the energy fraction x_γ of the quark relative to the photon, and the quark energy fraction z which is taken by the gluon: $x_\gamma \cdot z(1-z)$. Using $x_\gamma = 0.5$ and an asymmetric energy share between the quark and the massless gluon of $z = 0.1$, results in a life time which is 20 times shorter than the $\gamma \to q\bar{q}$ fluctuation.

At HERA $q\bar{q}$ fluctuations from quasi-real photons, measured relative to the proton rest frame, typically last $t > 10^4$ fm. The time of fluctuation involving gluons are $1-2$ orders of magnitude shorter than the quark fluctuations.

1.2 The Equivalent Photon Approximation

How many quasi-real photons are emitted by electrons, and what is the energy spectrum of these photons ? These questions can be answered, e.g. by calculating electron-nucleon scattering in the Equivalent Photon Approximation (EPA) (e.g. [BUD-75]). The field of a fast charged particle is similar to electromagnetic radiation. This radiation may be interpreted as a flux of photons with energy distribution $n(y)$ where y denotes the energy fraction of the photons relative to the electron energy. Electromagnetic electron–nucleon scattering can therefore be reduced to photon–nucleon interactions:

$$d\sigma_{eN}(y, Q^2) = \sigma_{\gamma N}(y)\; dn(y, Q^2) \tag{9}$$

where $\sigma_{\gamma N}$ is the total photo-absorption cross section, and Q^2 is the virtuality of the photons.

The first photon spectra were calculated by Weizsäcker and Williams [WEI-34, WIL-35], neglecting the virtuality of the photon and terms involving the longitudinal photon polarization. This approximation is usually referred to as Weizsäcker–Williams–Approximation (WWA). Integrating the emission of quasi-real photons in a large interval $Q_{min}^2 \le Q^2 \le Q_{max}^2 \ll 1$ GeV^2 and in a small energy bin dy, the equivalent number of photons is

$$dn(y, Q_{max}^2) = f_{\gamma/e}(y, Q_{max}^2)\; dy \tag{10}$$

with

$$f_{\gamma/e} = \frac{\alpha}{2\pi}\left(\frac{1+(1-y)^2)}{y}\ln\frac{Q_{max}^2}{Q_{min}^2} - 2m_e^2 y\left(\frac{1}{Q_{min}^2} - \frac{1}{Q_{max}^2}\right)\right). \tag{11}$$

Here α is the fine structure constant and $Q_{min}^2 \equiv m_e^2 y^2/(1-y)$ is the kinematic lower limit shown in equation (7).

In Fig.7 the energy spectrum of quasi-real photons, emitted by electrons, is shown for $Q_{max}^2 = 0.01$ GeV^2. The number of photons decreases at large photon energies $y > 0.2$ by an order of magnitude, but rises steeply towards small photon energies $y < 0.2$.

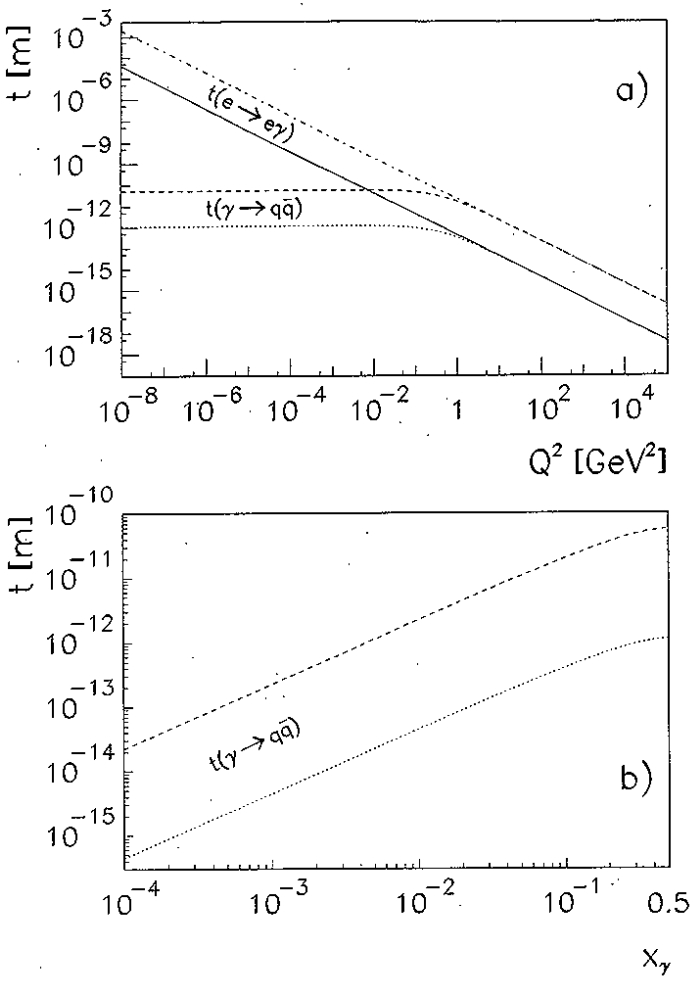

Figure 6: a) The time of a $e \to e\gamma$ fluctuation, as measured in a target rest frame, is shown as a function of the virtuality Q^2 of the photon for the photon energies $E_\gamma = 1$ TeV (full curve) and $E_\gamma = 50$ TeV (dash-dotted curve). The dotted (dashed) curve indicates the time of a subsequent $\gamma \to q\bar{q}$ fluctuation for $E_\gamma = 1$ TeV (50 TeV) with a symmetric energy sharing between the $q\bar{q}$ pair and $m_q^2 + p_{t,q}^2 = \Lambda_{QCD}^2$.
b) The time of a $\gamma \to q\bar{q}$ fluctuation depends on the energy fraction x_γ carried by the quark: the dotted (dashed) curve represents the fluctuation of a quasi-real photon, i.e. $Q^2 \approx 0$, into a $q\bar{q}$ pair at the photon energy $E_\gamma = 1$ TeV (50 TeV). Here again we set $m_q^2 + p_{t,q}^2 = \Lambda_{QCD}^2$.

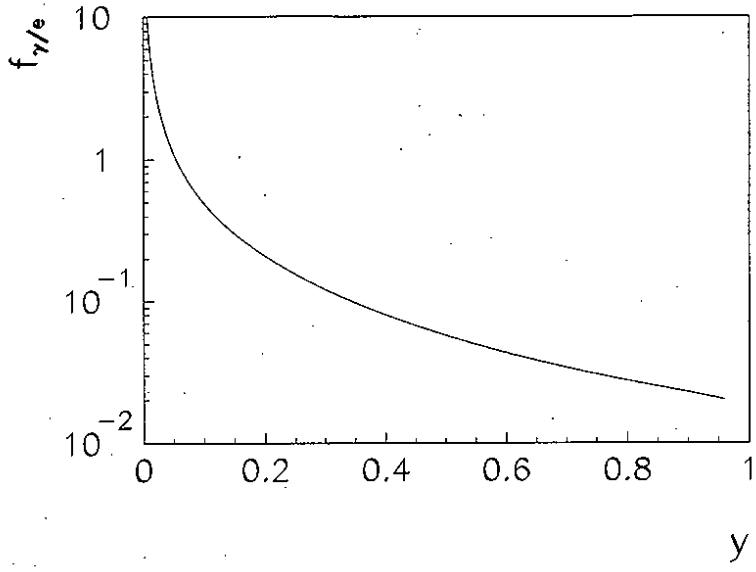

Figure 7: The energy spectrum of quasi-real photons, emitted by electrons, is shown as a function of the scaled photon energy $y = E_\gamma/E_e$ for a maximum virtuality $Q_{max}^2 = 0.01$ GeV^2.

The accuracy of the WWA has been studied for many different processes (see e.g. [BUD-75]). In the case of photoproduction of at HERA, the accuracy has been calculated, e.g., for the QED Compton process at large transverse photon momenta $p_T > 10$ GeV [BAW-89]. For events where the electron is tagged at small scattering angles in the laboratory $1 \leq \theta \leq 10$ mrad, the WWA is better than 1%. For jet production with transverse jet energies $E_t^{jet} \gg \sqrt{Q^2}$ and untagged electrons with $Q^2 < 4$ GeV^2, corrections to the WWA are at the few percent level [KLA-95A].

1.3 The photon structure function F_2^γ

The splitting of a photon into a quark-antiquark pair can be calculated in the Quark Parton Model (QPM). For a more complete discussion see e.g. [BER-87]. When a photon splits into a $q\bar{q}$ pair the quark carries an energy fraction x_γ, measured relative to the photon energy. Since the quark and anti-quark densities in the photon should be symmetric, and their momentum fractions are coupled in every process, a simple inverse relation holds for the probability of

finding a quark in the photon $f_{q/\gamma}$, and the probability of finding a photon in a quark $f_{\gamma/q}$ [GRI-71, CHE-75, BRO-79]:

$$f_{q/\gamma}(x_\gamma) = x_\gamma \; f_{\gamma/q}(1/x_\gamma) \tag{12}$$

The functional form of $f_{\gamma/q}$ is the same as that of $f_{\gamma/e}$ given in equation (11), scaled by the square of the quark charge e_q (ignoring the correction term $2m_e^2 y(1/Q^2_{min} - 1/Q^2_{max})$):

$$f_{q/\gamma}(x_\gamma) = e_q^2 \; \frac{\alpha}{\pi} \; \left(x_\gamma^2 + (1-x_\gamma)^2\right) \cdot \ln \frac{Q^2}{m_q^2} \tag{13}$$

Here m_q is a measure of the mass of 'free' quarks. A measurement of the analogous QED process $f_{\mu/\gamma}$ resulted in a precise determination of the μ mass [TPC-84]. To compare with experiments, the probabilities $f_{q/\gamma}$ are summed over all colours and flavours resulting in a prediction for the photon structure function F_2^γ:

$$F_2^\gamma(x_\gamma, Q^2) \;=\; 2\, x_\gamma \sum_{n_c, n_f} e_q^2 \; f_{q/\gamma}(x_\gamma, Q^2) \tag{14}$$

$$F_2^\gamma(x_\gamma, Q^2)\,[QPM] \;=\; 3 \sum_{n_f} e_q^4 \; \frac{\alpha}{\pi} \; x_\gamma \; \left(x_\gamma^2 + (1-x_\gamma)^2\right) \; \ln \frac{Q^2}{m_q^2}. \tag{15}$$

This QPM photon structure function F_2^γ has three features which are different from hadronic structure functions:

- The quark charges e_q contribute to the fourth power, compared to quadratic contributions in hadronic structure functions.
- The photon structure function increases with increasing energy fraction x_γ of the quark from the photon.
- The structure function of the quasi-real photon depends directly on the scale Q^2 at which it is probed by a highly virtual photon. In hadronic structure functions, Q^2 enters only via the QCD evolution equations.

QCD corrections to the simple QPM photon structure function can be calculated e.g. from the DGLAP evolution equations.These evolution equations are inhomogeneous for the quark distributions of the photon to account for the pointlike coupling of the photon to quarks (first term on right hand side in eq.(16)):

$$\frac{df_{q/\gamma}(x_\gamma, Q^2)}{d \ln Q^2} = \frac{\alpha}{2\pi} e_q^2 P_{q\gamma}(x_\gamma) + \frac{\alpha_s(Q^2)}{2\pi}\Big[P_{qq}(x_\gamma) \otimes f_{q/\gamma}(x_\gamma, Q^2) + P_{qg}(x_\gamma) \otimes f_{g/\gamma}(x_\gamma, Q^2)\Big] \tag{16}$$

$$\frac{df_{g/\gamma}(x_\gamma, Q^2)}{d \ln Q^2} = \frac{\alpha_s(Q^2)}{2\pi}\left[2P_{gq}(x_\gamma) \otimes \sum_{n_f} f_{q/\gamma}(x_\gamma, Q^2) + P_{gg}(x_\gamma, n_f) \otimes f_{g/\gamma}(x_\gamma, Q^2)\right] \tag{17}$$

Here P_{ij} denote the splitting functions, e.g. $P_{q\gamma}$ gives the probability of the photon radiating a quark. The sum runs over all quark flavours n_f. The convolution integral is defined as $a(x_\gamma) \otimes b(x_\gamma) = \int_{x_\gamma}^1 (dy/y) a(x_\gamma/y) b(y)$.

It is non-trivial that these QCD corrections preserve the $\ln Q^2$ dependence of the QPM photon structure function (eq. (15)). The leading order QCD prediction for the photon structure function is given by [WIT-77]

$$F_2^\gamma(x_\gamma, Q^2) = 3 \sum_{n_f} e_q^4 \; \frac{\alpha}{\pi} \; x_\gamma \; \left(x_\gamma^2 + (1-x_\gamma)^2\right) \; \ln \frac{Q^2}{\Lambda^2_{QCD}}. \tag{18}$$

Equation (18) accounts for the pointlike/anomalous photon contribution. Note that possible bound states between the quark and the anti-quark are not included.

Since the strong coupling constant is to first order $\alpha_s \propto (\ln Q^2/\Lambda^2_{QCD})^{-1}$ the photon structure function (18) is proportional to the ratio of the electromagnetic and strong coupling constants:

$$F_2^\gamma(x_\gamma, Q^2) \propto \frac{\alpha}{\alpha_s} \tag{19}$$

The photon structure function F_2^γ can be directly measured by deep inelastic electron-photon scattering experiments which could, in principle, give a precise determination of the QCD parameter Λ_{QCD}, or α_s respectively. Their measurements show that the anomalous photon processes cannot be separated from non-perturbative effects. The results of the experiments will be discussed in part III.

1.4 The Vector Meson Dominance Model

A very different ansatz to describe the photon and its interactions was postulated in the so-called Vector Meson Dominance Model (VDM): photons are essentially in a hadronic state when they interact with a target particle τ. The photoproduction cross sections were set proportional to the sum of vector-meson–target cross sections [SAK-60]:

$$\sigma_{\gamma\tau} = \sum_{V=\rho,\omega,\phi\ldots} \frac{\pi\,\alpha}{\gamma_V^2} \; \sigma_{V\tau} \tag{20}$$

The photon cross sections are suppressed by α. The photon–vector-meson coupling constants γ_V can be extracted from meson decay experiments.

The VDM model successfully describes photon–target interactions which are dominated by soft collisions. e.g. total cross section measurements. In hard interactions involving photons the label 'vdm' is synonymous with that part of resolved photon interactions where the quark–anti-quark pair of the photon forms a hadronic bound state before the scattering process.

Summary: photons

- At the ep and e^+e^- colliders, quasi-real photons are emitted by the leptons where the rate of these photons can be calculated with good accuracy by the Equivalent Photon Approximation.
- In the target rest frame the time of a $\gamma \to q\bar{q}$ fluctuation is very large compared to the size of a nucleon. Such partonic states lead to resolved photon interactions.

- Two extreme views of the resolved photon exist:
  1. The photon fluctuates into a hadron (Vector Meson Dominance Model).
  2. The quark and anti-quark propagate without forming a hadronic bound state: perturbative QCD predicts the distributions of quarks and gluons in the photon (anomalous resolved photon).
- Since the time of $\gamma \to q\bar{q}$ fluctuations is finite, also direct interactions of the photons with partons of a target particle should exist.

2 The QCD description of photon interactions

2.1 QCD predictions for parton scattering processes

The cross sections of elastic parton–parton scattering processes are predicted by QCD theory. For given initial state parton energies E_1, E_2, the distribution of the scattering angle $\hat{\theta}$ in the parton center of mass system are calculated (Fig.8). The results are usually presented in terms of the Lorentz invariant Mandelstam variables $\hat{s}, \hat{t}, \hat{u}$ which are for massless partons directly related to the parton energies and the scattering angle:

$$\hat{s} = 4E_1E_2 \tag{21}$$

$$\hat{t} = -\frac{\hat{s}}{2}\left(1-\cos\hat{\theta}\right) \tag{22}$$

$$\hat{u} = -\frac{\hat{s}}{2}\left(1+\cos\hat{\theta}\right) \tag{23}$$

The differential parton cross sections can be written in the form

$$\frac{d\hat{\sigma}}{d\hat{t}} = \frac{|M|^2}{16\pi\ \hat{s}^2} \tag{24}$$

with the matrix elements M of massless partons listed in Tab. 1 [LEV-92, KOL-84]. The corresponding Feynman diagrams are shown in Figs.2,3,9. Only two of the Mandelstam variables are independent of each other ($\hat{s}+\hat{t}+\hat{u}=0$). E.g., for a given parton CM energy $\sqrt{\hat{s}}$ the cross sections vary only with the parton scattering angle $\hat{\theta}$.

In Fig.10 the matrix elements are shown as a function of $\cos\hat{\theta}$. In the $\hat{\theta} = 90°$ scattering region, the matrix elements differ by three orders of magnitude. The dominant parton cross section results from gluon-gluon scattering $gg \to gg$. Most of the matrix elements diverge at $\cos\hat{\theta} = 1$ (-1) which corresponds to small angle forward (backward) scattering.

Since forward and backward scattering cannot be distinguished by the experiments in practice, only the absolute value of $\cos\hat{\theta}$ is relevant. In Fig.11 the shape of the matrix elements are shown as a function of $|\cos\hat{\theta}|$ for the direct photon processes and the resolved photon processes with the largest parton cross sections. The rise of the resolved photon processes is similar. However, the resolved processes are predicted to rise more steeply than the direct photon processes. In terms of the transverse parton momentum

$$\hat{p_t} = \frac{\sqrt{\hat{s}}}{2}\sin\hat{\theta}, \tag{25}$$

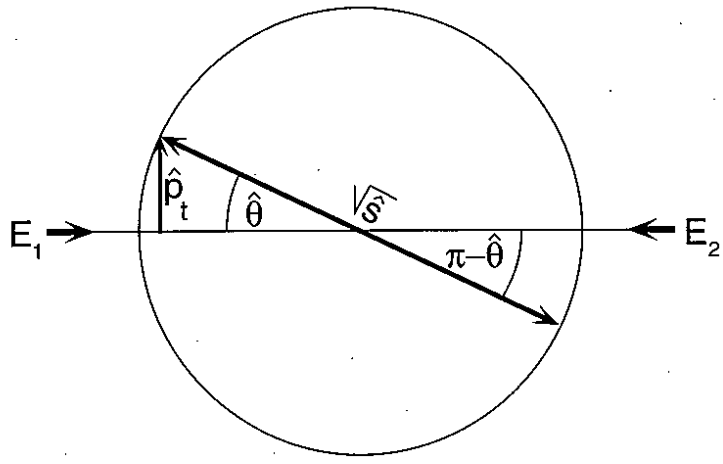

Figure 8: An elastic parton scattering process is shown in the parton-parton center of mass system. The center of mass energy is denoted by $\sqrt{\hat{s}}$, the scattering angle is $\hat{\theta}$, and $\hat{p_t}$ is the transverse momentum of the scattered partons.

the relative contribution of the direct processes to the total cross section increases with $\hat{p_t}$.

The renormalization scale μ_{ren} of the strong coupling constant α_s is set proportional to the transverse momentum $\hat{p_t}$ of the final state partons. Since α_s has to be small for reliable predictions of perturbative QCD, the parton transverse momentum has to be above some minimum value, usually set to about $\hat{p_t} = 2$ GeV. The small $\hat{p_t}$ region corresponds to the region where the majority of the parton cross sections diverge, that is at small (very large) scattering angles (eq.(25)). A lower cut-off in $\hat{p_t}$ therefore simultaneously solves the divergency problem and guarantees small α_s. The drawback is that predictions of perturbative QCD are restricted to the region of large transverse energies produced in the final state.

2.2 Leading order QCD predictions for jet and particle cross sections

To predict observable cross sections for parton scattering processes in lepton–target interactions involving quasi-real photons, the initial state parton luminosity and the final state parton fragmentation to hadrons or jets need to be known.

- Parton luminosity:
  1. The electrons radiate $f_{\gamma/e}(y,Q^2)dy$ photons with scaled energy $0 < y < 1$ and photon virtuality Q^2. Here the Weizsäcker-Williams Approximation, equation (11), can be used with high accuracy for sufficiently small $Q^2_{max} \ll 1$ GeV^2.

process	$\lvert M\rvert^2/\pi^2$
$qq' \to qq' = q\bar{q}' \to q\bar{q}'$	$\frac{64}{9}\alpha_s^2\left(\frac{\hat{s}^2+\hat{u}^2}{\hat{t}^2}\right)$
$qq \to qq$	$\frac{64}{9}\alpha_s^2\left(\frac{\hat{s}^2+\hat{u}^2}{\hat{t}^2}+\frac{\hat{s}^2+\hat{t}^2}{\hat{u}^2}-\frac{2}{3}\frac{\hat{s}}{\hat{u}\hat{t}}\right)$
$q\bar{q} \to q'\bar{q}'$	$\frac{64}{9}\alpha_s^2\left(\frac{\hat{t}^2+\hat{u}^2}{\hat{s}^2}\right)$
$q\bar{q} \to q\bar{q}$	$\frac{64}{9}\alpha_s^2\left(\frac{\hat{s}^2+\hat{u}^2}{\hat{t}^2}+\frac{\hat{t}^2+\hat{u}^2}{\hat{s}^2}-\frac{2}{3}\frac{\hat{u}}{\hat{s}\hat{t}}\right)$
$q\bar{q} \to gg$	$\frac{128}{3}\alpha_s^2\left(\frac{4}{9}\frac{\hat{t}^2+\hat{u}^2}{\hat{t}\hat{u}}-\frac{\hat{u}^2+\hat{t}^2}{\hat{s}^2}\right)$
$qg \to qg$	$16\alpha_s^2\left(\frac{\hat{s}^2+\hat{u}^2}{\hat{t}^2}-\frac{4}{9}\frac{\hat{s}^2+\hat{u}^2}{\hat{s}\hat{u}}\right)$
$gg \to q\bar{q}$	$\frac{8}{3}\alpha_s^2\left(\frac{1}{3}\frac{\hat{t}^2+\hat{u}^2}{\hat{t}\hat{u}}-\frac{3}{4}\frac{\hat{t}^2+\hat{u}^2}{\hat{s}^2}\right)$
$gg \to gg$	$72\alpha_s^2\left(3+\frac{\hat{t}^2+\hat{u}^2}{\hat{s}^2}+\frac{\hat{s}^2+\hat{u}^2}{\hat{t}^2}+\frac{\hat{s}^2+\hat{t}^2}{\hat{u}^2}\right)$
$\gamma q \to qg$	$\frac{128}{3}\alpha_s\alpha\, e_q^2\left(-\frac{\hat{u}}{\hat{s}}-\frac{\hat{s}}{\hat{u}}\right)$
$\gamma g \to q\bar{q}$	$16\alpha_s\alpha\, e_q^2\left(\frac{\hat{u}}{\hat{t}}+\frac{\hat{t}}{\hat{u}}\right)$
$\gamma\gamma \to q\bar{q}$	$\frac{1}{8}\alpha^2\, e_q^4\left(\frac{\hat{t}+\hat{u}}{\hat{t}\hat{u}}\right)$

Table 1: Leading order QCD matrix elements are listed for resolved (upper 9) and direct (lower 3) photon–nucleon and two–photon scattering processes. The matrix elements for direct interactions are the QCD Compton, the photon-gluon fusion, and the Quark Parton Model processes.

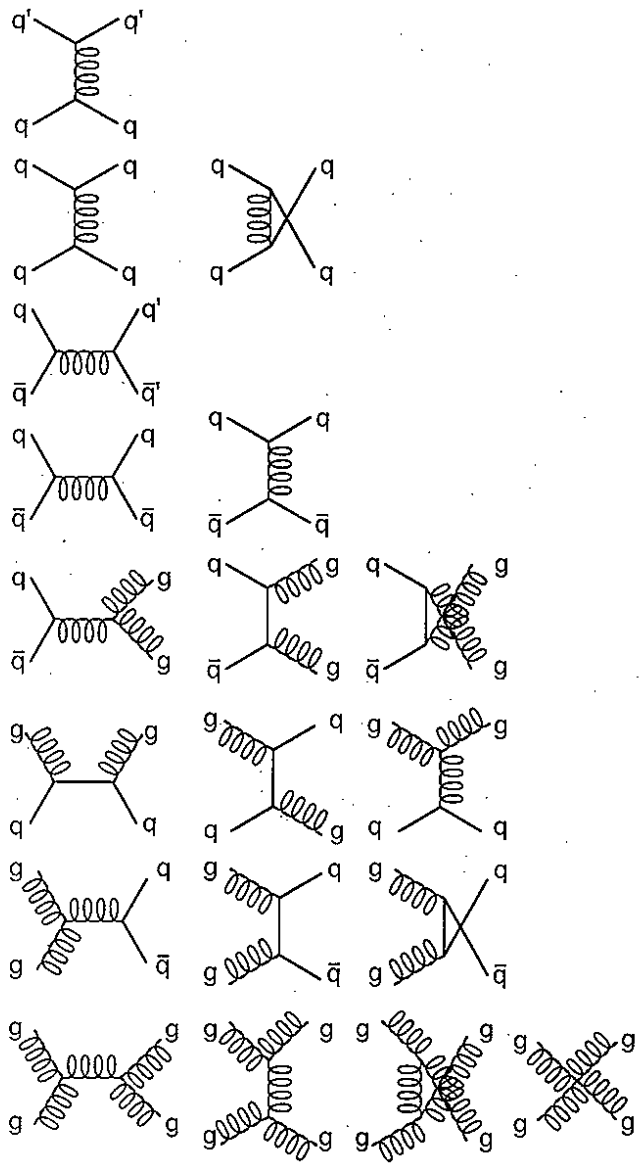

Figure 9: Leading order QCD diagrams for resolved photon–nucleon and double resolved two-photon scattering [LEV-92].

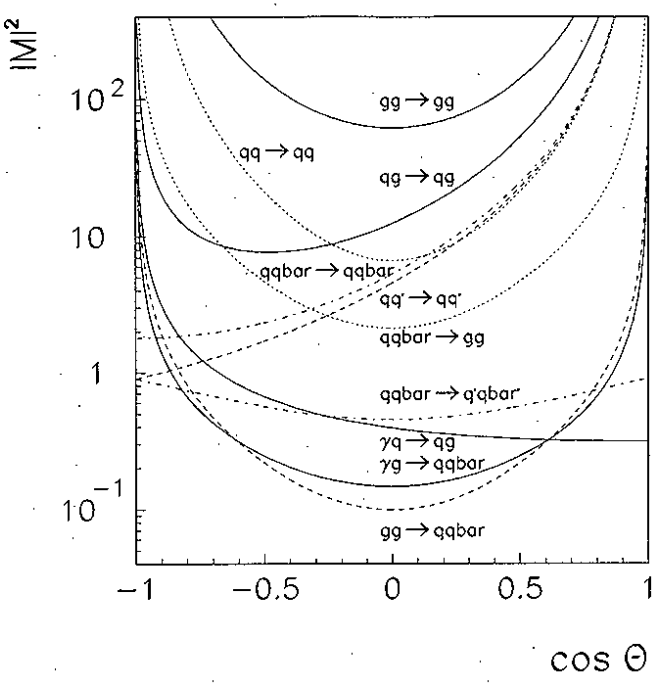

Figure 10: Distributions of the cosine of the parton scattering angle $\hat{\theta}$ in the parton-parton center of mass system are shown for different LO QCD matrix elements.

2. The parton distribution functions of the photon $f_{i/\gamma}(x_\gamma, \mu_{fac})$ are given as functions of the scaled parton energy $x_\gamma = E_{parton}/E_\gamma$, and the factorization scale μ_{fac}. The factorization scale μ_{fac} is usually set equal to the renormalization scale μ_{ren}. If non-perturbative bound state effects in the fluctuations of the photons into $q\bar{q}$ pairs are negligible, the anomalous photon contribution of equation (18) can be applied. For most applications the hadronic photon contributions are important and parameterizations of $f_{i/\gamma}$, extracted from experimental results, must be used. Their accuracy will be discussed in part III.
3. The parton distribution functions of the target particle $f_{j/\tau}(x_\tau, \mu_{fac})$ are required as functions of the scaled parton energy $x_\tau = E_{parton}/E_\tau$, and the factorization scale μ_{fac}.

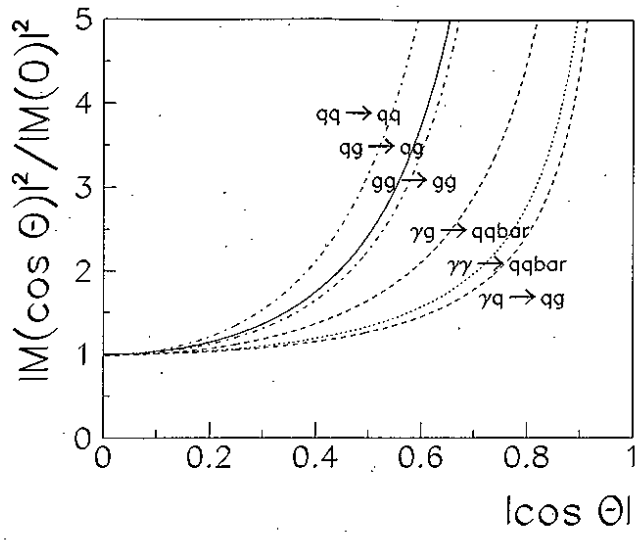

Figure 11: Comparisons of the shapes of the parton angular $\hat{\theta}$ distributions from Fig.10 of the parton scattering processes with the highest predicted rates. Since forward and backward parton scattering cannot be experimentally distinguished, the distributions are shown as a function of the absolute value of $\cos\hat{\theta}$. Matrix elements of resolved γ interactions rise more steeply than those of direct γ processes.

- Fragmentation

1. The fragmentation of a final state parton k into a hadron h is denoted by $D_{h/k}(z, \mu_{frag})$. Here z is the energy fraction of the hadron relative to the parton energy $z = E_h/E_k$, and μ_{frag} is the fragmentation scale, which is usually set equal to the hadron transverse momentum $\mu_{frag} = p_t^h$. The fragmentation functions have been parameterized from experimental results. In the case of the quark fragmentation function the accuracy obtained from e^+e^- measurements [BIN-95] is of the order of a few percent. The uncertainty in the gluon fragmentation function contributes an error of 20% to the QCD calculation of γp particle cross sections [BIN-96A]. The combination of LEP data and recently published UA1 data [UA1-95] should improve the accuracy of the gluon fragmentation function to the level of the quark fragmentation function.
2. The fragmentation of a final state parton k into a jet is treated by intelligent jet definitions: the jet algorithms are designed to integrate the energy of the partons

which is distributed to several hadrons during the fragmentation process. Common practice is therefore to set $D_{jet/k} \equiv 1$. Potential problems of this approach are under study [BUT-96].

To predict the inclusive cross sections of hadron and jet production, the parton cross sections have to be summed over all quarks and gluons, and integrated over all input distributions. The inclusive hadron and jet cross sections are then calculated by

$$\frac{d\sigma^h}{dt} = \sum_{ijk} \int dy\, dx_\gamma dx_\tau dz\; f_{\gamma/e}(y)\; f_{i/\gamma}(x_\gamma)\; f_{j/\tau}(x_\tau)\; \frac{d\hat{\sigma}}{d\hat{t}}(ij \to k)\; D_{h/k}(z) \tag{26}$$

$$\frac{d\sigma^{jets}}{d\hat{t}} = \sum_{ij} \int dy\, dx_\gamma dx_\tau \quad f_{\gamma/e}(y)\; f_{i/\gamma}(x_\gamma)\; f_{j/\tau}(x_\tau)\; \frac{d\hat{\sigma}}{d\hat{t}}(ij \to jets) \tag{27}$$

where the dependencies on the different scales μ_{ren}, μ_{fac}, μ_{frag}, and Q^2 have been suppressed to have legible formulae. Apart from these scales, a total of four variables is needed to describe the partonic state. This set of variables can e.g. be chosen to be $(y, x_\gamma, x_\tau, \hat{t})$. The parton CM energy $\sqrt{\hat{s}}$ of the parton cross section eq. (24) can be calculated from the photon and parton energy fractions, and the beam CM energy $s_{e\tau}$:

$$\hat{s} = y\; x_\gamma\; x_\tau\; s_{e\tau} \tag{28}$$

Other choices of the set of observables will be discussed in section 2.3.

Note that only the parton cross sections $d\hat{\sigma}/d\hat{t}$ are predicted by QCD theory. The common practice of calling the inclusive cross sections of equations (26) and (27) 'QCD predictions' rely on all the input distributions mentioned above, and on the factorization of the different input distributions. Turning the argument around: since QCD has been confirmed by many different experiments, comparisons of data with such complete calculations give potentially new information on the input distributions f and D.

2.3 Four observables to determine the parton kinematics

Convenient observables to describe the final state partons are their transverse momenta and rapidities in the laboratory system. The transformation from the parton center of mass system (PCMS) to the laboratory frame is given by

$$p_t = \hat{p}_t \tag{29}$$

$$\eta = \hat{\eta} + \eta_{pcms}. \tag{30}$$

Here the intrinsic transverse momenta of the partons from the photon and the target particle have been neglected. Since the parton configuration in the PCMS is back-to-back (Fig.8), $\hat{\theta_1} = \pi - \hat{\theta_2}$, their rapidity sum is $\hat{\eta_1} + \hat{\eta_2} = 0$. Using equation (30), the boost of the PCMS with respect to the laboratory system can be calculated by the parton rapidities in the laboratory frame:

$$\eta_{pcms} = \frac{\eta_1 + \eta_2}{2} \equiv \bar{\eta} \tag{31}$$

The rapidity difference is Lorentz invariant:

$$\Delta\eta \equiv \eta_1 - \eta_2 = \hat{\eta_1} - \hat{\eta_2} = -2 \ln \tan \frac{\hat{\theta}}{2}. \tag{32}$$

From this identity and trigonometrical gymnastics the cosine of the PCMS parton scattering angle results from

$$\cos\hat{\theta} = \tanh \frac{\Delta\eta}{2}. \tag{33}$$

At small values of the rapidity difference $|\Delta\eta| < 1$ it is simply $\cos\hat{\theta} \approx \Delta\eta/2$.

The scaled photon energy y was defined in eq.(1). The photon four vector γ can be calculated from the four vectors of the beam lepton e and the scattered lepton e' via $\gamma = e - e'$ (Fig.4). For quasi-real photons ($Q^2 \approx 0$), y results then from the energies of the beam lepton E_e and the scattered lepton $E_{e'}$:

$$y = 1 - \frac{E_{e'}}{E_e} \tag{34}$$

Alternatively, γ can be calculated from the target four vector τ and all final state partons with four vectors k_j, including the spectator partons, via $\gamma = \sum_j k_j - \tau$. Then the scaled photon energy is given by the transverse momenta $p_{t,j}$ and rapidities η_j of all partons:

$$y = \frac{\sum_j\; p_{t,j}\; e^{-\eta_j}}{2E_e} \tag{35}$$

The fractional parton energies x_γ and x_τ can be recovered from the two scattered partons with the four-momenta j_i from four-momentum conservation:

$$y x_\gamma e + x_\tau \tau = j_1 + j_2 \tag{36}$$

Here e and τ denote the four-vectors of the lepton and the target particle with the beam energies E_e and E_τ in the laboratory system. Multiplication of equation (36) with τ (e) leads to expressions for x_γ (x_τ), e.g. via the transverse momenta p_t and the rapidities η_i of the scattered partons:

$$x_\gamma = \frac{p_t}{2yE_e}\left(e^{-\eta_1} + e^{-\eta_2}\right) \tag{37}$$

$$x_\tau = \frac{p_t}{2E_\tau}\left(e^{+\eta_1} + e^{+\eta_2}\right) \tag{38}$$

So, the choice of the four variables (y, p_t, η_1, η_2) can be used to describe the initial partonic state, eqs. ((34 or 35),37,38,28). Also the parton final state can be calculated from these observables using eqs.(24,33): the differential parton cross sections can be rewritten to the form

$$\frac{d\hat{\sigma}}{d\hat{p_t}^2} = \frac{d\hat{\sigma}}{d\hat{t}} \frac{1}{\cos\hat{\theta}} \tag{39}$$

$$= \frac{|M|^2}{16\pi\, \cosh^4(\Delta\eta) \tanh(\Delta\eta/2)} \frac{1}{\hat{p_t}^4} \tag{40}$$

where $\Delta\eta = \eta_1 - \eta_2$.

$(y, p_t, \Delta\eta, \overline{\eta})$ also gives a possible set to describe the partonic state. The fractional energy of the partons is then calculated from:

$$x_\gamma = \frac{p_t}{2yE_e} \cosh(\Delta\eta)\, e^{-\overline{\eta}} \quad (41)$$

$$x_\tau = \frac{p_t}{2E_\tau} \cosh(\Delta\eta)\, e^{+\overline{\eta}} \quad (42)$$

The parton CM energy can be calculated using equations (28,41,42):

$$\hat{s} = \hat{p_t}^2 \cosh^2(\Delta\eta) \quad (43)$$

With this choice of observables one can see nicely that the different parton distributions are reflected in the boost $\overline{\eta}$ which is amplified by the exponential function (eqs.(41,42)). The parton cross sections (eq.(40)) are, of course, independent of the boost $\overline{\eta}$. Therefore studies of e.g. the inclusive jet rapidity cross sections $d\sigma/d\eta$, or the di-jet cross section as a function of the boost $d\sigma/d\overline{\eta}$, are sensitive to the parton distributions of the photon and the target particle.

At fixed rapidity difference the differential cross sections, eq.(40), have a strong dependence like $\hat{p_t}^{-4}$. This strong dependence dominates the logarithmic behaviour of the photon structure function $\ln(\hat{p_t}^2/\Lambda^2_{QCD})$, eq.(18). Therefore, studies of e.g. transverse jet energy distributions, eq.(27), exhibit essentially the features of the parton scattering processes.

2.4 Next-to-leading order QCD predictions

The LO QCD predictions for jet and particle cross sections have a strong dependence on the choice of the renormalization μ_{ren} and the factorization μ_{fac} scales. Several theory groups have therefore calculated next-to-leading (NLO) QCD predictions for the inclusive jet and particle cross sections [AUR-94, KRA-94A, BOD-94, GRE-94, GOR-94, KNI-94]. For the calculation of inclusive jet cross sections, a user friendly NLO QCD program package has been provided by [SAL-95]. NLO predictions have been calculated for di-jet cross sections [KLA-95B], and for the production of isolated, neutral particles: π° mesons and prompt photons [GOR-95].

A comparison of LO and NLO calculations for inclusive ep jet cross sections is shown in Fig.12 from [SAL-93]. The upper histogram shows the differential jet rapidity cross section $d\sigma^2/dp_t^{jet}/d\eta^{jet}$ for $p_t^{jet} = 5$ GeV. The full curve represents a LO QCD calculation. The dashed (dash-dotted) curve is a NLO QCD calculation using the cone jet algorithm [HUT-90] with $R = 1$ ($R = 0.7$). The triangles indicate the NLO QCD results using another cone jet algorithm. The LO and NLO QCD calculation with $R = 1$ differ by about 15% with only a small dependence on the rapidity of the jet.

The lower histogram of Fig.12 shows the scale dependence of the jet cross section at $\eta^{jet} = -2$. The variable ξ denotes the choice of the renormalization and factorization scales in multiples of the jet energy $\mu = \xi p_t^{jet}$. The NLO QCD calculations show smaller dependencies on the scale compared to the LO calculation.

In summary:

- The scale dependence of jet cross section calculations in γp scattering is significantly reduced in NLO QCD compared to the LO calculations.
- The results of LO QCD jet cross section calculations at the scale $\mu = p_t^{jet}$ are low by only 15% with respect the NLO calculations using jets with cone size $R = 1$.

2.5 Multiple parton interactions

The QCD parton cross section $d\hat{\sigma}/d\hat{p_t}^2$ has two inherent problems:

(a) It diverges towards small transverse momenta $\hat{p_t}$ of the scattered partons (section 2.1). This is usually solved by introducing a lower cut-off $\hat{p_t} > \hat{p_t}^{cut}$.

(b) The integrated parton cross section rises steeply with the CM energy. At some energy it exceeds the measured total cross section.

Item (b) is illustrated in Fig.13 which shows the energy dependence of the LO QCD parton cross section (dashed curve). It was calculated with the PYTHIA event generator (section 2.6) using the GRV-LO parameterizations of the parton distributions in the photon and the proton and a transverse momentum cut-off $\hat{p_t}^{cut} = 1.4$ GeV. Also shown is the energy dependence of the total photon-proton cross section, as parameterized by Donnachie and Landshoff [DON-92] (full curve), together with the HERA measurements at $\sqrt{s_{\gamma p}} \approx 200$ GeV (full circle: H1 [H1-95E], full triangle: ZEUS [ZEU-94A]). For fixed energy the problem (b) can be solved by a higher $\hat{p_t}$ cut-off, or by a reduction of the parton density in the photon. But this only shifts the problem towards higher CM energies.

Another possible solution is to consider the proton and the resolved photon as beams of partons and to allow for $n > 1$ parton interactions in one observable γp event [SJO-87B, SCH-93]. Then the observed inelastic cross section for resolved γp processes is n times smaller than the single parton cross section. Such a mathematical procedure which produces a varying number of parton interactions per event and ensures that the total parton cross section stays below the total observed cross section $\hat{\sigma} < \sigma_{\gamma p}$ is traditionally called 'unitarization'.

The obvious disadvantage of the multiple parton interaction concept is the introduction of additional model assumptions. The advantage of the concept is that the calculated non-diffractive γp cross section stays below the total cross section and describes the HERA measurements (Fig.13 dotted curve, open circle: H1 [H1-95E], open triangle: ZEUS [ZEU-94A]). Also, an important problem in the description of the energy flow in jet events is solved: the measured energy flow next to jets is much larger by far than expected from a single hard parton scattering process and its fragmentation. This energy flow is correctly described by the introduction of multiple parton interactions. The study of the energy flow in jet events turned out to be a key part for the understanding of the HERA data in terms of the parton content of the photon. It will be discussed in section 6.

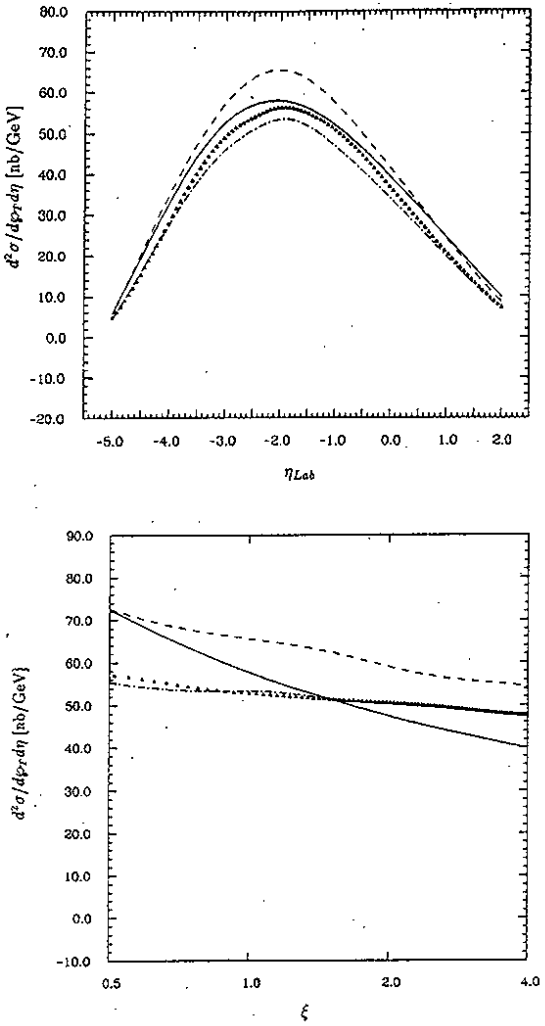

Figure 12: The upper histogram shows different calculations of the differential jet rapidity cross section for $p_t^{jet} = 5$ GeV. The full curve represents a LO QCD calculation. The dashed (dash-dotted) curve is a NLO QCD calculation using the cone jet algorithm [HUT-90] with $R = 1$ ($R = 0.7$). The triangles indicate the result using another cone jet algorithm.
The lower histogram shows the dependence of the jet cross section at the jet rapidity $\eta = -2$ on the renormalization and factorization scales in multiples of the jet energy $\mu = \xi\, p_t^{jet}$.

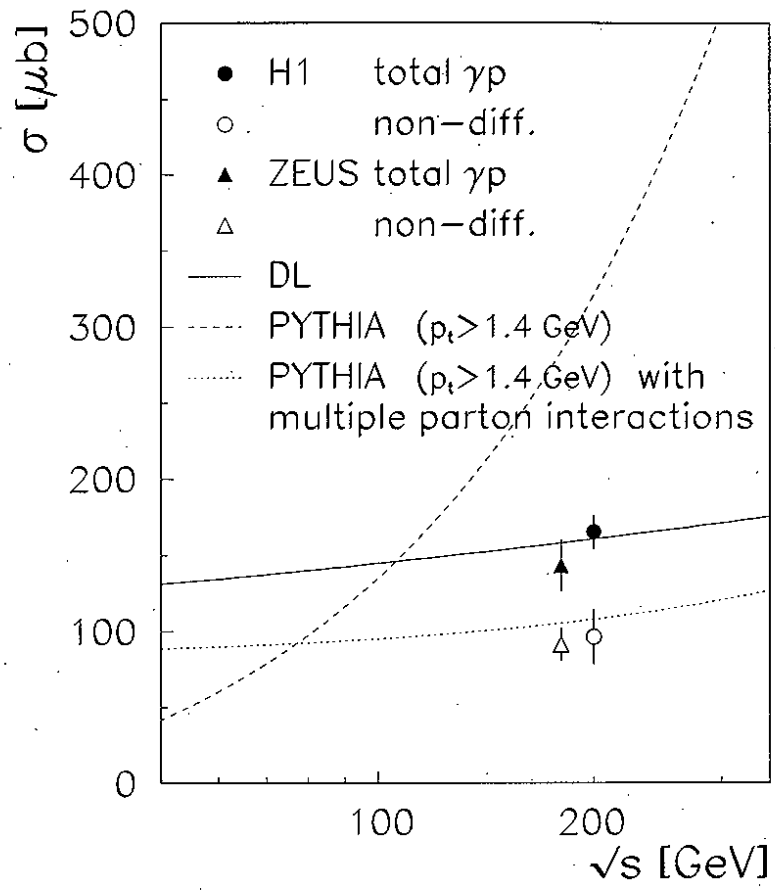

Figure 13: The energy dependence of the leading-order QCD parton cross section (dashed curve) for transverse parton momenta above $\hat{p}_t > 1.4$ GeV is shown using the PYTHIA generator together with the GRV-LO parameterizations of the parton distributions in the photon and the proton. The dotted curve shows the same calculation allowing for several parton scattering processes in one observable γp event (multiple parton interactions). For comparison, the energy dependence of the total photoproduction cross section is shown as the full curve [DON-92]. Also shown are the HERA measurements of the total photoproduction cross section by the full symbols, and the non-diffractive cross section by the open symbols (circles: H1 [H1-95E], triangles: ZEUS [ZEU-94A]).

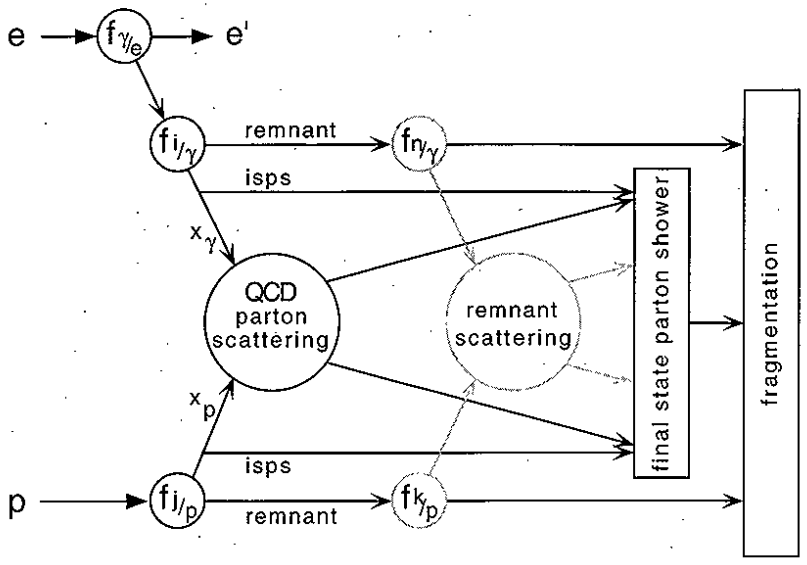

Figure 14: Schematic view of a QCD generator: the core is given by the QCD parton scattering process eq.(24). The input parton distribution functions are labeled $f_{i/\gamma}$ and $f_{j/p}$. The incoming and outgoing partons can radiate other partons (isps=initial state parton shower, final state parton shower). Together with the beam spectator partons (remnant) they fragment into hadrons (fragmentation). Optionally, interactions between the two beam remnants can be generated in addition to the primary hard parton scattering process.

2.6 Event generators

Quantitative analysis of hard scattering processes requires a detailed understanding of the hadronic final state which is measured in the detectors and its connection to the underlying parton dynamics which we want to study. This is the purpose of the QCD event generators.

In Fig.14 a schematic view of a QCD event generator is shown. In the central part of the program are the parton scattering processes eq.(24) together with the matrix elements of Tab.1. The partons from the photon and the target particle coming into the hard subprocess are chosen via the parton distribution functions $f_{i/\gamma}$ and $f_{j/p}$. Since incoming and outgoing partons can radiate other partons, so-called initial state and final state parton showers simulate higher order QCD processes. All partons, including those of the beam remnants, fragment into hadrons. The programs predict the exclusive hadronic final states of hard parton collisions.

The generators, described below, have the option of allowing interactions between the beam remnants in addition to the hard parton scattering process. The treatment of the remnant interactions is different in each of the generators which allows the study of the model dependencies of additional interactions.

PYTHIA

The PYTHIA 5.7 event generator is usually run in the mode of photon-proton interactions [SJO-94], together with a generator for quasi-real photons. PYTHIA is based on the leading order (LO) QCD matrix elements. It includes initial and final state parton radiation effects which are calculated in the leading logarithmic approximation. In most comparisons with data, the strong coupling constant α_s is calculated in first order QCD using $\Lambda_{QCD} = 200$ MeV with 4 flavours, and the renormalization and factorization scales are both set to the transverse momentum $\hat{p}_t$ of the partons emerging from the hard interaction. Since the LO QCD calculation of a single hard parton scattering is divergent for processes with small transverse momenta $\hat{p}_t$, a lower cut-off has to be applied. The lowest cut-off values chosen for comparisons with HERA data are around $\hat{p}_t^{cut} \approx 2$ GeV. For the hadronization process the LUND string fragmentation scheme is used (JETSET [SJO-87A]).

Within PYTHIA, multiple parton interactions may be generated in addition to the primary parton-parton scattering [SCH-93]. These are calculated as LO QCD processes between partons from the photon and proton remnants. The PYTHIA multiple parton interaction model extends the concept of the hard perturbative QCD parton scattering to the low transverse momentum, or semi-hard scattering region. In the simplest version of the model, the transverse momentum cut-off of the hard interactions is lowered to $\hat{p}_t^{mia} < \hat{p}_t^{cut}$. The mean number $\langle n \rangle$ of (semi-) hard interactions is given by

$$\langle n \rangle = \frac{\hat{\sigma}\,(\hat{p}_t > \hat{p}_t^{mia})}{\sigma_{non-diff.}} \tag{44}$$

where $\hat{\sigma}$ denotes the parton scattering cross section, and $\sigma_{non-diff.}$ is the observable non-diffractive γp cross section. The fluctuations of n are calculated based on a Poisson distribution. The number of additional interactions is typically between $1-4$. The parton process with the highest transverse momentum in the partonic final state can be given by any quark or gluon matrix element. This process includes initial and final state parton radiation effects and its partons are connected to the beam remnants by strings. The additional parton scattering processes in the event are calculated as perturbative gluon-gluon scattering processes. The initial state gluon momenta of each subsequent process are related to the remaining energy of the beam remnants. The resulting fractional momenta are used to determine the parton densities of the beam remnants.

PHOJET

The PHOJET 1.0 event generator was designed to simulate in a consistent way all components which contribute to the total photoproduction cross section [ENG-95]. It is based on the two-component Dual Parton Model [CAP-94]. The implementation of the PHOJET generator is similar to the Monte Carlo event generator DTUJET [AUR-92A, BOP-94B] which simulates multi-particle production in high energy hadron collisions. This latter generator was originally intended for the description of soft hadronic interactions and was then extended to hard scattering processes. In contrast to PYTHIA, PHOJET incorporates very detailed simulations of both multiple soft and hard parton interactions on the basis of a unitarization scheme [CAP-87]. The

soft hadronic processes are described by the soft, 'supercritical' Pomeron [ENG-92, BOP-94A]. These processes are simulated by a two-string ansatz which allows for initial transverse momenta of the partons at the ends of the strings. The hard processes are calculated using the LO QCD matrix elements. Final state parton radiation effects are simulated using the JETSET 7.4 program [SJO-87A]. Hard initial state parton radiation is not included in this version of PHOJET. The lower momentum cut-off for hard parton interactions was set to $\hat{p}_t^{cut} = 3$ GeV. Due to the unitarization scheme, small variations of this cut-off parameter do not have a large influence on the results of this generator. The model parameters which describe the soft part of the γp interactions have been tuned using results from proton–anti-proton collisions and low energy photoproduction cross section measurements. For the fragmentation the LUND string concept is applied (JETSET 7.4 [SJO-87A]).

HERWIG

The HERWIG 5.8 *ep* generator is also based on LO QCD calculations [MAR-92]. This program was designed to have as much input from perturbative QCD as possible, in order to minimize the free parameters. HERWIG includes a parton shower model which allows for interference effects between the initial and final state showers (colour coherence) [MAR-84, MAR-88A]. The renormalization and factorization scales are set according to the transverse momentum of the scattered partons with a lower cut-off $\hat{p}_t^{cut} \geq 2$ GeV. A cluster model is used to simulate the hadronization effects [WEB-84, MAR-88B].

HERWIG also has the option of allowing for additional interactions between the beam remnants. These interactions are called the *soft underlying event* and are parameterizations of experimental results on 'soft' hadron-hadron collisions. A tuning of the strength and frequency parameters is still in progress. Recently, a model for multiple parton interactions has also been developed for HERWIG [BUT-95].

Summary: hard photon–target interactions

- QCD predicts the cross sections of parton–parton scattering as functions of the parton center of mass energy, and the parton scattering angle.
- For predictions of jet and particle cross sections, the parton luminosities and fragmentation functions are needed on input. Comparisons of measurements with LO and NLO QCD predictions provide on one side tests of perturbative QCD, on the other side they give information on the parton distributions and fragmentation effects.
- Four observables are needed to calculate the final state parton kinematics in leading order, e.g. the scaled photon energy y, the transverse parton momentum p_t, and the parton rapidities η_1, η_2. These variables are conveniently related to observables in di-jet events.
- For the prediction of the exclusive final state in photon–nucleon and photon–photon interactions event generators have been provided which are based on LO QCD calculations.

Generator		soft proc.	hard proc. QCD	transition soft↔hard: unitarization	beam remnant interactions	parton showers	hadronization
PYTHIA	1		•			initial and final state	string
	2		•	•	multiple hard parton ia		
	3	•					
PHOJET		•	•	•	soft and hard multiple parton ia	final state	string
HERWIG	1		•			initial, final state plus interference	cluster
	2		•		soft underlying event		
	3		•	•	multiple hard parton ia		

Table 2: Comparison of different LO QCD Generators: all models include the LO QCD matrix elements (hard interactions), parton radiation effects to simulate higher order effects, and a simulation of the fragmentation phase. Some generators offer in addition options for interactions between the beam remnants, a modeling of the transition region between soft and hard processes, or the soft interactions themselves.

- In resolved photon–nucleon interactions, or double resolved photon–photon scattering, the photon and the nucleon can be considered as beams of partons such that several parton pairs may collide in one observable event (multiple parton interactions).

Part III

Two-γ physics: deep inelastic lepton–photon scattering

Around 1980, the e^+e^- collider experiments started to study photon-photon interactions for which the Feynman diagram is shown in Fig.3. Here we are interested in $\gamma\gamma$ processes where one photon is quasi-real ($Q^2 \approx 0$ GeV^2) from which the second photon is scattered with high $Q^2 \gg 1$ GeV^2: this process can therefore be regarded as deep-inelastic scattering (DIS) from a real photon target.

The double differential cross section as a function of Q^2 and the parton energy fraction x_γ is related via a kinematical factor to the structure function F_2^γ of the quasi-real photon:

$$\frac{d^2\sigma}{dx_\gamma\, dQ^2} = \frac{4\pi\alpha^2}{x_\gamma Q^4}\left(1 - y + \frac{y^2}{2}\right) F_2^\gamma(x_\gamma, Q^2) \qquad (45)$$

Here y denotes the scaled photon energy.

In the following sections we will discuss the F_2^γ measurements, and summarize the parton distribution functions which were extracted from the F_2^γ measurements.

3.1 Measurements of the photon structure function F_2^γ

Fig.15 shows one of the measurements of the photon structure function F_2^γ/α for $\langle Q^2\rangle = 5.3$ GeV^2 as a function of the parton momentum fraction x_γ [BER-87]. In contrast to hadronic structure functions (long-dashed line labeled 'HAD') F_2^γ rises with x_γ.

A compilation of all F_2^γ measurements, available in 1991, are shown in Fig.16 (from [VOG-94]). The photon virtuality varies in the range $0.7 < Q^2 < 100$ GeV^2, covering fractional parton energies up to $x_\gamma = 0.9$. The accuracy of the measurements varies between $10 - 50\%$. The data appear essentially flat in x_γ, but show a significant rise with increasing Q^2.

Recently, smaller x_γ values became available at high Q^2 from experiments at the TRISTAN and LEP colliders. In Fig.17 F_2^γ measurements of the TOPAZ, OPAL, and DELPHI experiments are compared at similar average $\langle Q^2\rangle \approx 15$ GeV^2 [TOP-94A, WAR-94, DEL-95]. The agreement between the two LEP measurements is quite good. They show a decrease towards small x_γ. The TOPAZ measurement on the other hand shows the tendency to increase towards small x_γ. The data points were here lowered by the QPM charm contribution calculated in [TOP-94A] in order to compare with the LEP measurements.

The data are compared to different parameterizations of the parton distributions of the photon, calculated at $\langle Q^2\rangle = 12$ GeV^2 [DEL-95]. The different curves demonstrate the uncertainties in the extrapolations towards the small x_γ region. For new parameterizations of the parton distributions of the photon at small x_γ, the difference between the experimental results needs to be clarified.

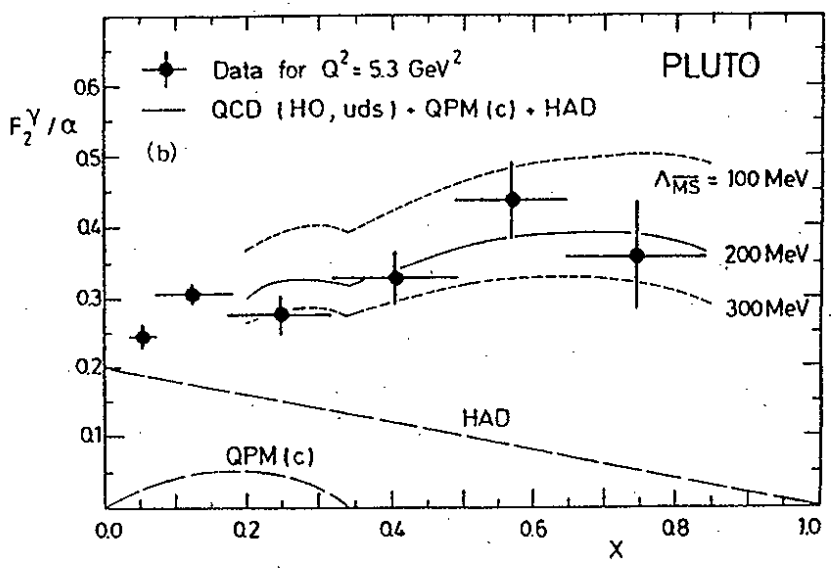

Figure 15: The photon structure function F_2^γ is shown as a function of the parton momentum x_γ at the average scale $\langle Q^2\rangle = 5.3$ GeV^2 (PETRA: PLUTO Collab.[BER-87]). The measured F_2^γ increases with x_γ, which is clearly distinct from a hadronic structure function, and arises from the pointlike coupling of the photon to quarks. The long-dashed curve HAD indicates the structure function of a vector meson. The curve QPM reflects the charm contribution as calculated in the Quark Parton Model. The full curve shows the summed QPM and HAD contributions together with a higher order QCD calculation for the light quarks. The short dashed curves indicate the sensitivity of the calculation to the QCD parameter Λ_{QCD}.

The anomalous photon component can be tested directly by measuring the Q^2 dependence of F_2^γ at large x_γ (eq.(18)). In Fig.18 the Q^2 dependence of the data is studied at large fractional parton energies between $0.3 < x_\gamma < 0.8$ (compilation by [KEN-96]). The structure function F_2^γ rises with increasing Q^2 at a rate that is compatible with a linear dependence on $\log Q^2$ and confirms the anomalous component of the photon which was predicted by QCD. Note that even at large x_γ the hadronic contribution to F_2^γ is sizable at $Q^2 = 5$ GeV^2 which can be seen from Fig.15. Since this part cannot be calculated by perturbative QCD, a precise determination of α_s from the F_2^γ data, which was proposed in eq.(18), is difficult.

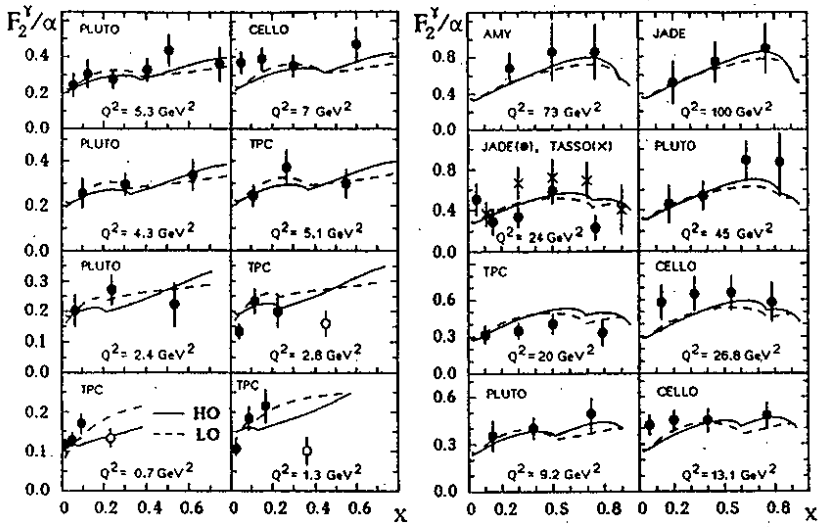

Figure 16: Measurements of the structure function F_2^γ of the quasi-real photon are shown from experiments before 1991. The data are drawn as a function of the parton energy fraction x_γ and at different average photon virtuality Q^2.
The data are compared with the LO (dashed) and NLO (full) parameterizations by GRV [GLU-92C]. The full points were used to fit the parameter κ of this parton distribution function (from [VOG-94]).

Summary: measurements of the photon structure function F_2^γ

- Two-photon experiments have established the anomalous photon component which was predicted by QCD theory.
- The measurements of the structure function F_2^γ constrain the quark distribution of the photon in the range of fractional parton energies $0.05 < x_\gamma < 0.9$ to the level of $10-50\%$. At small $0.1 \ll x_\gamma$ and large $Q^2 \approx 15$ GeV^2, differences between recent measurements at TRISTAN and LEP have to be clarified.
- The anomalous photon component cannot be separated in a unique way from the hadronic part of the photon structure function. Therefore, for meaningful prediction of e.g. jet production rates in $\gamma\gamma$ or γp scattering, the parton distributions need to include both the anomalous and the vector meson components of the photon.

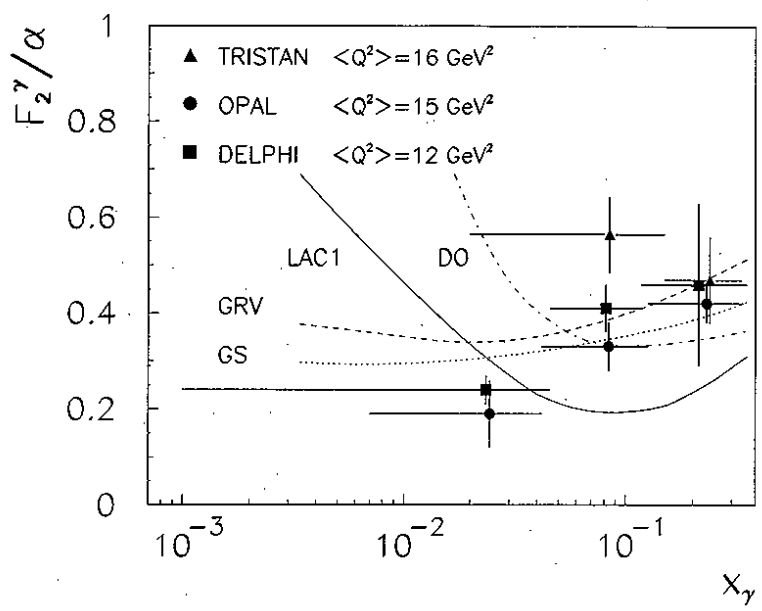

Figure 17: The photon structure function F_2^γ was measured at average scale $\langle Q^2 \rangle \approx 15$ GeV^2 in the interval of the parton fractional energy $0.001 \leq x_\gamma \leq 0.35$ (TRISTAN: TOPAZ [TOP-94A], LEP: OPAL [WAR-94], DELPHI [DEL-95]). Only statistical errors are shown in the figure. The curves represent the photon structure function as obtained with different parameterizations of the parton distributions [DEL-95]: full=LAC1 [ABR-91], dashed=GRV [GLU-92C], dotted=GS [GOR-92], dash-dotted=DO [DUK-82].

3.2 Parameterizations of the parton distributions of the photon

The parton distributions of the photon can be extracted from the photon structure function measurements using eq.(14) and the evolution equations (16, 17). For convenient application, parameterizations of the parton distributions were introduced which contain the parton momentum distributions at some scale Q_0^2 and their Q^2 evolutions. Almost all of them are used somewhere by experiments. Here a short summary from the user's point of view is given, for recent theoretical reviews refer to e.g. [VOG-94, SJO-96]. Meanwhile more than a dozen parameterization sets exist with most of them available via the PDFLIB [PLO-93]. The parameterizations can be subdivided into three categories:

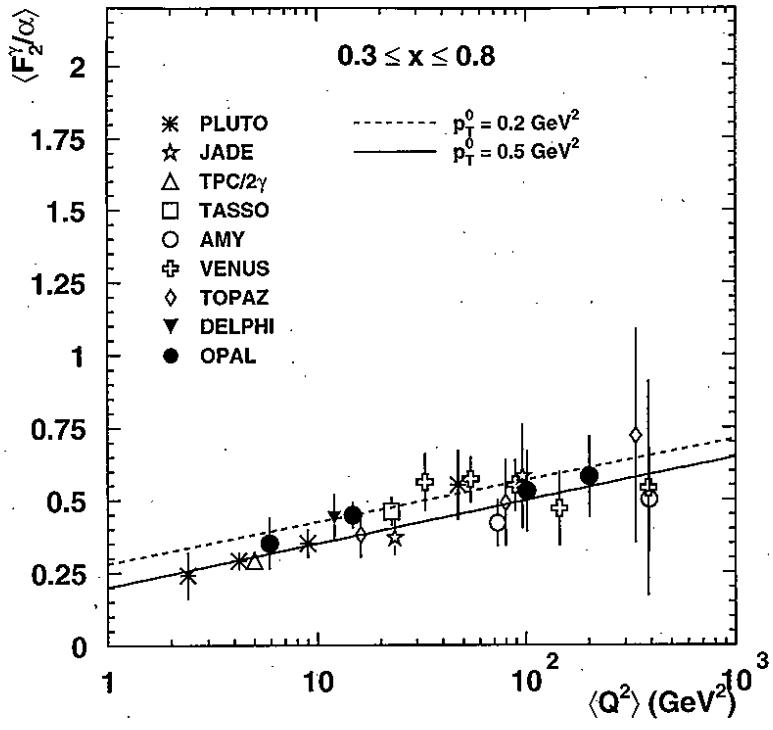

Figure 18: Measurements of the photon structure function F_2^γ as a function of the scale Q^2 for a fixed interval of parton fractional energies $0.3 < x_\gamma < 0.8$. The data are compatible with a linear dependence of F_2^γ on $\log Q^2$, as predicted by QCD theory. The curves are the calculations of the FKP model [FIE-86, FIE-87] using different cut-off values for the model parameter p_T^o (compilation from [KEN-96]).

- Pointlike/anomalous component of real photons:
  - The first parameterizations were constructed by Duke and Owens (DO) who made an ansatz for the pointlike coupling of the photon and used an asymptotic solution for the evolution equations [DUK-82]. The parton distributions of the vector meson part of the photon had to be added 'by hand', e.g. from the TPC/2γ measurements [TPC-87].
  - Field, Kapusta and Paggioli (FKP) provided parameterizations of the pointlike part including higher order QCD effects. The parameterizations contain the Q^2 evolution

at large x_γ [FIE-86, FIE-87, KAP-89].

- Complete parameterizations of the real photon:
  - The first successful attempt to parameterize the pointlike and vector meson parts of the photon structure together was carried through by Drees and Grassie (DG) [DRE-85]. Using an ansatz for the parton distributions at $Q^2 = 1$ GeV^2 together with the LO inhomogeneous evolution equations, they fitted first data points from deep inelastic $e\gamma$ scattering experiments [BER-83].
  - This ansatz was carried further by Levy, Abramowicz and Charchula (LAC) [ABR-91] using more than 50 data points. They demonstrated that the gluon distribution in the photon, which enters only via the Q^2 evolution, was not constrained by the DIS $e\gamma$ results. Accordingly, they provided three different test sets of LO parameterizations of photonic parton distributions with different gluon contents.
  - In a similar approach by Watanabe, Hagiwara, Izubuchi and Tanaka, the charm contribution to F_2^γ was treated in an elaborate way: 6 WHIT parameterizations were obtained, each with different gluon distributions in the photon [HAG-95].
  - Gordon and Storrow (GS) provided several, LO and NLO, parameterizations where e.g. they used a gluon input at $Q^2 = 5.3$ GeV^2 equivalent to that of a vector meson [GOR-92]. They allowed for a κ-factor for the overall uncertainty of this ansatz, and fitted κ and the light quark masses to the DIS $e\gamma$ data.
  - Glück, Reya and Vogt (GRV) provided LO and NLO parameterizations which are constructed at very low $Q_o^2(\mathrm{LO}) = 0.25$ GeV^2 [GLU-92C]. Here the valence quark distributions in the photon have the same shape as in the pion structure function [GLU-92B]. The gluon content was set proportional to the valence quark content. They fit only 1 parameter, essentially the same κ-factor as GS, to the DIS $e\gamma$ data (Fig.16).
  - Aurenche, Fontannaz and Guillet (AFG) provided a NLO parameterization with a more elaborate ansatz for the vector meson input at low Q_o^2. No fit to data was performed.
- Complete parameterizations for real and virtual photons:
  - Glück, Reya and Stratman extended the very low Q_o^2 ansatz for real photons and studied the photon at virtualities ≈ 1 GeV [GLU-95]. Non-perturbative contributions to the photon structure are predicted to be sizable here as well.
  - Schuler and Sjöstrand (SAS) fitted the shapes of their parameterization to real photon data and constrained the normalization via the Vector Meson Dominance model. In addition to the parameterizations for real photons they provide them also for virtual photons based on a dispersion relation in the photon mass [SCH-95, SCH-96].

A comparison of the main features of the different parameterizations is shown in table 3. Examples for different parameterizations of the parton distributions in the photon are shown in Fig.19 from [SJO-96]. The LO and NLO quark parameterizations agree in the range $0.1 < x_\gamma < 0.9$ to

authors	year	real γ	virtual γ	LO	NLO	pointlike/ anomalous	hadronic/ vdm	Q_o^2 [GeV^2]
DO	82	•		•		•		
FKP	86	•			•	•		
DG	85	•		•		•	•	1
LAC	91	•		•		•	•	1/4
WHIT	95	•		•		•	•	4
GS	92	•		•	•	•	•	5.3
GRV	92	•		•	•	•	•	0.25/0.3
AFG	94	•			•	•	•	0.25
GRS	94	•	•	•	•	•	•	0.25/0.3
SAS	95	•	•	•		•	•	0.6/2

Table 3: Parameterizations of parton distributions in real and virtual photons in LO and NLO QCD. They contain the pointlike (i.e. anomalous) component of the photon, or both the pointlike and hadronic (i.e. VDM) components of the photon. The parameterizations were constructed at a fixed scale Q_o^2. Higher values of the scale are calculated with the inhomogeneous QCD evolution equations. To constrain the gluon in the photon, some parameterizations use information from vector mesons.

the level of 30%. At large $x_\gamma > 0.9$ the parameterizations show large differences, most striking is the steep increase of the GRV-NLO and AFG-NLO distributions. At small $x_\gamma < 0.1$ the large differences between the extrapolation of different LO quark parameterizations were shown in Fig.17. The gluon distribution is essentially unconstrained by the DIS $e\gamma$ data, as demonstrated by the different LAC parameterizations in Fig.19. The NLO gluon parameterizations look very similar. This however is not a consequence of the data, but a result of similar theoretical input, based on the VDM model.

Summary: parameterizations of the parton distributions of the photon

- From the F_2^γ measurements, parton distributions were extracted and parameterized as functions of x_γ and Q^2. They form the basis for predictions of particle and jet production, e.g., in collisions of two quasi-real photons at KEK and LEP, or in hard photon–proton scattering at HERA.
- The gluon distribution of the photon is essentially unconstrained by DIS $e\gamma$ experiments.

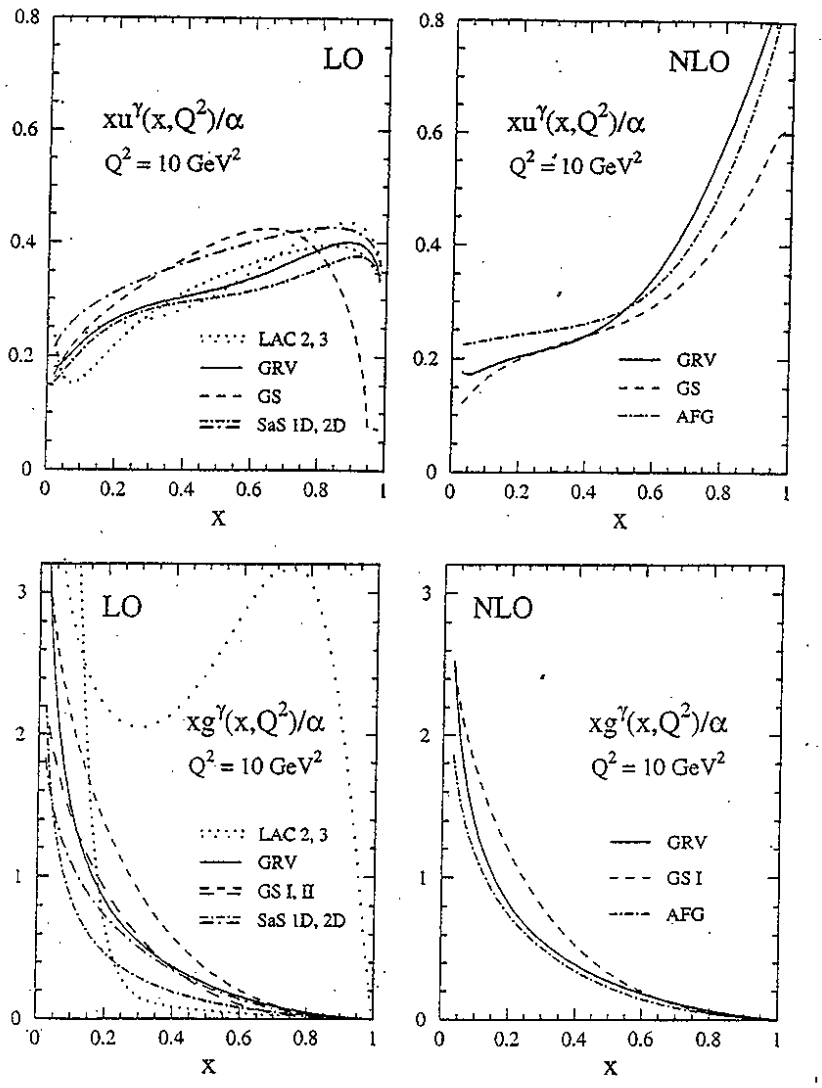

Figure 19: Different LO (left) and NLO (right) parameterizations for the parton distributions in the photon are compared. The upper two histograms show the u-quark densities which are known to the level of 30% in the range $0.1 \leq x_\gamma \leq 0.9$, but have large uncertainties at high momenta $x_\gamma \to 1$. The lower two histograms refer to the gluon in the photon which has essentially no constraints from the results of deep inelastic $e\gamma$ experiments. The similarity of the different NLO gluon parameterizations arises from a similar modeling of the gluon in the photon, but not from photon data (from [SJO-96]).

Part IV

Photon–proton interactions at HERA

4 Introduction

The lepton-hadron collider HERA allows the study of a rich variety of different physics processes. In this introduction to photoproduction physics at HERA we want to

1. list the relevant photoproduction processes,
2. define the final state variables,
3. identify the kinematic region where scattering of partons from the photon and the proton can be observed, and
4. explain the main features of the machine and the detectors.

4.1 Photoproduction processes

In Fig.20 an overview over the photoproduction processes at HERA is given. Three types of processes can be distinguished: elastic, diffractive processes and non-diffractive processes.

They can be further separated into soft and hard processes according to the transverse energy produced in the hadronic final state. The soft processes include elastic vector meson production, photon-diffractive, proton-diffractive and double diffractive scattering. Soft non-diffractive processes dominate the total cross section (Fig.13, [ZEU-94A, H1-95E]). Such processes can be understood as peripheral collisions of a vector meson like photon and the proton.

Hard scattering processes which lead to particles with high transverse momenta and jets have been observed in non-diffractive processes [H1-92, ZEU-92], and recently also in diffractive scattering [H1-95A, ZEU-95B]. Here direct and resolved photon processes are predicted by QCD. In this review, we are interested in the hard scattering processes leading to particles with high transverse momenta and jets, in order to study the photon and its partonic interactions. We concentrate on the study of non-diffractive hard scattering, since here the parton luminosities of the proton provide well defined input distributions for the QCD calculations.

4.2 Event kinematics

Variables to describe the final state particles

To describe the final state particles, three variables are conventionally used which are drawn in Fig.21:

- the transverse momentum p_t is measured with respect to the beam axis,

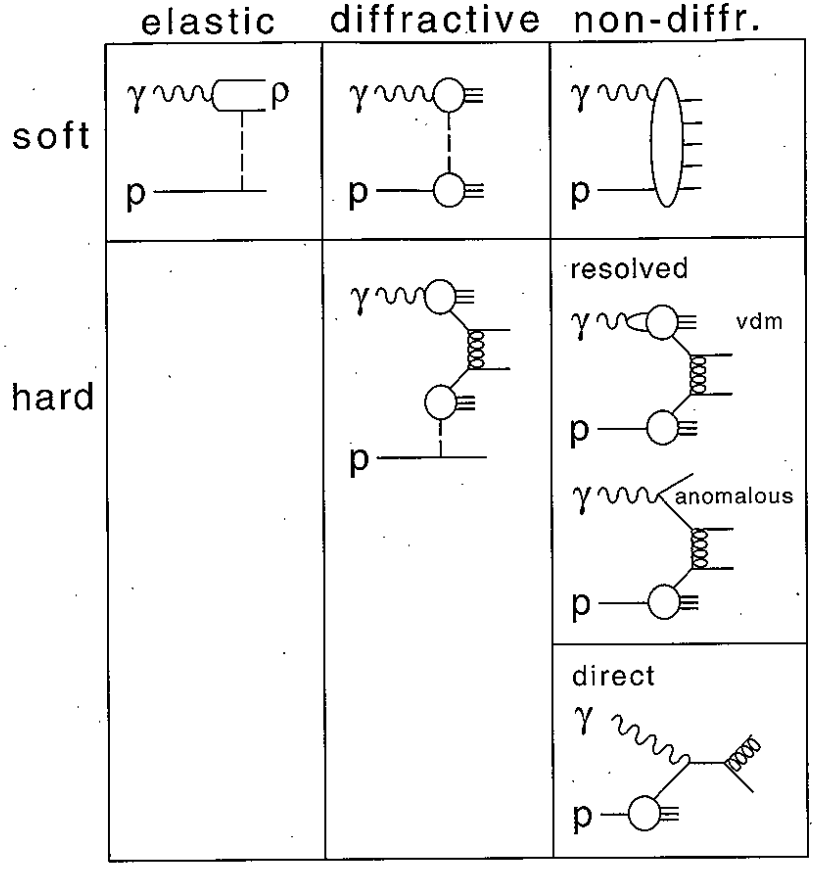

Figure 20: Photoproduction processes are labeled 'soft' and 'hard' according to the transverse energy E_t produced in the hadronic final state. The soft processes include elastic contributions, e.g. ρ production, single and double diffractive processes, and non-diffractive interactions, i.e. peripheral photon-proton scattering processes.
In the non-diffractive hard processes, the quarks and gluons of the proton are used to probe the quasi-real photons. Shown are two examples of *resolved* photon-proton interactions: in anomalous γp processes, the photon fluctuates into a $q\bar{q}$ pair before it interacts with a parton from the proton. In vdm resolved γp processes a $q\bar{q}$ pair of the photon forms a vector meson state before the scattering. In *direct* photon-proton interactions the bare photon couples to a quark of the proton.
In diffractive events hard scattering processes have recently been established. These events are also expected to have direct and resolved γp processes (this separation is not shown in the figure).

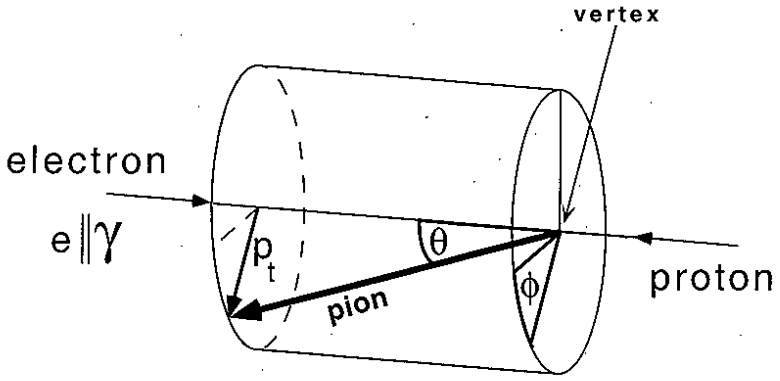

Figure 21: Variables for the final state particles: The transverse momentum p_t is measured with respect to the beam axis. φ denotes the azimuthal angle around the beam axis. The polar angle θ is measured relative to the proton direction. Instead of θ the pseudo-rapidity $\eta = -\ln\tan(\theta/2)$ is frequently used.

- φ describes the azimuthal angle around the beam pipe, and
- θ is the polar angle with respect to the proton direction. It is frequently replaced by the laboratory pseudo-rapidity, defined as $\eta = -\ln\tan(\theta/2)$. We will also make use of the pseudo-rapidity in the photon–proton center of mass system which we denote $\eta_{\gamma p}$.

Photon virtuality Q^2, center of mass energy $\sqrt{s_{\gamma p}}$, and transverse energy E_t

The available phase space at HERA is sketched in Fig.22 as functions of the photon virtuality Q^2, the photon–proton CM energy $\sqrt{s_{\gamma p}}$, and the summed transverse energy E_t of the final state hadrons.

We measure continuously from $Q^2 \approx 0$ GeV^2 (photoproduction) to large values of Q^2 (deep inelastic lepton–proton scattering) with a transition region around $Q^2 \approx 1$ GeV^2. The transition region is very interesting and is presently under study by several theory groups and by the experiments. For the purpose of this review we concentrate on quasi-real photons which are best selected in the kinematical region below $Q^2 < 10^{-2}$ GeV^2 and between $150 < \sqrt{s_{\gamma p}} < 250$ GeV by the detection of the scattered lepton in the electron detector of the luminosity system (dashed window: 'tagged electron').

In order to increase statistics, events are also analysed in which the electron disappears undetected at small scattering angles θ_e with average virtuality $Q^2 = 10^{-3}$ GeV^2 [ZEU-95B], and a maximum virtuality of $Q^2 = 4$ GeV^2 ('untagged events'). The photon energy is derived from the scattered electron energy, eq.(34), in the case of electron tagged events and in the untagged case from the final state hadrons, eq.(35).

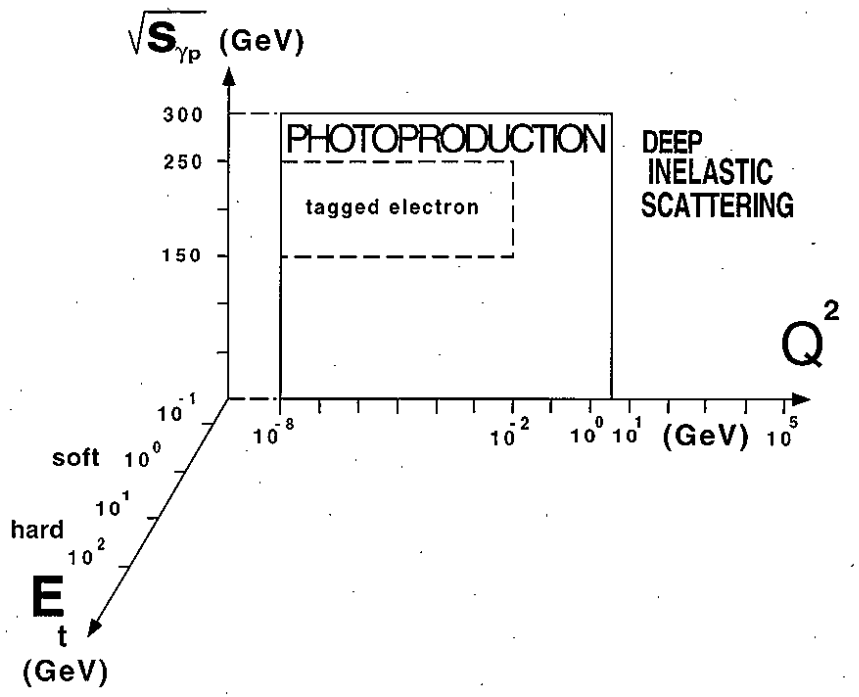

Figure 22: Relevant scales for photon-proton scattering at HERA: The negative squared four-momentum of the exchanged photon is $Q^2 \equiv -\gamma^2$ (Fig.4). Above $Q^2 \approx 4$ GeV^2 the interacting leptons are scattered into the main detectors (Figs.26, 27). These events are attributed to deep inelastic *ep* scattering processes. The region below $Q^2 \approx 1$ GeV^2 is termed the 'photoproduction' region, i.e. the scattering of quasi-real photons with protons. $\sqrt{s_{\gamma p}}$ is the photon-proton CM energy. The dashed line indicates the kinematic window where the scattered lepton can be found in the small angle electron detector of the luminosity system. E_t denotes the summed transverse energy produced in the hadronic final state. The low E_t region, labeled 'soft', refers to peripheral scattering processes between the proton and vector meson states of the photon. High E_t corresponds to the region where hard parton scattering processes between the photon and the proton are expected.

For the study of hard scattering processes events with sufficiently high transverse energy E_t are required (E_t at least 10 GeV).

Parton kinematics

The fractional parton energies, x_γ and x_p, can be reconstructed in two-jet events using eqs.(37,38). In Fig.23, three typical jet configurations are shown which correspond to:

(a) **low-x_γ** and **high-x_p**: both jets are found at large rapidities η,

(b) **high-x_γ** and **high-x_p**: one jet is at positive, one jet at negative rapidities,

(c) **high-x_γ** and **low-x_p**: both jets are at rapidity $\eta \approx 0$.

Transverse energy as a function of rapidity

The boost of the photon–proton center of mass system (CMS) with respect to the laboratory system is about $\Delta\eta = 2$. In Fig.24 a schematic view of the transverse energy distribution is shown as a function of the photon–proton CM rapidity $\eta_{\gamma p}$. The additional axes indicate the laboratory variables η and θ. The proton remnant particles appear as the enhancement at positive rapidities. The region within ± 1 units around the γp rapidity $\eta_{\gamma p} = 0$ we call the 'mid-rapidity' region. The negative (positive) rapidity region $\eta_{\gamma p} < -1$ ($\eta_{\gamma p} > 1$) corresponds to the 'photon fragmentation region' ('proton fragmentation region'). The scattered electron is indicated at negative rapidities (not to scale).

The geometric acceptance of the H1 and ZEUS detectors and their electron detectors is indicated by the dashed lines. The main detectors cover a large fraction of the photon fragmentation region, the central photon-proton collision region, and only a small part of the proton fragmentation region.

4.3 The HERA accelerator

A new generation photon facility became alive in 1992 when the first lepton-proton collider HERA was turned on at DESY (Hamburg, Germany). The center of mass energies here are one order of magnitude above the previous photon experiments and reach up to $\sqrt{s_{ep}} \approx 300$ GeV. The separate storage rings for the protons and the electrons have a circumference of 6.3 km and provide 4 interaction regions. The beam energies of the proton $E_p = 820$ GeV and the electron $E_e = 26.7$ GeV are largely asymmetric, satisfying the need for high center of mass energies at minimal synchrotron radiation losses. In 1994 the electron energy was raised slightly to $E_e = 27.5$ GeV, and later positrons were filled instead of electrons with the advantage of more stable running conditions. In principle a maximum of 210 bunches of electrons and protons, separated in time by 96 nsec, can be filled. For the purpose of controlling the background in the experiments, ~ 10 electron (proton) bunches are usually filled without a proton (electron) bunch partner. Variation of the interaction points along the beam direction is determined by the proton bunch lengths, and shows an approximately Gaussian distribution with a width of $\sigma = 11$ cm. A proton fill typically lasts one day, a positron fill around 7 hours.

The luminosity has increased each year since the start-up of HERA and has reached $L = 6.7 \times 10^{30}$ cm^{-2}s^{-1} which corresponds to about half the design luminosity. The integrated luminosity produced for the years 1992 to 1995 is shown in Fig.25. It is one order of magnitude below the expectations, but still provided sufficient statistics for the study of photoproduction physics. In the left histogram the luminosity produced by the HERA machine is shown, the right histogram represents the luminosity used by the H1 experiment for data taking.

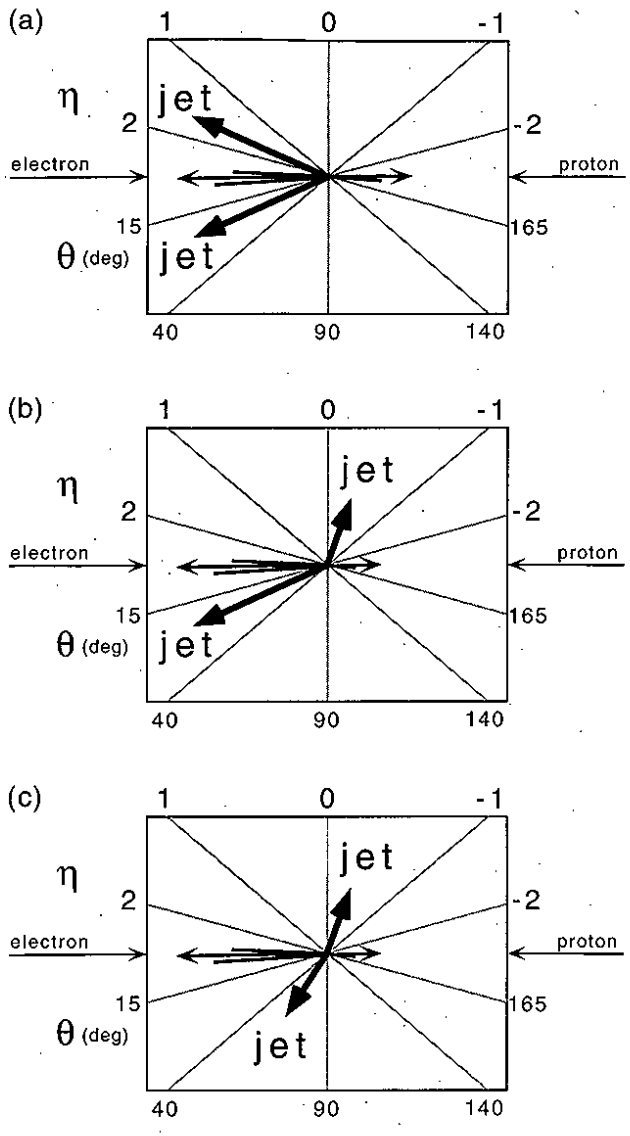

Figure 23: Different jet configurations correspond to different regions of the parton kinematics.
(a) at low-x_γ and high-x_p both jets are found at large rapidities η,
(b) at high-x_γ and high-x_p one jet is at positive, one jet at negative rapidities,
(c) at high-x_γ and low-x_p both jets are at rapidity $\eta \approx 0$.

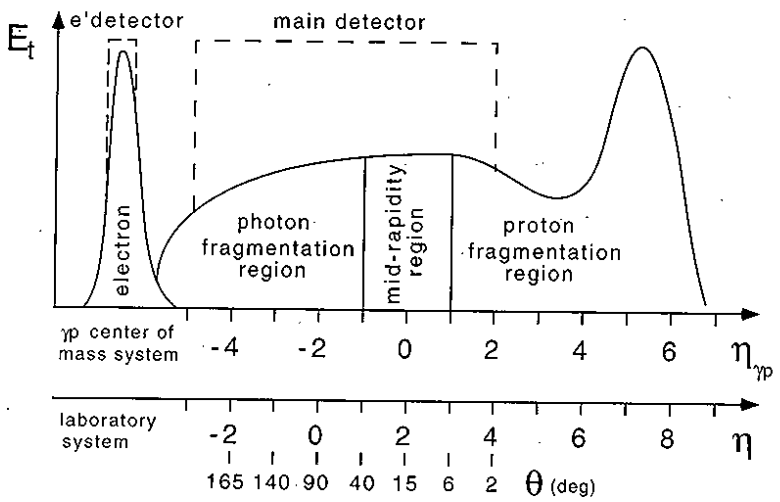

Figure 24: A schematic view of the transverse energy flow is drawn as a function of the photon–proton CMS rapidity $\eta_{\gamma p}$. Also shown are the corresponding observables in the laboratory frame, rapidity η and polar angle θ, and the position of the main detector. The electron distribution is indicated on the left side (not to scale).

4.4 The H1 and ZEUS experiments

The asymmetric beam energies imply a boost of the final state particles into the proton direction: e.g., a pion which was scattered at 90° in the photon–proton CMS is at $\theta \approx 15°$ in the laboratory system (Fig.24). The energy of our hypothetical pion in the laboratory system is approximately a factor four above its CM energy. The detector design, e.g. the interaction length covered by the calorimeters, was adapted according to these conditions.

The H1 and ZEUS collaborations designed multi-purpose detectors (Fig.26, 27). Elaborate descriptions exist in the literature [H1-96B, ZEU-93]. Here only a short description of those parts which are relevant to this review are given, with special emphasis on the differences between the detectors which led to partly complementary achievements in the photoproduction sector.

Both experiments have several tracking devices which detect charged particles over the full azimuth and in the polar angular region between $5° \leq \theta \leq 172°$. The trackers are located inside a strong magnetic field with 1.15 (1.4) Tesla in the H1 (ZEUS) experiment. Published results on charged particle production in photoproduction processes rely on the central cylindrical drift chambers which detect tracks in the interval $20° \leq \theta \leq 150°$. The precision in the transverse momentum measurements of the particles is $\sigma_{p_t}/p_t = 0.0075\, p_t \oplus 0.01$ $(0.005\, p_t \oplus 0.016)$ with p_t in GeV for the H1 (ZEUS) detector.

The tracking detectors are surrounded by calorimeters with electromagnetic (em) and hadronic (had) sections. The ZEUS collaboration built a Uranium-scintillator calorimeter with

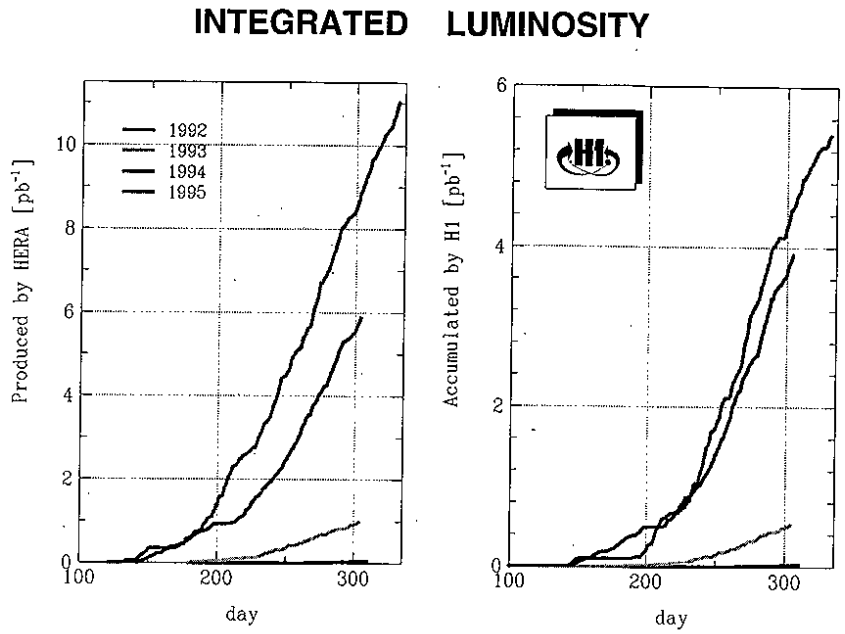

Figure 25: Integrated luminosity versus the day of the year: in the left histogram the integrated luminosity produced by the HERA machine is shown. The luminosity has increased each year since the start-up of HERA in 1992, and has now reached up to 50% of the design luminosity 1.5×10^{31} cm^{-2}s^{-1}. About half of the produced luminosity is used for data taking (right histogram from H1 Collab.).

photomultiplier read-out. The thickness of the Uranium and scintillator layers were optimized for the hadronic energy resolution: electrons and pions with the same energy give the same energy response in the calorimeter ('compensation'). The calorimeter covers the polar angular interval $2.6° \leq \theta \leq 176.1°$. It is mechanically separated into three parts, rear (electron direction), barrel, and forward calorimeter (proton direction). The size of the stacks in the em section is 5×20 cm^2 (10×10 cm^2 for the rear calorimeter) with a depth of 25 radiation lengths. The hadronic stacks are 20×20 cm^2 in size. The total absorption corresponds to $7 - 4$ interaction length, decreasing with increasing θ. The energy resolution for electrons is $\sigma_E/E = 0.18/\sqrt{E} \oplus 1\%$ with E in GeV, and for pions $\sigma_E/E = 0.35/\sqrt{E} \oplus 1\%$. For photon-proton collisions this calorimeter is especially well suited to measure the hadronic energy depositions over a wide range in the photon fragmentation region of the γp CMS with a single calorimeter type.

The corresponding calorimeter system of H1 consists of two main parts, a liquid Argon calorimeter (LAr) and a lead scintillator calorimeter (1992-94: BEMC, since 1995: SPACAL). The LAr calorimeter covers the polar angle between $4° \leq \theta \leq 153°$. The em section consists of lead absorbers and is $20 - 30$ radiation lengths deep. The hadronic section was built with

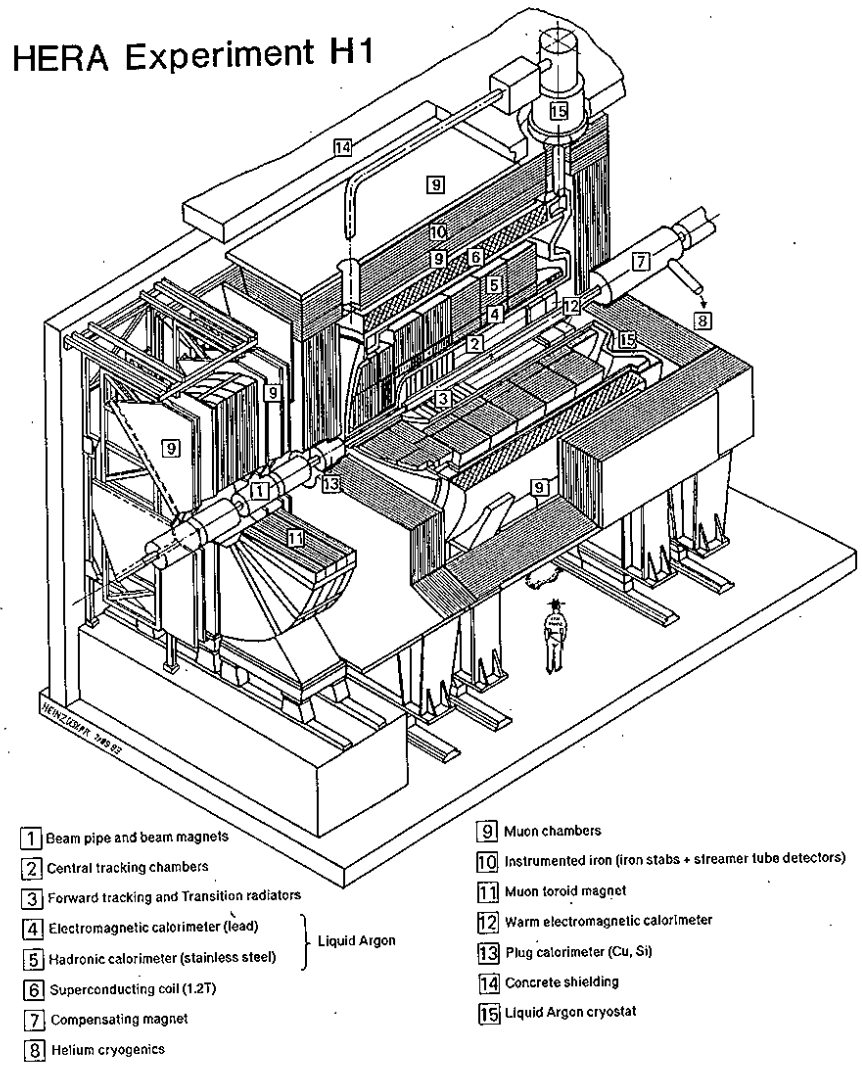

Figure 26: The H1 detector at HERA consists of tracking detectors inside the field of a superconducting magnet. They are surrounded by elaborate calorimetry (liquid Argon, Iron, Lead-scintillator). A separate muon spectrometer is indicated on the left side.

steel absorbers. The total depth of the calorimeter varies between $8 - 4.5$ interaction lengths, depending on θ. The energy resolution for electrons is $\sigma_E/E = 0.12/\sqrt{E} \oplus 0.01\%$, and for pions $\sigma_E/E = 0.5/\sqrt{E} \oplus 0.02\%$. In contrast to the ZEUS calorimeter, the energy response of pions and electrons with equal energies are different, and require offline corrections according to the

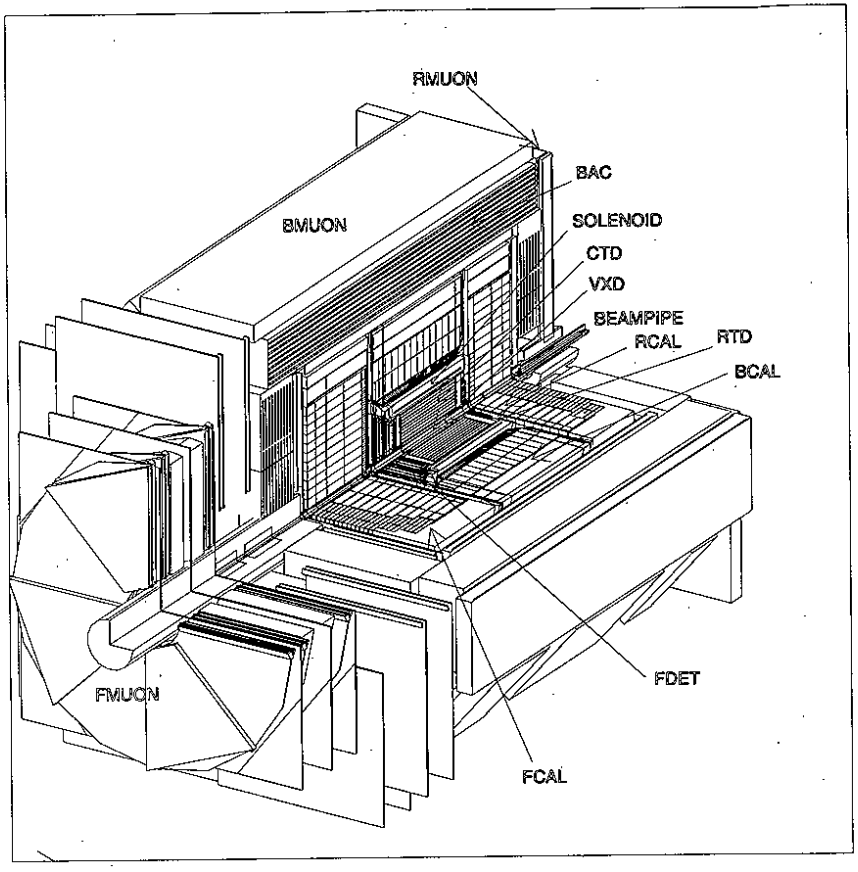

Figure 27: The ZEUS detector at HERA consists of tracking detectors (VXD, CTD, FDET, RDET) inside the field of a warm magnet. They are surrounded by a Uranium-scintillator calorimeter with photomultiplier read-out (FCAL, BCAL, RCAL), and an Iron calorimeter (BAC). Muon detection is provided (BMUON, RMUON, FMUON).

shower shape and the energy. In this H1 calorimeter not only was the depth adapted to the boost of the photon-proton center of mass system, but also the cell sizes were optimized according to the asymmetric beam energies: fine granularity was built in the proton direction with the cell sizes as small as 3×3 cm^2, increasing with θ. In photoproduction processes, this calorimeter is therefore well suited to study the hadronic final state in the region around the γp center of mass system.

The electron direction was previously covered by a lead scintillator calorimeter BEMC in the range $151° \leq \theta \leq 177°$. It consisted of an electromagnetic section with a depth of 22.5 radiation lengths. The energy resolution for electrons was $\sigma_E/E = 0.1/\sqrt{E}$. Since the 1995 data taking

period the BEMC has been replaced by a scintillating fiber calorimeter with photomultiplier read-out.

Both experiments have verified the hadronic energy scale of the calorimeters to the level of 5%, based on comparisons of data and simulated events:

- The ZEUS experiment compared the summed transverse momenta of tracks pointing into jet cones and the calorimetric jet energy measurements in the central detector region.
- They studied the forward calorimeter energy scale with transverse energy balance in di-jet photoproduction events, where one jet points into the central, the other jet into the proton-forward region.
- The H1 experiment compared the transverse energy balance between the scattered electron and the hadronic final state in deep inelastic scattering events.

The calorimeters of both experiments are surrounded by Iron tail catchers which record energy leakage out of the calorimeters and provide muon identification. In the proton direction, separate devices were built to detect 1) muons, e.g. for charm analysis, 2) protons to study diffractive scattering, and 3) neutrons for measurement of the pion structure function.

The luminosity available to the experiments is measured via the Bethe-Heitler process $ep \to ep\gamma$ which is predicted by QED theory. Both experiments have two electro-magnetic calorimeters in the electron direction with photomultiplier read-out, a photon detector for scattering angles below 0.5 mrad at a distance of ~ 100 m away from the experiments, and an electron detector for scattering angles below 6 mrad at around 30 m (Fig.28). The detectors consist of TlCl/TlBr crystals in the case of H1 with a resolution of $\sigma_E/E = 0.1/\sqrt{E}$. The ZEUS experiment has lead-scintillator calorimeters with similar resolution. The luminosity can be calculated from a simultaneous e and γ tag. Since the background rate in the photon detectors turned out to be negligible, the luminosity is actually calculated from the events in the photon tagger, where no complicated magnetic beam optics have to be simulated to determine the acceptance of the detector.

In the case of γp interactions the electron detectors of the luminosity systems are especially important. About 40% of the events with scaled photon energies between $0.2 < y < 0.8$ and photon virtuality below $Q^2 < 0.02$ GeV^2 have the scattered electron tagged in these detectors: the electron tag ensures that the interacting photon is quasi-real.

In the ZEUS experiment the main triggers used for photoproduction analysis are calorimeter triggers where towers were formed with low energy thresholds of 0.4 (1.0) GeV in the em (had) sections. They were used in coincidence with an energy deposit in the electron tagger above $E \geq 5$ GeV, or as a stand-alone trigger with a summed energy requirement of $E \geq 10$ GeV.

In the case of H1, the main trigger is an energy deposit in the electron detector above $E \geq 4$ GeV in coincidence with at least one track seen by the central drift chamber trigger with a transverse momentum above $p_t \geq 450$ MeV.

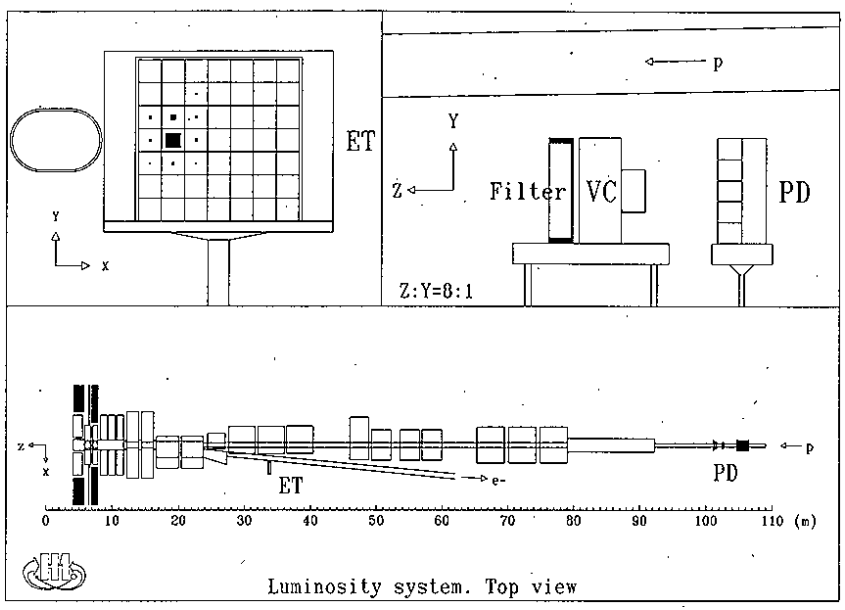

Figure 28: The H1 Luminosity system consists of an electron detector (ET) and a photon detector (PD). The lower picture shows a top view of the beam line relative to the interaction point in the direction of the scattered electron. The upper left picture shows the front view of the electron tagger together with a typical electron signal. The upper right picture shows the side view of the photon detector with a lead filter and a veto counter in front as a protection against synchrotron radiation.

Summary: photon–proton interactions at HERA

- At the HERA ep collider, quasi-real photons are emitted by the leptons. Quarks and gluons of the photon are probed by the partons of the proton at γp center of mass energies up to $\sqrt{s_{\gamma p}} = 300$ GeV.
- Photon–proton interactions are studied with the two multi-purpose detectors H1 and ZEUS.
  1. The collisions of quasi-real photons with protons are identified by leptons which scatter through small angles and are measured in the electron detectors of the luminosity system. Events where the electron disappears undetected at small scattering angles are also assigned to photoproduction processes.
  2. For studies of the hadronic final state, the detectors were optimized differently. The H1 liquid Argon calorimeter has fine granularity in the central γp collision region. This enabled detailed studies of the transverse energy flow and multiple parton inter-

actions. The ZEUS Uranium calorimeter covers a large range of the photon fragmentation region. This enabled studies of the direct photon processes and the photon remnant jet. Both experiments studied the parton distributions of the photon by measurements of the differential jet rates.

3. For studies of high p_t charged particle production both experiments have tracking detectors inside a magnetic field which cover approximately 3 rapidity units of the photon fragmentation region. These devices enable studies of the parton content in the photon through differential cross section measurements.

5 Verification of QCD predictions in γp scattering

In this section we want to test the following QCD predictions for hard photoproduction at HERA:

1. Hard scattering between the partons of the photon and the proton should be seen. Such γp interactions lead to particles with large transverse momenta and jet production.
2. Direct and resolved γp interactions should exist. In the LO approximation of perturbative QCD they can be distinguished by photon spectator particles which should appear only in the case of resolved photon scattering.
3. Direct and resolved γp interactions should have different distributions of the parton scattering angle. This can be studied by distributions of the jet rapidities in di-jet events.
4. Higher order QCD effects should appear: in di-jet events they cause an imbalance between the jet transverse energies. Multi-jet production should be observed.

5.1 Hard scattering

5.1.1 Transverse momentum spectra of particles

The first question is: do we see hard parton–parton scattering processes at all ? One possibility of answering this is the analysis of single inclusive particle spectra. This has been successfully used e.g. in proton–proton scattering at the ISR in 1972 [COL-84]. While studying π° production for $\theta \approx 90°$, they found two components in the transverse momentum spectrum (Fig.29):

(a) At small transverse momenta $p_t < 1$ GeV, the p_t spectrum was found to decrease exponentially as $\exp(-b\,p_t)$ with $b = 6$. This region corresponds to soft hadronic collisions.

(b) At large transverse momenta $p_t > 2$ GeV, they measured an excess of high p_t particles which is described by a power law, in agreement with expectations from hard scattering processes.

Single particle spectra have also been measured by the H1 and ZEUS experiments in γp interactions [H1-94, ZEU-95E]. The ZEUS experiment measured charged hadron production in the central tracking detector which covers a large rapidity interval in the photon fragmentation region ($-3.4 < \eta_{\gamma p} < -0.8$). Hadrons with transverse momenta between $0.3 < p_t < 8$ GeV were selected. The scattered electron was required to be found at small angles in the electron detector of the luminosity system which ensured the collision of quasi-real photons with protons at photon virtualities below $Q^2 < 0.02$ GeV^2. The corresponding average γp CM energy was $\sqrt{s_{\gamma p}} = 180$ GeV. Two types of event sample were selected from the 1993 data taking period with an integrated luminosity of 0.4 pb^{-1}:

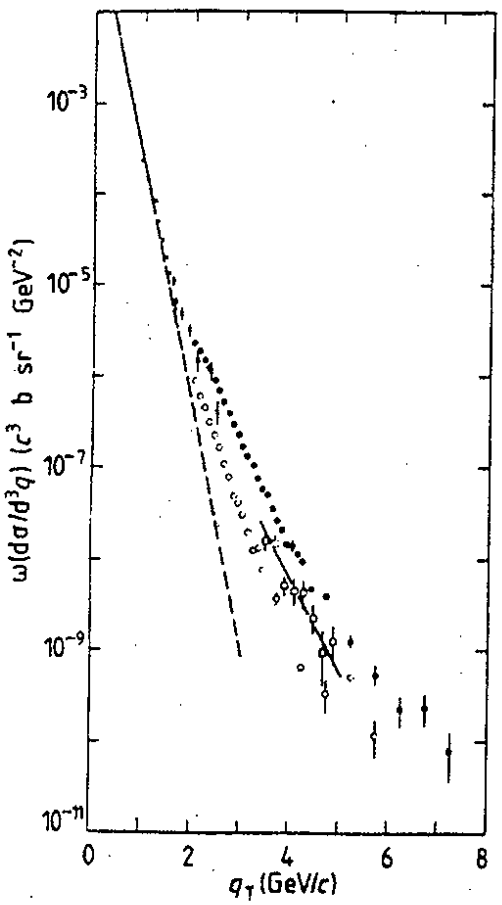

Figure 29: Differential cross section of π° production at 90° in pp collisions at the ISR. The symbols refer to different CM energies: open circles=31 GeV, open squares=44 GeV, full circles/crosses=53 GeV. The broken line is the extrapolation of $\exp(-6\,p_T)$ which describes the data at $p_T < 1$ GeV [COL-84].

1. Diffractive events were selected by requiring a rapidity region close to the proton direction which was free of hadrons (a so-called 'rapidity gap'). The invariant mass M_X of all hadrons in the final state was $M_X = 5$ GeV on average, a sample which essentially contains soft scattering processes. The shape of the resulting transverse momentum spectrum of the hadrons is shown in Fig.30 as open circles. The spectrum was fitted with an exponential function (dotted curve).

2. In a non-diffractive event sample (no requirement of a rapidity gap) two components were found in the transverse momentum spectrum (full circles):

   (a) At small transverse momenta $p_t < 1.2$ GeV, the data can again be described by an exponential fit. This region corresponds to soft collisions between the photon and the proton.

   (b) At large transverse momenta $p_t > 1.2$ GeV, the data follow a power law shape, as expected for partonic scattering processes between the photon and the proton. A fit to the functional form $A(1 + p_t/B)^{-n}$ gave $n = 7.25 \pm 0.04$.

Also shown in the Fig.30 is a next-to-leading order QCD calculation as the full curve which slightly overshoots the data [KNI-94]. The dash-dotted curve represents the shape of a power law fit to data from $\overline{p}p$ collisions at similar CM energies $\sqrt{s_{\overline{p}p}} = 200$ GeV [UA1-90]. These data fall significantly more steeply ($n = 12.14 \pm 0.39$) than the photoproduction data and indicate the different parton distributions of photons and protons, and the presence of direct photon processes.

Two important conclusions can be drawn from these measurements and the comparison with the QCD calculation:

- Parton collisions in photoproduction events at HERA are observed. At peak luminosities the rate of such events is large ~ 0.1 Hz.
- Quantitative descriptions of the data are obtained from NLO QCD hard scattering processes, with parton fluxes derived from standard photon and proton parton parameterizations, and fragmentation functions determined with e^+e^- and $\overline{p}p$ data. These results confirm QCD theory and show that the quark distribution functions from DIS $e\gamma$ scattering are applicable to the photoproduction data. Later we will discuss how the HERA results improve the knowledge of the parton distributions in the photon (section 7).

5.1.2 Jet production and jet universality

The second proof of the existence of hard scattering processes in photon-proton collisions was the observation of jets with large transverse energy. Their existence is beyond any doubt: the jets can be seen 'by eye' on event displays. In Fig.31 a photoproduction event, observed with the H1 detector, is displayed demonstrating that the individual jets are in fact strongly focused energy depositions. This event is a candidate for a direct photon processes, since no energy deposition of a photon remnant is observed in the direction of the scattered electron. A candidate event for jet production from a resolved photon process is shown from ZEUS data in Fig.32: here a third jet is observed in the electron direction (right) which shows the particles of the photon remnant.

Before we draw quantitative conclusions from the comparison of jet rates in measured data and QCD calculations, we need to regard the following three topics:

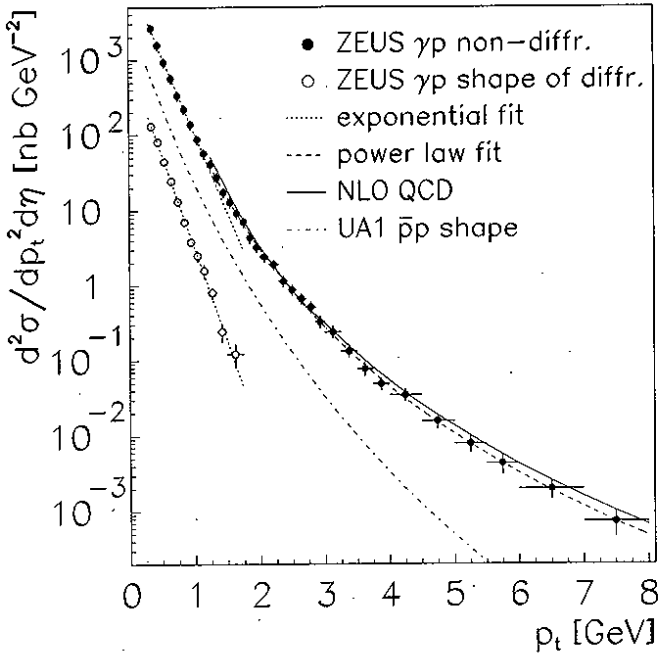

Figure 30: The inclusive differential particle cross section $d\sigma/dp_t$ is shown from ZEUS data as full circles [ZEU-95E]. The shape of a diffractive event selection is shown by the open circles. The dotted (dashed) curves represent exponential (power law) fits to the data. The full curve is a NLO QCD calculation by [KNI-94]. The dash-dotted curve is a power law fit to UA1 data from $\bar{p}p$ collisions at similar center of mass energies [UA1-90].

1. Jets from γp collisions were reported for the first time at HERA [H1-92, ZEU-92]. Are these focused particle bundles of the same jet type as observed in e.g. $\bar{p}p$ scattering?
2. The jets depend on their definition: experimentalists and theorists need to agree on a jet algorithm.
3. Are the jets described by QCD calculations?

Jet algorithms

Several algorithms for the jet definition have been studied in γp interactions (e.g. [PFE-94]) which can be classified as 'cone' and 'cluster' algorithms.

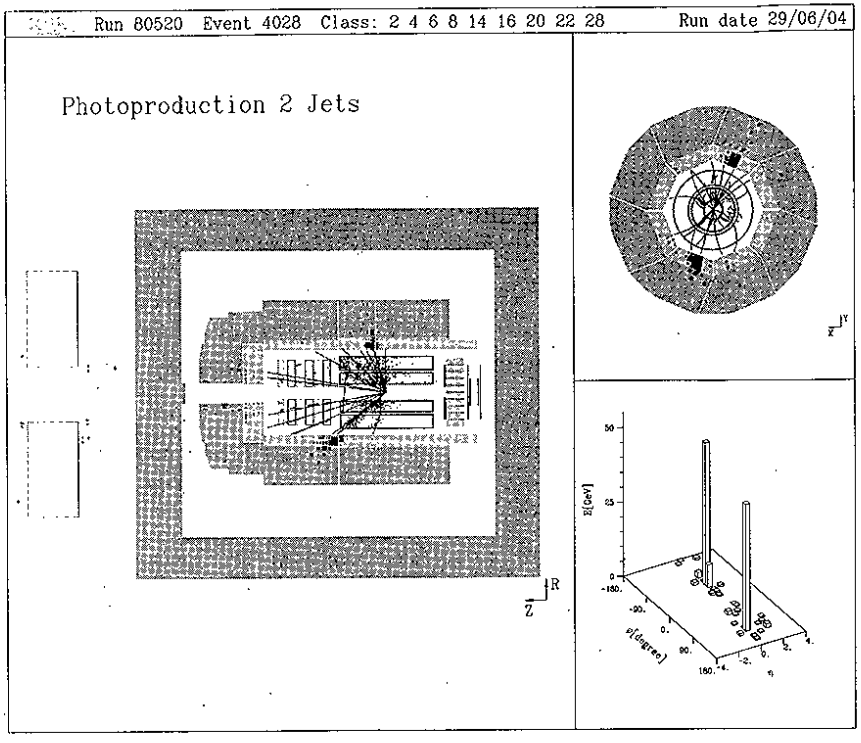

Figure 31: Direct photoproduction of two jets: the side view of the H1 detector is shown on the left, where the proton comes from the right, the electron from the left side. Some particles of the proton spectator are shown close to the beam pipe on the left side of the detector. The electron scattered through a small angle and was not detected. The two jets in the central part of the detector are back-to-back in the plane transverse to the beam axis (upper right). The histogram shows the energy weighted jet positions in the pseudo-rapidity and azimuthal directions (lower right).

Most of the HERA photoproduction analyses use a cone algorithm for the jet reconstruction which follows the recommendations of the 'Snowmass accord' [HUT-90]. Here a two-dimensional grid is used in the plane of the pseudo-rapidity η and the azimuthal angle φ, requiring a minimum energy deposit in one of the cells of the grid. The size of the cone is typically chosen to be $R = \sqrt{\Delta\eta^2 + \Delta\varphi^2} = 1$, or $R = 0.7$. The transverse jet energy is simply calculated from the sum of the transverse energies found inside the cone $E_i^{jet} = \sum_i E_t(\eta_i, \varphi_i)$. The jets are only accepted if the summed energy is above some threshold, which is typically chosen around 8 GeV at HERA. The rapidity and azimuthal positions of the jet axis are calculated from the weighted energy sums of the contributing cells, e.g.: $\eta^{jet} = \sum_i (E_t(\eta_i, \varphi_i) \times \eta_i)/E_i^{jet}$. The cone algorithm cuts out the transverse energy of a clearly defined area in (η, φ) space. With this feature it is well suited for jets in an environment similar to hadron-hadron collisions, where migrations of

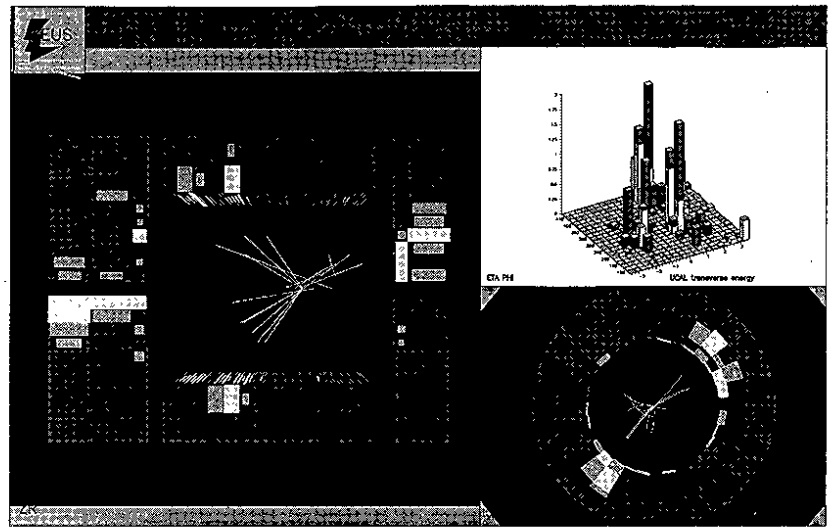

Figure 32: Resolved photoproduction of jets: the figure on the left shows the side view of the ZEUS detector with two jets at large polar angles θ going to the left and a third jet in the scattered electron direction (to the right) which results from the photon remnant. The two jets in the central part of the detector are back-to-back in the plane transverse to the beam axis (lower right). The histogram shows the energy weighted jet positions in the pseudo-rapidity and azimuthal directions (upper right).

energy into and out of the jet cone need to be understood.

Cluster algorithms are better suited to finding jets at small transverse energies and at small angles θ. Such algorithms are used for dedicated analyses, like e.g. the K_t jet algorithm [CAT-92] for a study of the particles fragmenting from the photon spectator partons (see section 5.2). This algorithm decomposes the event topology into large combined 'clusters' of energy depositions: based on the opening angle between two energy depositions E_n, E_m and their energy, the quantity $K_t = min(E_n^2, E_m^2)(1 - \cos\theta_{n,m})$ is calculated for all two-cluster combinations. The pair with the minimum K_t value is combined into a common cluster. The process is repeated until no two clusters can be found with K_t below $\xi^{cut} E_t^2$, where E_t is the total transverse energy found in the event, and ξ^{cut} is a cut-off parameter.

Properties of jets in γp, $\bar{p}p$ and $\gamma\gamma$ collisions

The shape of jets from γp scattering

In Fig. 33a the uncorrected transverse energy flow in the azimuthal direction $\Delta\varphi$ around the jet with the highest E_T^{jet} in events with at least two jets is shown from H1 data [H1-96A]. The jets were found in the photon fragmentation region between $-2 \leq \eta_{\gamma p}^{jet} \leq -1$ where detector corrections are small. The transverse jet energies are around $E_T^{jet} = 10$ GeV summed in a cone

of size $R = 1$. The energy flow was integrated in a slice of $|\eta_{\gamma p} - \eta_{\gamma p}^{jet}| \leq 1$ around the jet axis. The two jets usually deviate from a back-to-back configuration in the azimuthal angle $\Delta\varphi = \pi$. Here $\Delta\varphi$ was defined such that $-\pi \leq \Delta\varphi \leq 0$.

The profile of the jets has approximately Gaussian shape and is described by an empirical fit (full curve) which can be used to determine three features of the jet profiles: the amplitude, the width Γ and the energy level of the underlying event (also called the 'jet pedestal') [H1-96A]. The results of a LO QCD calculation including fragmentation effects and a detailed simulation of the detector effects (dashed histogram: PYTHIA) gives a satisfactory description of the profile in this rapidity region.

This agreement is no longer there in the central rapidity region of the γp collision $\eta_{\gamma p}^{jet} \approx 0$ (Fig.34 from H1 data [RIC-96]). Here the PYTHIA generator without multiple interaction predicts too little transverse energy flux outside the jet area (dotted histogram). This problem cannot be cured by changing the fragmentation of the hard parton scattering process, but is understood as an effect of beam remnant interactions (full histogram: PYTHIA with multiple parton interactions) which will be discussed in section 6.2.4.

QCD predictions for jet shapes

Two predictions on jet profiles result from a QCD calculations on the parton level which include higher order effects [KRA-94B]:

1. The jets of γp and $\bar{p}p$ with equal scaled transverse jet energy

$$x_T = 2E_t^{jet}/\sqrt{s} \tag{46}$$

   should have the same jet shape. The authors recommend that the normalization of the CM energy should be $\sqrt{s_{\bar{p}p}}$ for the proton-anti-proton data, and $\sqrt{s_{ep}}$ for the photoproduction data.

2. The width of jets should decrease with increasing jet energy. In the $\Delta\varphi$ projection the decrease can be approximated by a $1/E_t^{jet}$ behaviour.

Both the simple scaling behaviour (46) and the dependence of the jet width on E_t^{jet} are phenomenological interpretations of the calculated results.

Comparisons of the jet shapes from γp, $\bar{p}p$ and $\gamma\gamma$ processes

In Fig.35 the fitted full width at half maximum above the pedestal, Γ, is shown for jets between $-2 \leq \eta_{\gamma p}^{jet} \leq -1$ as a function of $x_T = 2E_t^{jet}/\sqrt{s_{ep}}$ from H1 data (full points [H1-96A]). The measured jets become narrower with increasing jet energies, and can be fitted by the functional form $1/E_t^{jet}$ (curve).

Published results on jet profiles from $\bar{p}p$ experiments [UA1-83, UA1-88] (e.g. Fig.33b) have been fitted with the same fitting function [H1-96A]. The resulting jet widths are shown in the same Fig.35 as open symbols for different jet energies and beam energies. Within the error bars, the widths of γp jets are compatible with the jet widths determined in the $\bar{p}p$ data at the same value of x_T.

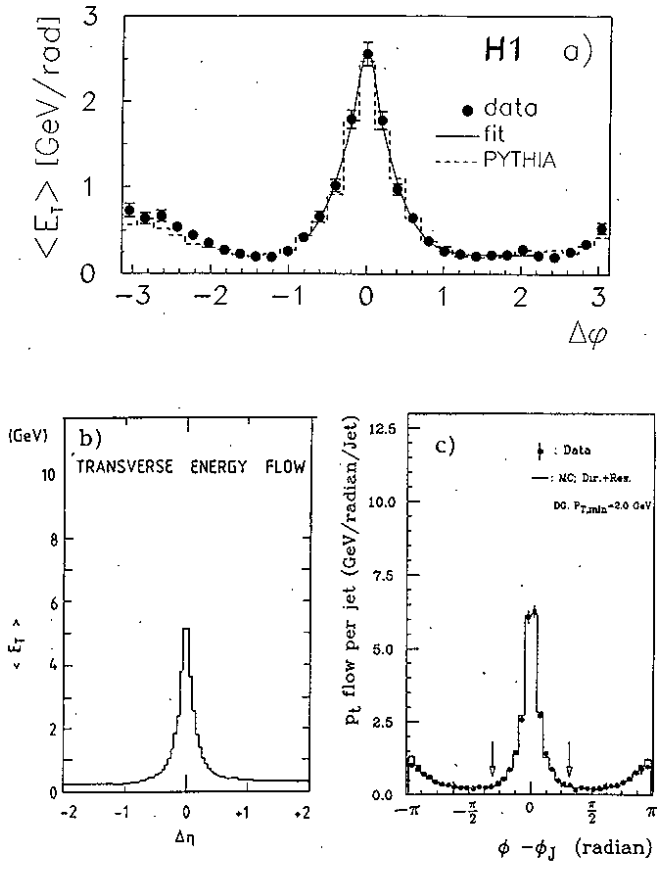

Figure 33: Observed transverse energy flow around a jet axis from different processes: γp, $\overline{p}p$ and $\gamma\gamma$ collisions.

a) Photoproduction of jets with transverse energy $E_t^{jet} = 10$ GeV is shown from H1 data in a projection onto the azimuthal direction [H1-96A]. The jets have rapidities between $-2 \leq \eta_{\gamma p}^{jet} \leq -1$. The transverse energy of a second jet is seen at $\Delta\varphi \sim \pm\pi$. The axis of this jet had to be at $\Delta\varphi \leq 0$. The latter requirement allows to measure the energy outside of jets at $\Delta\varphi = 1.5$. The full curve is an empirical fit to the data. The dashed histogram is a calculation of the LO QCD generator PYTHIA including a detailed simulation of the detector effects.

b) Jet shapes measured in proton–anti-proton collisions are shown in the rapidity projection for jets between $30 \leq E_t^{jet} \leq 40$ GeV [UA1-83].

c) The azimuthal projection of jet profiles are shown for jets above $E_t^{jet} \geq 2.5$ GeV which were observed in the collisions of two quasi-real photons [TOP-93]. The full histogram is the calculation of a LO QCD generator.

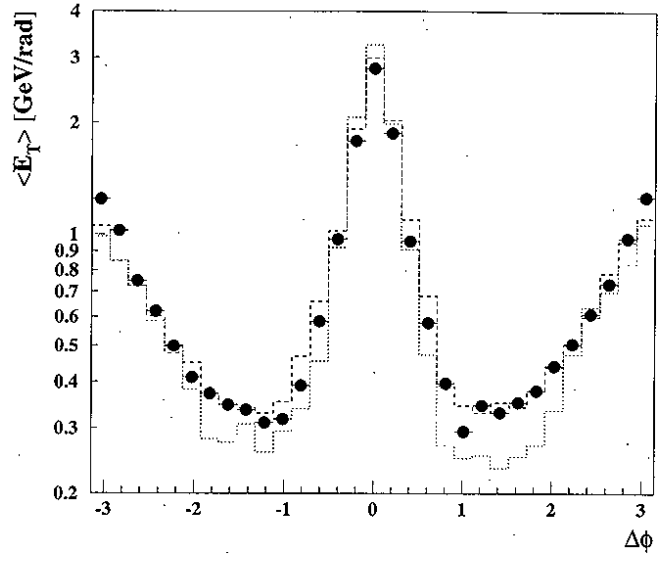

Figure 34: The observed transverse energy flow around the jet axis for jets with transverse energies between $10 \leq E_t^{jet} \leq 12$ GeV is shown in the central rapidity region of the γp collision $0 < \eta_{\gamma p}^{jet} < 0.5$ (H1 data [RIC-96]). The dotted histogram is the calculation of the LO QCD generator PYTHIA for single hard parton scattering processes per event including a detailed simulation of the detector effects. This calculation cannot describe the measured energy flow next to the jets at $\Delta\varphi = 1.5$. The dashed histogram shows the calculation of the same generator including multiple parton scattering processes which gives an improved description of the measured jet shape.

A word of caution is needed here for the comparison of the data with the QCD calculations using partons: although the measured jet shapes are compatible with the QCD expectations, we do not know the size of the fragmentation effects which have to be added to the QCD calculation for safe comparisons.

In Fig.33c, a profile of jets from the collisions of two quasi-real photons are shown for jet transverse energies above $E_t^{jet} \geq 2.5$ GeV (full circles) [TOP-93]. This jet profile was also fitted with the same fitting function. The width of these jets is shown in Fig.35 by the open circle at $x_T = 2E_t^{jet}/\sqrt{s_{ee}}$. As the average transverse jet energy we use here $E_t^{jet} = 3$ GeV. The jets from $\gamma\gamma$ collisions show a shape which is compatible with the simple scaling law (46).

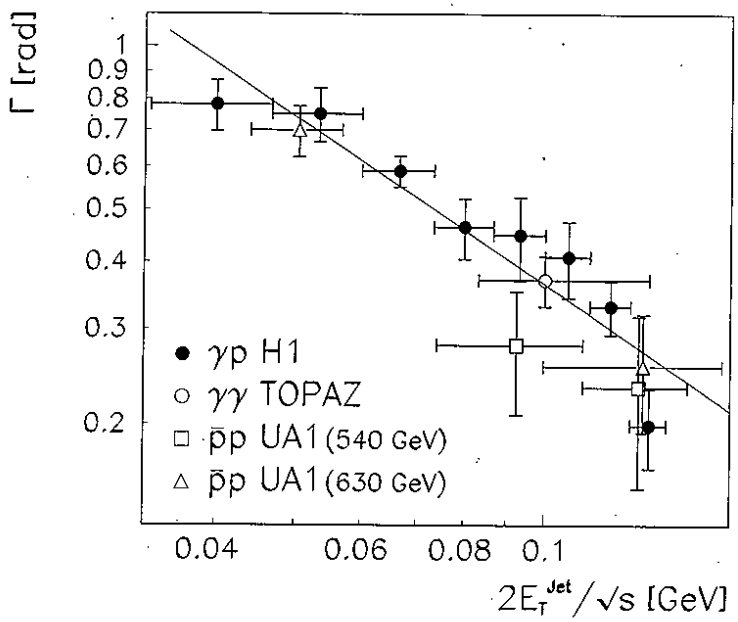

Figure 35: The jet width Γ was determined at half maximum above the energy level measured next to the jets. The width is shown as a function of the ratio of the transverse jet energy over the collision energy. The full points are the results of fits to H1 photoproduction data [H1-96A] where the jet energies were normalized to the ep center of mass energy, following [KRA-94B]. The full line is a fit to the data proportional to $1/E_t^{jet}$ which is the functional form expected from QCD calculations. The open squares and triangles show the results of the same fits applied to jet shapes measured in $\bar{p}p$ collisions [UA1-83, UA1-88]. The open circle shows a fit to the TOPAZ $\gamma\gamma$ data (Fig.33 [TOP-93]).

In summary:

- The jets observed in photoproduction events show a Gaussian shape.
- Narrowing of the jet width with increasing jet transverse energies is observed.
- Jet parameters of γp, $\bar{p}p$ and $\gamma\gamma$ scattering are related by a simple scaling law depending on the CM beam energy $E_t^{jet}/\sqrt{s}(ep) = E_t^{jet}/\sqrt{s}(\bar{p}p) = E_t^{jet}/\sqrt{s}(\gamma\gamma)$. These results support the idea that jets are universal.

Transverse jet energy cross section

Jets with sufficiently high transverse energy reflect the direction and energy of scattered partons. The parton–parton cross sections are predicted to fall as p_t^{-n} with $n = 4$. The transverse jet energy cross section is however folded with the parton distribution functions and is influenced by fragmentation effects which jointly modify the power n.

In Fig.36 the measured differential transverse jet energy cross section $d\sigma/dE_t^{jet}$ is shown from a ZEUS analysis [ZEU-95A]. The jets were defined by a cone algorithm with cone radius $R = 1$. They have transverse jet energies above $E_t = 8$ GeV and were integrated in the rapidity interval $-1 < \eta^{jet} < 1$. The event kinematics correspond to photon virtuality below $Q^2 = 4$ GeV^2, and a large interval in the photon–proton CM energy $130 < \sqrt{s_{\gamma p}} < 270$ GeV. The measurement is based on 1993 data with an integrated luminosity of 0.55 pb^{-1}. The data can be described by a power law distribution $(E_t^{jet})^{-n}$ with $n = 5.8$, where the power n is larger than $n = 4$ due to the convolution with the input distributions.

In the same Fig.36, the data are compared to a NLO QCD calculation [KLA-95A]. Here the parton distribution functions of MRSD$^-$ (proton) and GRV-HO-DIS (photon) were used. The dotted curve represents the direct photon contribution which is compatible with the data at large $E_t^{jet} > 20$ GeV. The resolved photon processes (dashed curve) dominate the region around $E_t^{jet} = 8$ GeV. The total calculation (full curve) gives a shape similar to that observed in the data. The total rate is found to be above the data which indicates that the parameterizations of the parton densities need to be adjusted.

In summary:

- As in the case of particle production, the measured transverse jet energy cross section confirms the QCD parton picture of hard photon–proton interactions.

5.2 Resolved photon interactions

Resolved γp interactions can be identified by the measurement of the particles from the photon remnant. Here we want to check the existence of the photon remnant and study its properties. Since the remnant particles result from partons, they should form a jet. Such jets would then reflect the intrinsic transverse momenta k_t^γ of the partons from the photon. The k_t^γ distribution is expected to be broader than that of hadrons due to the anomalous component of the photon.

Transverse energy flow

The photon remnant energy should be large for small fractional parton energy x_γ, and should vanish in the case of direct γp interactions ($x_\gamma \equiv 1$). Therefore the study of the x_γ dependence of the transverse energy flow in the photon direction should the reveal the photon remnant.

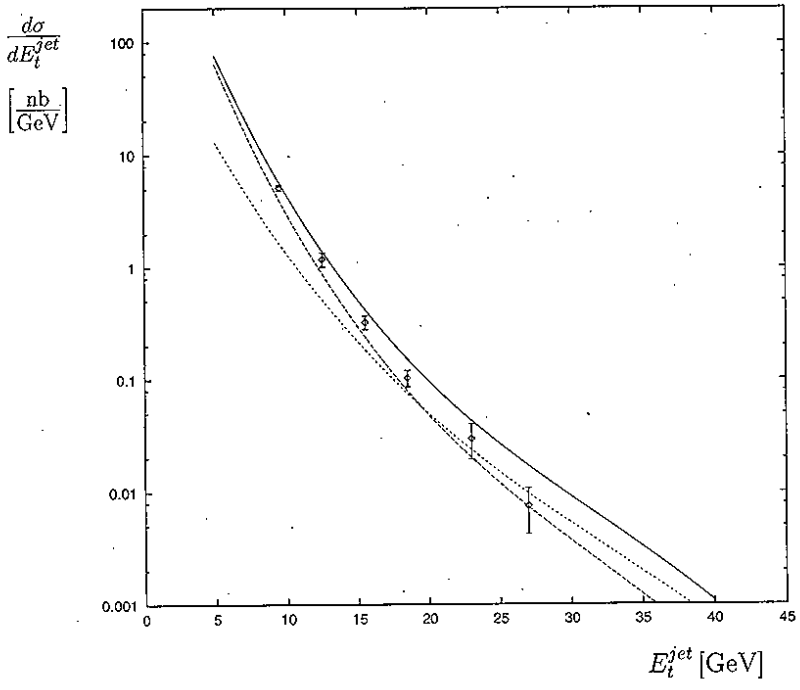

Figure 36: The inclusive differential jet ep cross section $d\sigma/dE_t^{jet}$ is shown as a function of the transverse jet energy from ZEUS data [ZEU-95A]. The jet rapidity range was between $-1 \leq \eta^{jet} \leq 1$. The event kinematics corresponds to $130 \leq \sqrt{s_{\gamma p}} \leq 270$ GeV and $Q^2 < 4$ GeV^2. The full curve represents a NLO QCD calculation using the parton distribution functions MRSD$^-$ for the proton and GRV-HO for the photon [KLA-95A]. The contributions of the direct (dotted) and resolved (dashed) photon processes are shown separately.

In LO QCD x_γ can be calculated from the two scattered partons using eq.(37). A good estimate of x_γ is given by the corresponding jet quantities in events with two jets:

$$x_\gamma^{jets} = \frac{E_t^{jet1} e^{-\eta^{jet1}} + E_t^{jet2} e^{-\eta^{jet2}}}{2E_\gamma} \tag{47}$$

In Fig.37 the transverse energy flow is shown as a function of the rapidity difference $\Delta\eta$ relative to jets with rapidity between $0 < \eta^{jet} < 1$ (from H1 di-jet data [HUF-95]). The jets had transverse energies above $E_t^{jet} > 7$ GeV. The photon energy E_γ was determined from the energy of the scattered electron which was measured in the luminosity detector (eq.(34)). In order to exclude the energy of the second jet, energy deposits were only integrated in the azimuthal range

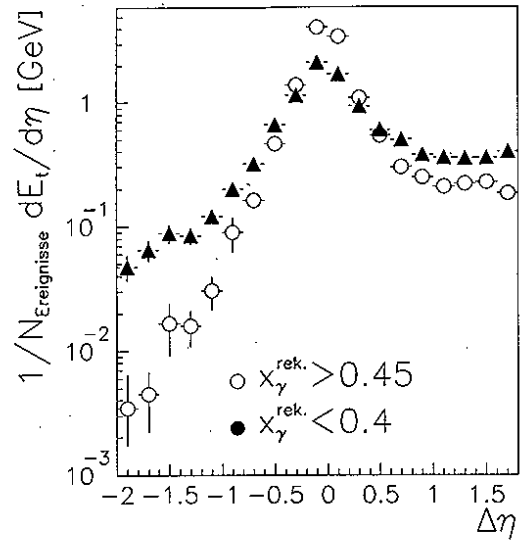

Figure 37: The transverse energy distribution around jets is shown as a function of the rapidity distance from the jet axis in two intervals of the fractional parton energy x_γ^{jets} (H1 data, [HUF-95]). The jets had transverse energies above $E_t^{jet} = 7$ GeV, and the jet rapidity was between $0 < \eta^{jet} < 1$. The transverse energy was integrated in the azimuthal slice $|\varphi - \varphi^{jet}| < 1$ in order to exclude the energy of a second jet in the event which is needed to calculate x_γ^{jets} (eq.(47)).

$|\varphi - \varphi^{jet}| < 1$. The data are shown in two intervals of $x_\gamma^{jets} > 0.45$ and $x_\gamma^{jets} < 0.4$.

At low x_γ^{jets} the transverse energy flow in the photon direction ($\Delta\eta < 0$) is larger by one order compared to the high x_γ^{jets} data. This enhanced energy flow shows the existence of the photon remnant, and therefore the presence of resolved photon interactions.

In the proton direction ($\Delta\eta > 0$), the transverse energy flow is also enlarged, here by a factor two, for the low x_γ^{jets} data relative to the high x_γ^{jets} events. This observation is explained by initial state parton radiation and multiple parton interaction effects (Figs.43,47).

The photon remnant jet

Particles resulting from the photon spectator partons should form a jet. The ZEUS detector is well suited to study hadronic energy depositions close to the beam pipe in the γ direction. The following analysis is based on three jet events from an integrated luminosity 0.55 pb^{-1} in the kinematic range $Q^2 < 4$ GeV^2 and $130 \leq \sqrt{s_{\gamma p}} \leq 270$ GeV [ZEU-95D].

In order to detect a potentially small transverse energy deposition, the K_T jet algorithm was used to decompose the event into three so-called energy 'clusters' (see section 5.1.2). If two

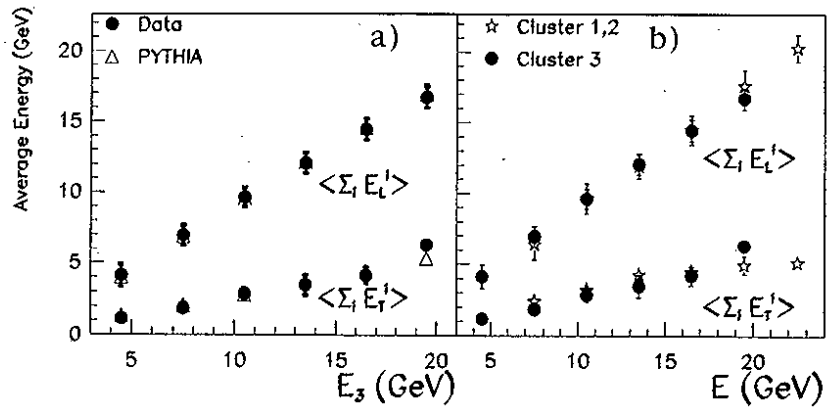

Figure 38: a) The longitudinal and transverse energy distributions with respect to the axis of the photon remnant cluster are shown from ZEUS data (points) [ZEU-95D]. The open triangles represent the calculations of the PYTHIA generator.
b) The same photon remnant energy distributions are compared to the two jets from the hard scattering process (stars), which demonstrates that the photon remnant forms a jet.

clusters had transverse energies above $E_t^{cluster} \geq 6$ GeV and were at rapidities below $\eta^{jet} \leq 1.6$, the third cluster turned out to be on average in the photon fragmentation region, well away from the central γp collision region. Such configurations can be interpreted as the result of a hard resolved γp scattering process: the two leading E_t clusters reflect the jets from the hard parton scattering, and the third cluster is the energy deposition resulting from the photon remnant.

The energy distributions along and around the axis of the third cluster were found to be well collimated. In Fig.38a the longitudinal and transverse energy distributions with respect to the cluster axes are shown for this cluster as a function of the cluster energy E_3 (full points). A LO QCD calculation of the PYTHIA generator for single hard parton interactions gives a good description of this energy distribution (open triangles). In Fig.38b the same quantities are shown for all three clusters as a function of the cluster energy (points for the photon remnant, stars for the high E_t clusters). Within the error bars the third cluster shows the properties of a jet, as one would expect from the partonic picture of photon-proton interactions.

Transverse momenta of the partons from the photon

In the anomalous photon coupling the photon splits into a $q\bar{q}$ pair which can have large transverse momenta k_t^γ relative to the γ direction. The distributions of k_t^γ are expected to follow a power law, rather than a Gaussian distribution, which one would expect for partons from hadrons [SCH-93, DRE-93, CHY-94, SCH-94]. The k_t^γ distribution should be reflected in the photon remnant jet distributions.

In Fig.39a the rapidity distribution of the third cluster is shown between $-4 \leq \eta_3 \leq 2$ from the ZEUS analysis. The region around $\eta_3 \sim 2$ corresponds to the central γp collision region. The

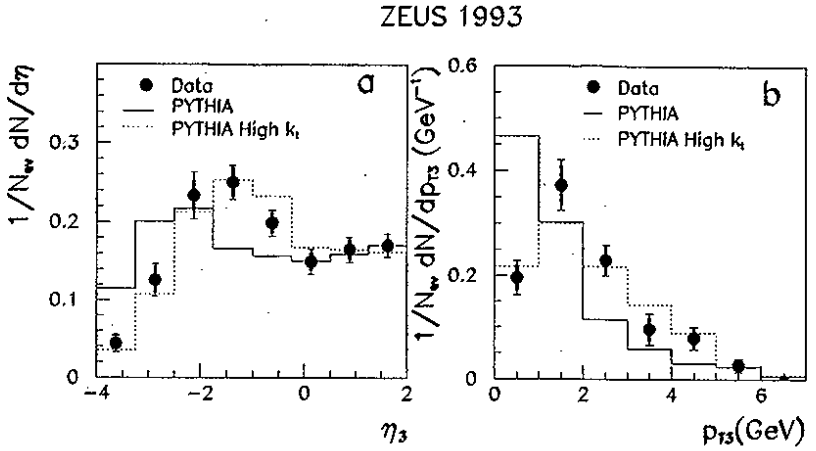

Figure 39: a) The corrected rapidity distribution of the photon remnant jet is shown from ZEUS data [ZEU-95D]. The full histogram represents the LO QCD calculation of the PYTHIA generator using a hadronic type distribution (Gaussian) for the parton transverse momenta k_t^γ from the photon. The dotted histogram shows the same calculation with a power law like distribution for k_t^γ.
b) The corrected transverse momentum distribution of the photon remnant jet is shown for jet rapidities below $\eta_3 < -1$. Histogram assignment is as in a).

distribution was corrected for detector effects, including energy losses in the beam pipe, using an unfolding procedure [DAG-94]. The full histogram in the figure represents the calculation of the PYTHIA QCD generator, using here a Gaussian, i.e. hadronic, distribution of the parton momenta relative to the photon direction. This calculation does not describe the data. The dotted histogram shows the same QCD calculation, using a power law type k_t^γ distribution of the partons in the photon: $dN/dk_t^2 \propto ((k_t^\gamma)^2 + k_0^2)^{-1}$ with $k_0 = 0.66$. This calculation gives a fair description of the data.

In Fig.39b the transverse momentum distribution of the third cluster is shown for rapidities below $\eta_3 \leq -1$. While in the central γp collision region $\eta \approx 2$ such jets may originate from QCD radiation effects, these clusters are safely inside the photon fragmentation region. The p_{t3} spectrum is much harder in the data compared to the calculation with the Gaussian k_t^γ distribution. Here also the calculation with the power law like k_t^γ distribution is compatible with the data.

Summary: resolved γp interactions

- The measurement of photon remnant particles in jet events demonstrates the presence of resolved γp interactions.

- Studies of the energy flow distribution in the photon fragmentation region show that the photon spectator partons form a jet.
- The transverse energy E_t^{jet} of the photon remnant jet reflects the transverse momentum k_t^γ of the partons from the photon. The measured E_t^{jet} distribution is much harder than expected from a hadronic type k_t^γ distribution and reflects the anomalous photon component.

5.3 Direct photon interactions

The life time of the photon fluctuations into $q\bar{q}$ pairs is finite according to the uncertainty relation (eqs.(3,8)). So, the photon must also exist in its bare state when interacting with a nucleon.

Two methods have been used for the search of direct photon–nucleon interactions:

1. QCD theory predicts a relative suppression of the direct photon processes with respect to the resolved photon processes at small parton scattering angles $\hat{\theta}$ in the parton-parton CMS, i.e. small transverse parton momenta $\hat{p}_t$ (Fig.11). Therefore, searches for deviations from resolved photon processes are most promising at large transverse parton momenta.
2. In the case of direct photon interactions, the full photon energy enters the parton scattering process. Studies of the distribution of the parton energy fraction x_γ should therefore show an enhancement at $x_\gamma = 1$.

Results of fixed target γN experiments

The fixed target experiments of the 1980is applied a nice trick: with the same detector they measured photon–nucleon and meson–nucleon scattering and compared the production of pions at large transverse momenta p_t. The NA14 experiment found a clear excess of π° production in γN scattering compared with meson-N interactions [NA14-86].

A similar excess of γp data was found in the production of charged hadrons by the WA69 experiment. This measurement is shown in Fig.40a [OME-89]. The difference in the measured cross sections could be explained well by QCD calculations of direct photon-nucleon interactions (Fig.40b). According to these results the photon can be decomposed into a vector meson and a direct component. No sign of the anomalous photon component, which was established by deep inelastic lepton-photon scattering experiments (Fig.18), was found at the CM energy $\sqrt{s_{\gamma p}} = 18$ GeV.

Di-jet measurements at HERA

At HERA the most interesting results come from the two-jet distributions of the parton energy fraction x_γ. The ZEUS analysis shown here was based on an integrated luminosity of 0.55 pb^{-1} [ZEU-94B]. The scattered electron was required to be absent in the main calorimeter corresponding to a virtuality of the photon below $Q^2 = 4$ GeV^2. The γp CM energy was between $130 \leq \sqrt{s_{\gamma p}} \leq 270$ GeV. Both jets had transverse energies above $E_t^{jet} \geq 5$ GeV, and rapidities in the interval $-1.125 \leq \eta^{jet} \leq 1.875$. The rapidity difference between the two jets

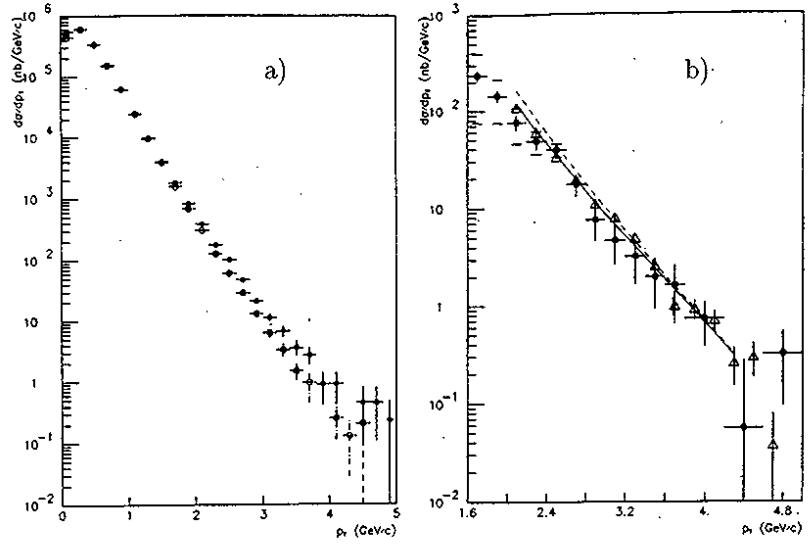

Figure 40: a) The differential cross sections of charged particle production in fixed target photon-proton (full circles) and meson-proton (open circles) scattering are compared as a function of the transverse particle momenta p_T [OME-89]. The meson-proton data were normalized to the photon-proton data at small $p_T < 1$ GeV.
b) The difference between the photon and meson data (full circles) is compared with a LO QCD calculation (open triangles) and with two NLO QCD calculations: the full curve represents the direct photon case, the dashed curve includes also the anomalous photon coupling.

had to be below $|\Delta\eta^{jet}| \leq 0.5$ which selected events with $\approx 90^\circ$ scattering in the parton-parton CMS.

The energy fraction of the parton from the photon x_γ was reconstructed using the two jets with the highest transverse energies in the event:

$$x_\gamma^{cal} = \frac{E_t^{jet1} e^{-\eta^{jet1}} + E_t^{jet2} e^{-\eta^{jet2}}}{\sum_{hadrons} E_t e^{-\eta}} \tag{48}$$

The photon energy was reconstructed using $E_\gamma = (\sum_{hadrons} E_t e^{-\eta})/2$. This gives on average a value which is smaller than the true photon energy, because in resolved photon-proton interac-

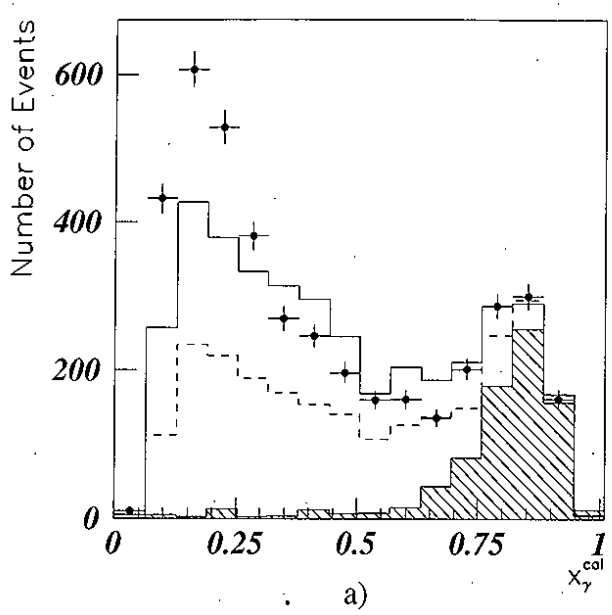

Figure 41: The observed 2-jet spectrum is shown as a function of the fractional energy of the parton from the photon side, using equation (48) (ZEUS Collab. [ZEU-94B]). The histograms represent LO QCD calculations using the HERWIG (dashed) and PYTHIA (full) generators for single hard parton scattering processes. The hatched histogram shows the direct photon contribution as calculated with the HERWIG generator.

tions particles of the photon spectator are lost in the beam pipe. Experimentally, the advantage of formula (48) is that uncertainties in the energy measurement, e.g. event by event fluctuations due to energy resolution effects, or uncertainties in the absolute energy scale of the calorimeter, cancel.

In Fig.41 the two-jet spectrum is shown as a function of the reconstructed energy fraction x_γ^{cal} of the parton from the photon. The distribution has two peaks, the large peak at $x_\gamma^{cal} = 0.2$ corresponds to resolved photon-proton scattering processes, the smaller peak at $x_\gamma^{cal} = 0.8$ is associated with the direct photon-proton interactions. The histograms in the same figure show LO QCD predictions of the generators HERWIG (dashed) and PYTHIA (full). Both were normalized to the peak at $x_\gamma^{cal} = 0.8$. Also shown is the direct photon contribution to the total rate as calculated by the HERWIG generator which demonstrates that the peak at large x_γ^{cal} is caused by direct photon events.

At small $x_\gamma^{cal} = 0.2$ the energy flow problems of generator programs with only single hard parton interactions per event becomes apparent. This is not relevant at large $x_\gamma^{cal} > 0.4$ (Fig.47). In the large x_γ region (Fig.41), the observed data are not purely direct photon interactions, but

are 'contaminated' by resolved photon interactions. Therefore, from this distribution alone, it is not possible to make an exact determination of the direct photon cross section which could improve our knowledge of the parton distributions in the proton. Instead, information on the parton distributions of the photon in the kinematic region $x_\gamma \approx 1$ can be obtained, where the error bars of the DIS lepton-photon experiments are sizable (Fig.16).

Summary: direct photon interactions

- The existence of direct photon interactions at small photon virtuality, which was demonstrated in fixed target γN experiments, was confirmed in γp collisions at HERA.
- The QCD prediction for the direct photon cross section is correct at CM energies $\sqrt{s_{\gamma N}} =$ 18 GeV, and is compatible with the HERA data at $\sqrt{s_{\gamma p}} = 200$ GeV, taking into account the uncertainties of the resolved photon contributions.

5.4 The parton scattering angle

A basic QCD prediction is that different sub-processes have different distributions of the parton scattering angle $\hat{\theta}$. E.g., the parton cross section as a function of $\cos\hat{\theta}$ varies much faster for resolved photon interactions compared to direct photon processes (Fig.11).

In di-jet events $\cos\hat{\theta}$ can be calculated from the rapidity difference between the two jets, eq.(33). Direct and resolved processes can be distinguished by the fractional parton energy x_γ (Fig.41). In Fig.42a, the shape of the measured preliminary $\cos\hat{\theta}$ distribution is shown from 1994 ZEUS data [CAS-96]. The full symbols refer to the resolved γp interactions, $x_\gamma < 0.75$, the open symbols reflect the direct γp processes $x_\gamma > 0.75$. Both distributions were normalized to one at $\cos\hat{\theta} = 0$. The measurements show a much steeper rise of the resolved γp angular distribution compared to the direct γp processes.

In the same Fig.42a, the data are compared to analytical LO (dashed) and NLO (full) QCD calculations [OWE-95]. Both calculations are compatible with the data. In Fig.42b, the data are compared to the predictions of two generators: PYTHIA (full curve) and HERWIG (dashed). The description of the PYTHIA generator is good, the HERWIG prediction is compatible with the data.

In summary:

- The basic QCD prediction, that different sub-processes have different distributions of the parton scattering angle, is confirmed in di-jet data.

5.5 Higher order QCD effects

Are higher order QCD corrections to the LO calculation needed to describe the data ? Such effects can be studied by the imbalance between the transverse energies of the leading E_t^{jet} jets or by the observation of multi-jet events ($n_{jet} > 2$).

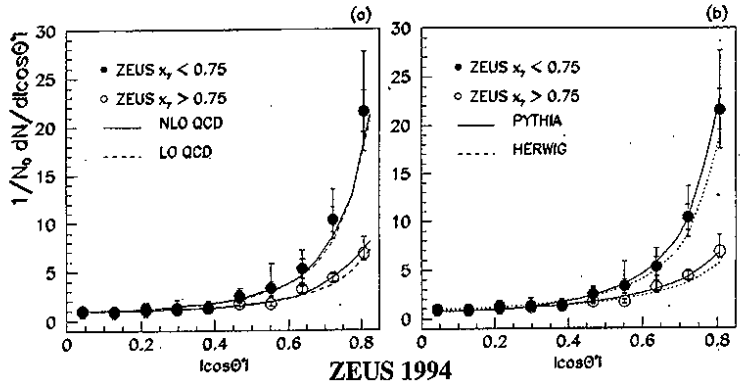

Figure 42: a) The distribution of the cosine of the parton scattering angle $\hat{\theta}$ is shown from di-jet events in two intervals of the parton fractional energy $x_\gamma > 0.75$ (open symbols) and $x_\gamma < 0.75$ (full symbols) (ZEUS PRELIMINARY: [CAS-96]). Both distributions were normalized to one at $\cos\hat{\theta} = 0$. The curves represent the predictions of analytical LO (dashed) and NLO (full) QCD calculations [OWE-95].
b) The data are compared to the predictions of two LO QCD generators: PYTHIA (full curve) and HERWIG (dashed).

In Fig.43a the shape of the transverse energy imbalance $\Delta E_t = E_t^{jet1} - E_t^{jet2}$ between two jets is shown from H1 data [RIC-96]. The data show a tail towards large values of ΔE_t. Both jets had transverse energies above $E_t^{jet} = 7$ GeV, collected in a cone of size $R = 0.7$, and rapidities between $-0.5 < \eta^{jet} < 2.5$. The reconstructed parton energy fraction x_γ^{jets} (eq.(47)) was $x_\gamma^{jets} > 0.4$ in order to reduce effects of multiple parton interactions (Fig.47). The rapidity distance between the two jets was $|\Delta\eta| < 1$ to have the same jet pedestal on average. The missing total transverse energy of the events had to be below $E_t^{miss} = 5$ GeV to ensure that the transverse jet energies were well measured.

The shape of the ΔE_t distribution is described by a PYTHIA calculation with multiple parton interactions which includes hard initial state parton showers (full histogram in Fig.43a). The dashed histogram represents the prediction of the PHOJET generator which does not include hard initial state parton radiation effects: this calculation gives too small ΔE_t. Hard initial state parton radiation effects are essential to describe the data.

In Fig.43b the transverse momentum imbalance of the two scattered partons is shown for the PYTHIA calculation (full histogram). Their Δp_t distribution results primarily from initial state parton radiation effects: for comparison also the intrinsic transverse momentum k_t distributions of the partons from the proton (dotted histogram) and the photon (dash-dotted histogram) are shown.

Fig.44 shows a four-jet event observed with the H1 detector. This is another demonstration that higher order effects are present.

In summary:

- Higher order QCD effects are present in the measured photoproduction data.

Summary: Verification of QCD predictions in γp scattering

- Hard scattering processes in photon–proton collisions were unambiguously observed by particles with large transverse momenta and jets with high transverse energies.
- Jets from γp interactions are of the same nature as the jets found in $\overline{p}p$ and $\gamma\gamma$ scattering.
- The differential jet and particle transverse momentum cross sections at rapidities around $\eta = 0$ are described by QCD calculations.
- Direct and resolved photon–proton processes were both observed in events with at least two jets.
- The distributions of the parton scattering angle were found to be different for direct and resolved γ interactions. They are correctly predicted by QCD.
- The presence of higher order processes was demonstrated in di-jet events by the imbalance of the transverse jet energies and by the observation of multi-jet events.
- Jet formation from the photon spectator partons was observed. The transverse jet energy distribution reflects the transverse momenta of the partons from the photon which were found to be large, as expected from the anomalous photon component.

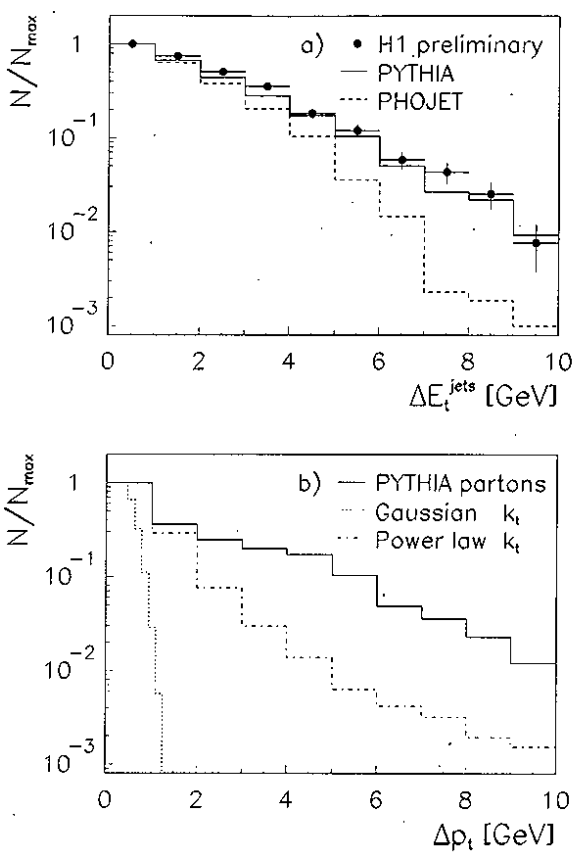

Figure 43: a) The shape of the uncorrected jet transverse energy imbalance $\Delta E_t = E_t^{jet1} - E_t^{jet2}$ is shown from H1 di-jet data (full symbols [RIC-96]). The jets had transverse energies above $E_t^{jet} = 7$ GeV. The reconstructed fractional parton energy was $x_\gamma^{jets} > 0.4$ in order to reduce effects of multiple parton interactions. The full and dashed histograms show the predictions of the PYTHIA and PHOJET generators including a detailed simulation of the detector effects. The PYTHIA calculation provided hard initial state parton radiation effects. the PHOJET calculation did not.
b) The full histogram reflects the transverse momentum imbalance of the scattered partons of the PYTHIA calculation. This imbalance results primarily from parton radiation effects: the dotted histogram indicates the shape of a Gaussian transverse momentum k_t^p distribution of the partons from the proton. The dash-dotted histogram reflects the shape of the power law k_t^γ distribution of the partons from the photon.

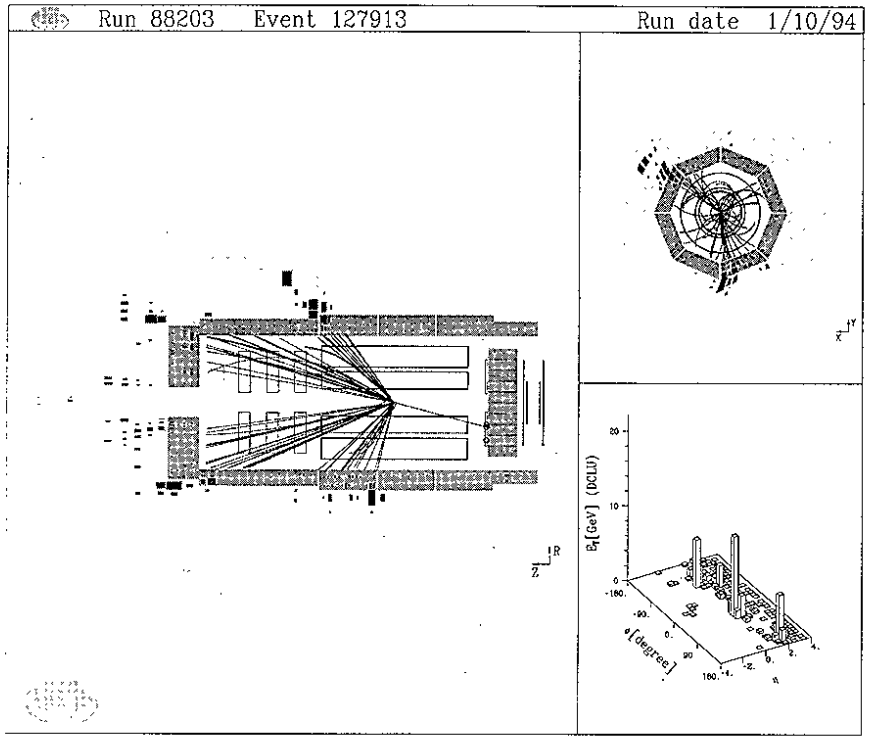

Figure 44: Photoproduction of four jets: the side view of the H1 detector is shown on the left side. where the proton comes from the right, the electron from the left. Some particles of the proton spectator are shown close to the beam pipe on the left side of the detector. The electron scattered through a small angle and was detected in the electron detector of the luminosity system. The upper right picture shows the plane transverse to the beam axis. The histogram shows the transverse energy weighted jet positions in the pseudo-rapidity and azimuthal directions (lower right).

6 Multiple parton interactions

Jets reflect the kinematic properties of the hard scattered partons. To go from jet properties to parton properties one has however take into account the following effects:

1. Transverse energy from the scattered partons may fall outside of the jets. The reason can be final state parton radiation, or fragmentation effects. Transverse energy of initial state parton radiation may fall into the jet.

2. Interactions between the spectator partons of the two beam particles may contribute to the energy inside the jets, since their energy contributions should be uncorrelated with the primary parton scattering process.

3. Fragments of the non-interacting spectator partons may contribute energy inside the jets. This contribution is also uncorrelated with the parton scattering process.

Whereas items 1) and 3) are provided in standard QCD generators, the existence and importance of item 2) has to be demonstrated.

In this section we will discuss the results on double parton scattering (item 2) obtained at pp and $\overline{p}p$ colliders, using four jet events. Then we will study the transverse energy distributions in γp collisions with respect to multiple parton scattering (item 1,2) and quantify the smearing of the jet energy.

6.1 Double parton scattering in pp and $\overline{p}p$ collisions

The distortion effects, listed above, have been discussed in the analysis of $\overline{p}p$ collisions for several years. The extreme case of spectator interactions (item 2) are hard parton interactions which result in four-jet events. Here we will briefly discuss these results:

The cross section σ_{dp} for such double parton scattering can be calculated from the di-jet cross section σ_{di-jet} times the probability to have a second di-jet production in the same event:

$$\sigma_{dp} = \sigma_{\mathrm{di-jet}} \frac{\sigma_{di-jet}}{2\ \sigma_{eff}} \tag{49}$$

Here σ_{eff} is the part of the total cross section which is relevant to di-jet production. The factor 2 has been suggested in [SJO-87B]. For uncorrelated double di-jet production, σ_{eff} is proportional to the total non-diffractive cross section $\sigma_{eff} = \sigma_{non-diff.}/2$.

The rate of double parton scattering is highly suppressed with respect to the double bremsstrahlung effects which give four parton final states from higher order QCD processes. Therefore observables were designed which are sensitive to the differences between double parton interactions and double bremsstrahlung effects. Such observables study the jet configurations in the azimuthal direction: in the case of double parton scattering, the transverse momenta of each di-jet pair are well balanced, and the azimuthal production angle $\Delta\Phi$ of the two di-jet pairs is uncorrelated, i.e. the distribution of $\Delta\Phi$ is flat. In contrast to this, the double bremsstrahlung processes give a $\Delta\Phi$ distribution which is peaked at $\Delta\Phi = \pi$.

The AFS collaboration reported evidence for double parton interactions in four-jet events with $E_t^{jet} \geq 4$ GeV at the CM energy $\sqrt{s_{pp}} = 63$ GeV [AFS-87]. This result was not confirmed by a study of the UA2 collaboration, which used four jets with $E_t^{jet} > 15$ GeV in $\overline{p}p$ collisions at $\sqrt{s_{\overline{p}p}} = 630$ GeV [UA2-91]. They set a limit on the normalizing cross section $\sigma_{eff} > 8.3$ mb at 95% confidence level.

More recently, evidence for double parton scattering was reported by the CDF collaboration using jet energies above $E_t^{jet} = 25$ GeV at the CM energy $\sqrt{s_{\overline{p}p}} = 1800$ GeV [CDF-93]. They determined the double parton cross section $\sigma_{dp} = 63 \pm^{32}_{28}$ nb for parton transverse momenta $p_t > 18$ GeV, and an effective cross section $\sigma_{eff} = 12.1 \pm^{10.7}_{5.4}$ mb. This result is compatible with uncorrelated double parton scattering, because the non-diffractive cross section amounts to $\sigma_{non-diff.} \approx 44$ mb. It is also compatible with the limit set by the UA2 experiment.

These measurements indicate that several parton–parton collisions can happen in one event. However, the four jet analyses are complicated, because one searches for a small effect within large hadronic activity. Therefore, the results need support from other measurements. If multiple parton interactions are universal, then they should also be found in other processes than $\overline{p}p$ interactions, e.g. in resolved γp collisions at HERA.

6.2 Transverse energy distributions in γp collisions

At HERA, the effects of multiple parton interactions were studied using transverse energy flow distributions. It is interesting that, in the case of γp collisions, spectator partons of the photon (item 3 of the introduction to section 6) – and therefore spectator parton interactions (item 2) – exist only for resolved photon interactions, but not for the direct photon processes. Therefore, comparisons of direct and resolved photoproduction events have a good potential to give new information on interactions between spectator partons.

Since we are looking for details in events, which include parton scattering processes, we need the comparison of the data with generators where spectator interactions can be turned on and off. In this section we therefore study events with sufficiently large transverse energy with respect to the following questions:

1. How much transverse energy is produced in the events?

2. How is the transverse energy distributed along the γp collision axis?

3. How strongly correlated are the energy depositions?

4. How much transverse energy flow appears next to jets?

6.2.1 Inclusive transverse energy cross section

In this section we study the transverse energy of the final state hadrons, independently of jet production. The H1 analysis, described here, was based on a 1993 sample of quasi-real photon-proton collisions ($Q^2 \leq 0.01$ GeV^2) at average CM energies $\sqrt{s_{\gamma p}} = 200$ GeV [H1-96A].

The data correspond to an integrated luminosity of 0.29 pb^{-1}. In Fig.45a the differential transverse energy cross section is shown for transverse energies between $20 \leq E_t \leq 50$ GeV. The energy was summed in the rapidity region $-2.5 \leq \eta_{\gamma p} \leq 1$ and was corrected for detector effects. The errors are dominated by the uncertainty in the knowledge of the absolute H1 calorimeter energy scale. The cross section is around 10 nb/GeV at $E_t = 20$ GeV and shows an exponentially decreasing distribution $\exp(-\lambda E_t)$ with $\lambda = 0.21 \pm 0.01$. Such exponential transverse energy distributions have been observed in pp and $\bar{p}p$ collisions at sufficiently high energy before [AFS-83, UA1-87, CDF-92].

The data in Fig.45a could equally well be fitted by a power law E_t^{-n} which one would naively expect from parton scattering processes. A fit to the data gave $n = 5.9 \pm 0.1$ which is close to the power law found in the inclusive jet cross sections (Fig.36) and supports the interpretation of this distribution in terms of hard parton scattering processes.

Also shown in the same figure are calculations of different QCD generators, using the same parameterizations of the parton distributions in the photon and the proton throughout (GRV-LO [GLU-92C, GLU-95A]). The PYTHIA single parton interaction model is far below the data, and shows a power law behaviour, rather than an exponential distribution (dotted histogram). The PYTHIA calculation with multiple parton interactions shows instead an exponentially decreasing distribution with a different slope compared to the data (dashed histogram). In this model relatively small energy depositions of spectator interactions are added on top of the energy from the hard parton scattering process. They not only give a higher cross section, since more events get over the E_t threshold, but also cause a significant change in the shape of the distribution. The PHOJET predictions (full histogram), which include multiple parton scattering, were found to be well compatible with the data in the measured E_t range. The main difference between the PYTHIA and PHOJET models is, that PYTHIA includes only QCD hard multiple parton interactions, while PHOJET contains soft and hard multiple parton scattering processes.

6.2.2 Transverse energy flow

Fig.45b shows the average transverse energy per event as a function of the γp CM rapidity. For this measurement, the total transverse energy was restricted to the interval $25 \leq E_t \leq 30$ GeV (Fig.45a). The data were corrected for detector effects, where the corrections depend slightly on the generator model used and give the dominant measurement error in this energy distribution. The energy flow per event in minimum bias data (open circles) is also shown in the figure. This data set is defined by a trigger condition which accepts 95% of the total non-diffractive photoproduction cross section (Fig.13). While the minimum bias data are perfectly flat in this rapidity interval, as one would expect from soft hadronic interactions, the high energy data differ from such a flat distribution and show a maximum close to the mid-rapidity region. These phenomena are well known from hadron-hadron collisions: a) flat rapidity distributions have been extensively studied at the ISR [BS-75, CAP-74], while b) at the large beam energies of $\bar{p}p$ collider experiments the rapidity distributions with sufficiently high transverse energy are peaked at mid-rapidity [UA1-87].

The observation that the transverse energy distribution of the γp data is not flat means that these data cannot result from soft γp interaction, but show the scattering of constituents which

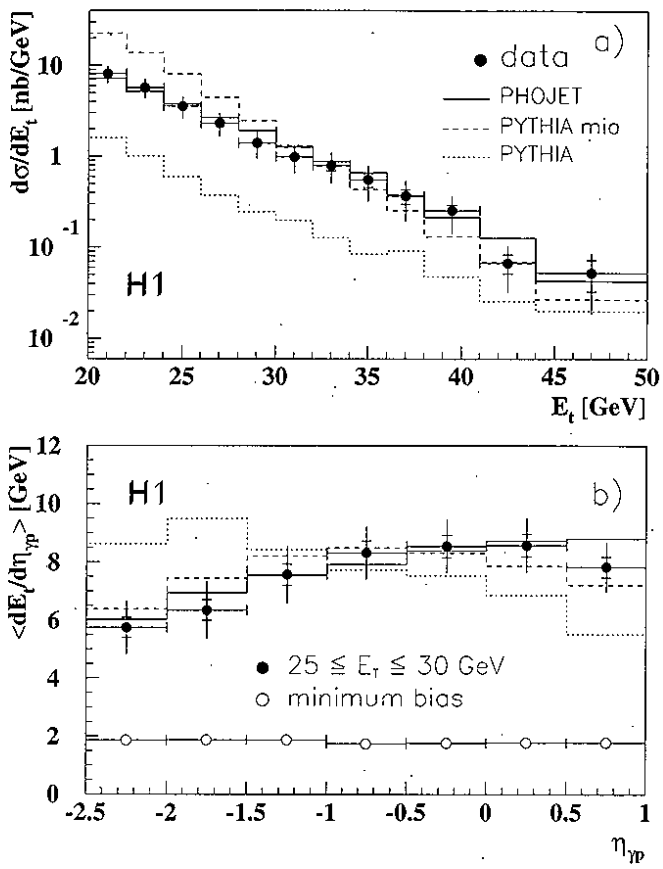

Figure 45: a) The inclusive differential transverse energy cross section $d\sigma/dE_t$ is shown for the γp center of mass rapidity interval $-2.5 \leq \eta_{\gamma p} \leq 1$ from H1 data [H1-96A]. The dotted and dashed histograms show the LO QCD calculation of the PYTHIA generator for single hard parton scattering processes and for multiple interactions respectively. The full histogram is a calculation of the PHOJET generator which also includes multiple interactions.
b) The transverse energy is shown as a function of $\eta_{\gamma p}$ for the total transverse energies between $25 \leq E_t \leq 30$ GeV (full points). The measurement is compared to the energy level found in non-diffractive soft scattering processes (minimum bias data: open circles). Histogram assignment is as in a).

have less than the full beam energy. Naively, one would expect this distribution to be peaked somewhere in the photon fragmentation region, i.e. at negative rapidities, since more partons with large fractional energy x exist in the photon than in the proton. In the same Fig.45b the PYTHIA calculation for one hard parton interaction per event is shown which supports this simple view (dotted histogram). Possible explanations for the maximum at mid-rapidity are:

(a) The distribution is dominated by the scattering of partons with small momentum fractions x and the parton distributions of the photon and proton are similar. This would require a large gluon content in the photon.

(b) The effect could be explained without requiring a large gluon content in the photon by the superposition of several parton scattering processes with a fraction of processes at small x to fill energy into the γp CMS region.

The latter scenario is implemented in PYTHIA with hard multiple parton interactions which is shown in the figure as the dashed histogram. The maximum is shifted relative to the calculation of the single parton interaction model towards the central rapidity region of the γp collision, but the calculation still does not coincide with the data. The PHOJET calculation gives a fair description of these data distributions.

In summary:

- The description of the measured transverse energy distributions is much improved by the inclusion of multiple parton interactions.

6.2.3 Energy-energy correlations

In previous figures (e.g. Fig.34,45), QCD generators which allow for multiple parton interactions describe the data significantly better than generators with one parton scattering process per event. In multiple parton interaction models the parton-parton scattering processes are essentially independent of each other. Here we want to test this model assumption by studying the transverse energy-energy correlations.

Fig.46 shows the transverse energy-energy correlations in H1 data (event selection was described in section 6.2.1) in the rapidity projection with respect to the central collision region of the γp CMS, where most of the energy is concentrated. The H1 detector is well suited for this measurement, since the calorimeter has a fine granulation in the region of interest. The correlation function Ω was defined as

$$\Omega(\eta_{\gamma p}) = \frac{1}{N_{ev}} \sum_{i=1}^{N_{ev}} \frac{\left(\langle E_{t,\eta_{\gamma p}=0}\rangle - E_{t,\eta_{\gamma p}=0}\right)_i \left(\langle E_{t,\eta_{\gamma p}}\rangle - E_{t,\eta_{\gamma p}}\right)_i}{(E_t^2)_i} \qquad (50)$$

The average energies $\langle E_{t,\eta_{\gamma p}}\rangle$ were determined from all events. The data shown were not corrected for detector effects and have a total transverse energy in the rapidity region shown of $E_t^{vis} \geq 20$ GeV. Short range energy correlations are observed close to the mid-rapidity region. According to the definition of the correlation function this means: if the energy deposited at

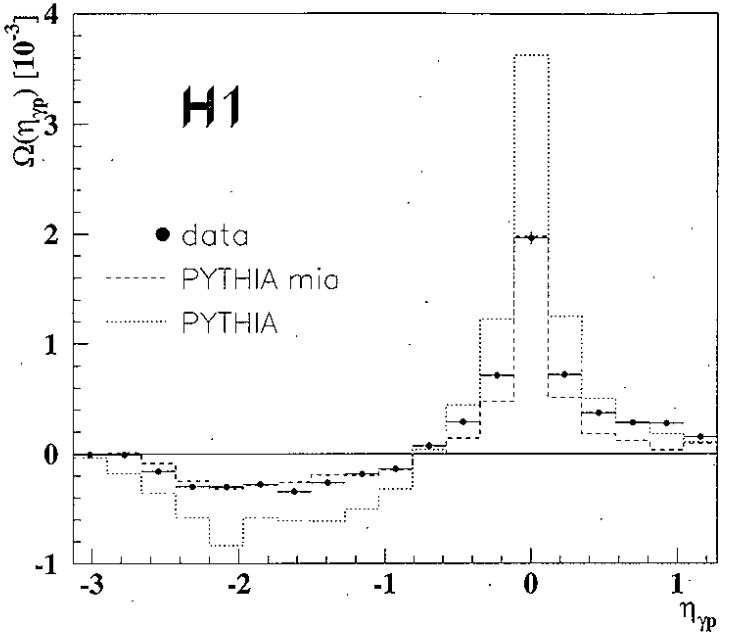

Figure 46: Observed transverse energy correlations with respect to the γp center of mass are shown as a function of the rapidity $\eta_{\gamma p}$ from H1 data [H1-96A]. The dotted histogram shows the LO QCD calculation of the generator PYTHIA for single hard parton scattering processes which gives too strong energy correlations. The dashed histogram represents the calculation of the same generator including multiple interactions, which shows a correlation strength similar to that observed in the data.

$\eta_{\gamma p} = 0$ in one event is above the event average energy, the energy in the neighbour bin is also above the event average in that bin. Anti-correlations are observed in the photon hemisphere at rapidity $\eta_{\gamma p} \sim -1.8$.

The PYTHIA calculation of single hard parton interactions including a detailed simulation of the H1 detector, shows the same shape of the correlation function (dotted histogram). However, the correlation strength between the transverse energy depositions is twice as large as in the data. In contrast, the same calculation of PYTHIA with multiple interactions (dashed histogram) not only gives a fair description of the shape of the rapidity correlation, but also results in the correct

energy correlation strength, as observed in the data. These conclusions do not change with the added requirement of two jets with transverse energy above $E_t^{jet} > 7$ GeV in the event.

In summary:

- The studies of energy-energy correlations give strong support to multiple parton interaction models which spread *uncorrelated* energy into an event, in addition to the energy resulting from a hard scattering process.

6.2.4 Underlying event energy

If the large measured transverse energy flow results from additional interactions between the spectator partons of the proton and the photon, we expect differences in the energy flow between resolved and direct photoproduction processes: only the resolved photon processes can have spectator interactions, not direct photon processes, which by definition do not have photon spectator partons. More generally speaking, we expect a dependence on the energy fraction x_γ of the parton from the photon, which determines the energy $E_{\gamma sp}$ remaining for the photon spectator partons: $E_{\gamma sp} = (1 - x_\gamma)E_\gamma$. The parton fractional energy from the proton side is typically $x_p \approx 0.01$, so the energy of the proton spectator partons is essentially the same as the proton energy.

The transverse energy density at mid-rapidity

In this H1 analysis x_γ was reconstructed using the two jets with the highest transverse energy E_t^{jet} in the event and their rapidities in the laboratory frame η^{jet} (eq.(47)) [H1-96A]. The photon energy E_γ was determined from the energy of the scattered electron in the luminosity detector (eq.(34)).

Since we are looking for effects beyond the primary hard parton scattering processes, we need to exclude the transverse energy of the jets themselves. The energy flow, measured outside of jets, is called the *underlying event energy*. From Fig.45b,46 we know that the effects of spectator parton interactions should be largest at mid-rapidity, where the energy flow is largest, and the correlations of the transverse energy depositions are relatively weak.

In Fig.47 the corrected average underlying transverse energy density at mid-rapidity of the γp CMS is shown for events with at least two jets (points). In addition to the event selection, described in section 6.2.1, two jets were required with transverse energies $E_t^{jet} > 7$ GeV, collected in a cone of size R=1. The energy was summed in the region $|\eta_{\gamma p}| \leq 1$. Energy deposited close to the jet axes, within $R \leq 1.3$ of the two jets with the highest transverse energies, was excluded from the energy sum. The summed energy was divided by the area used for the energy summation. Therefore, the vertical axis of Fig.47 represents the energy outside of jets per unit area in (η, φ) space. The horizontal axis represents the parton momentum x_γ^{jets} according to eq.(47). x_γ^{jets} was corrected for detector effects. The error bars of the distribution are dominated by the uncertainty in the detector corrections.

The energy density of the underlying event in Fig.47 was measured to be 0.4 GeV/rad at large fractional energies x_γ^{jets} and to increase to above 1 GeV/rad at small x_γ^{jets}. The measurement

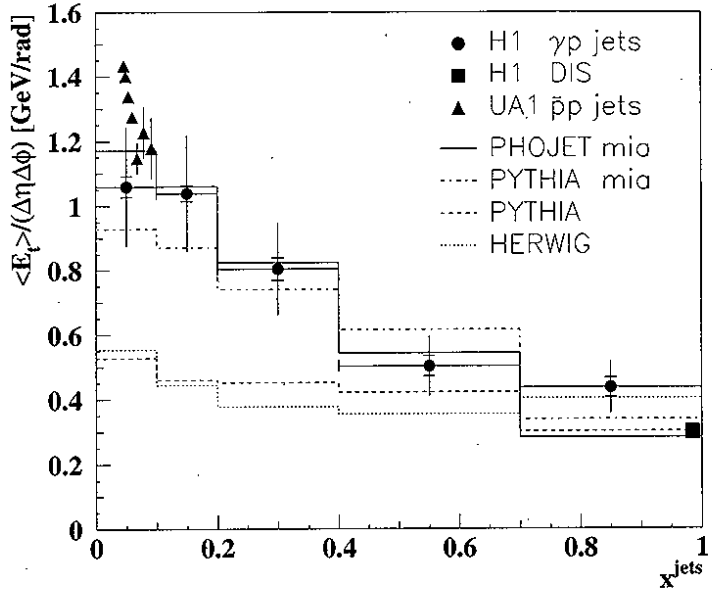

Figure 47: The transverse energy density outside of jets is shown for the central γp collision region $|\eta_{\gamma p}| \leq 1$ from H1 data (full circles) [H1-96A]. The E_t density was measured as a function of the fractional momentum of the parton from the photon side using equation (47). The histograms are LO QCD calculations of the HERWIG (dotted) and PYTHIA (dashed) generators for one hard parton scattering process per event. The dash-dotted and full histograms represent the calculations of the PYTHIA and PHOJET generators including multiple parton interactions.
The transverse energy density measured in deep inelastic ep scattering in the central $\gamma^* p$ collision region is shown as the square symbol for events with average photon virtuality $\langle Q^2 \rangle = 30$ GeV^2 from H1 data [H1-95D]. Since this measurement results from direct photon interactions, it has been placed at $x = 1$.
The triangle symbols represent the raw transverse energy density measured outside of jets in $\overline{p}p$ collisions at $\sqrt{s_{\overline{p}p}} = 630$ GeV, where the jets had transverse energies between $28 \leq E_t^{jet} \leq 62$ GeV (UA1 Collab. [UA1-88]). The parton energy fraction was here estimated using $x = E_t^{jet}/\sqrt{s_{\overline{p}p}}$.

is compared to the energy level found at mid-rapidity in deep inelastic scattering (DIS) events at average $\langle Q^2 \rangle = 30$ GeV^2 from H1 data (square), which correspond to 'pure' direct photon-proton interactions [H1-95D]. It is interesting to note, that the energy level of these DIS events coincides with that of minimum bias photoproduction data (Fig.45b). Since the only common contribution to the underlying event in these two data sets is the fragmentation process, the initial and final state parton radiation in direct photon events cannot have a large influence on the central photon-proton collision region.

The triangle symbols in Fig.47 show the uncorrected underlying event transverse energy measured in $\overline{p}p$ collisions at $\sqrt{s_{\overline{p}p}} = 630$ GeV next to jets with transverse energies between $28 \leq E_t^{jet} \leq 62$ GeV [UA1-88]. Such collisions involve initial state partons with small energies which we have calculated from $x^{jets} = E_t^{jet}/\sqrt{s_{\overline{p}p}}$. The energy density is found to be compatible with the energy measured in resolved photon-proton interactions at $x_\gamma^{jets} = 0.1$ and tends to increase towards small x^{jets}. This similarity hints for a universal effect.

The amount of initial state radiation at low x_γ^{jets} has been checked with two QCD generators for single parton scattering processes per event. The results of these calculations are shown in Fig.47 as the dashed (PYTHIA) and dotted (HERWIG) histograms. The calculations show a small increase of the energy density towards small x_γ^{jets}, however, the increase is far below the data. The use of another photon structure function parameterization cannot change this result, since, e.g., a large gluon content at small x_γ^{jets} increases the number of events, but not the average energy density. Attempts to reproduce the large energy density with increased initial state parton radiation effects did not result in a consistent description of the data.

Fig.47 also shows a calculation of the PYTHIA model with hard multiple parton interactions using the GRV-LO parton distribution functions (dash-dotted histogram). This gives a transverse energy density which is compatible with the data. Also the fluctuations of the energy density are described by this model as well as the jet kinematics at small x_γ [HUF-95]. The calculation of this model does depend on the choice of the photon structure function parameterization, because

1. subsequent parton scattering processes result from a different parton energy fraction x_γ, and

2. the number of parton scattering processes depends on the gluon density in the photon.

A PYTHIA calculation using the LAC1 parameterization of the photon structure function instead of the GRV-LO set results in an energy density which is too large at small x_γ^{jets} by 0.5 GeV/rad. A re-adjustment of the parton transverse momentum cut-off from $\hat{p}_t^{mia} = 1.2$ GeV to $\hat{p}_t^{mia} = 2$ GeV again results in a compatible description of the measured distribution [STE-96]. The calculation of the PHOJET generator which contains soft and hard multiple parton interactions, gives a fair description of the measured energy density shown as the full histogram in Fig.47 (using the GRV-LO parameterizations).

The number of interactions per event

Independently of the specific multiple interaction model, one can estimate the number of interactions per event between the beam particles via the underlying transverse energy density itself: the calculations of the transverse energy flow E_t^{sia} for single hard parton interactions per event represent the energy resulting from a primary hard scattering process (Fig.47: dashed, dotted histograms). Since distributions of transverse energy are steeply falling, we assume that the additional interactions between the beam remnants are not jet like to first order, but contribute transverse energy $E_t^{min.bias}$ at the level of minimum bias events (Fig.45b). With these assumptions the number of interactions per event can be determined from the measured transverse energy density E_t^{meas}:

$$R = 1 + \frac{\langle E_t^{meas} \rangle - \langle E_t^{sia} \rangle}{\langle E_t^{min.bias} \rangle} \tag{51}$$

In Fig.48 the interaction rate is shown as a function of the energy fraction x_γ. We have ignored here the logarithmic dependence of the transverse energy density $E_t^{min.bias}$ in minimum bias events on the CM energy which is available to the spectator system $\sqrt{s} = \sqrt{(1-x_\gamma)s_{\gamma p}}$, because this can only be calculated for the first spectator interaction, not for a subsequent one. Therefore, the rate R is a lower estimate of the interaction rate. The transverse energy density $\langle E_t^{sia} \rangle$ used was the average value of the PYTHIA and HERWIG calculations. The number of interactions per event above $x_\gamma > 0.4$ is compatible with one interaction. Below $x_\gamma < 0.4$ the rate increases to three interactions per event on average between the photon and the proton.

Summary: multiple parton interactions

- The measured transverse energy distributions in γp scattering are described much better overall by QCD generators with multiple parton interactions compared to generators without them.

- At large fractional parton energies $x_\gamma > 0.4$, QCD generators which calculate one hard parton scattering process per event give a consistent description of the measured transverse energy flow.

- At low $x_\gamma < 0.4$, such calculations fail to describe the large measured underlying event energy. Analytic NLO QCD calculations also cannot account for this large E_t flow [AUR-95, KRA-95]. A natural explanation is provided by models which allow for several parton–parton interactions per event. The photon, with its unique feature of direct and resolved photon interactions, gives new insight into multiple parton scattering dynamics, complementary and beyond the double parton scattering reported from $\overline{p}p$ scattering.

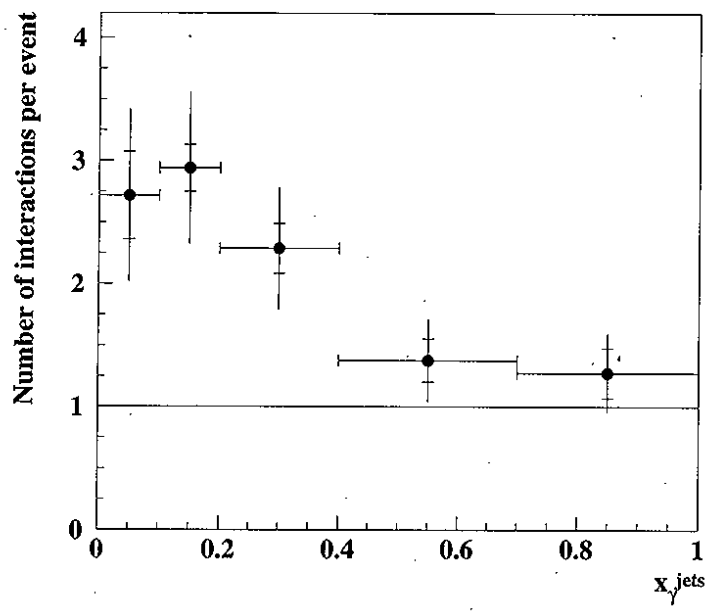

Figure 48: The number of interactions per event was calculated from the transverse energy density of the underlying event: $R = 1 + (\langle E_t^{meas} \rangle - \langle E_t^{sia} \rangle)/\langle E_t^{min.bias} \rangle$. Here $\langle E_t^{meas} \rangle$ are the measured values from Fig.47. The QCD calculation of the transverse energy density produced by a single hard parton interaction is represented by $\langle E_t^{sia} \rangle$ (Fig.47: dashed, dotted histograms). The transverse energy density $\langle E_t^{min.bias} \rangle$, determined in minimum bias photoproduction events, was used as a measure of the transverse energy produced in the interactions between the beam remnants.

7 Parton distributions of the photon

What is the contribution of particle and jet data in photon–proton and two-photon interactions to our knowledge of the parton distributions in the photon? Do such results go beyond the achievements of the DIS lepton-photon scattering experiments ?

The results of the DIS $e\gamma$ experiments constrain the quark distribution of the photon for parton fractional energies between $0.05 < x_\gamma < 0.9$ to the level of 30%. These data are not sensitive to the gluon distribution of the photon, as was demonstrated by the LAC1-3 parton distribution functions. Uncertainties in the very small, $x_\gamma \ll 0.1$, and very large, $x_\gamma \approx 1$, regions are large (see Figs.17,19).

Particle and jet measurements of photoproduction data at HERA and two-photon data at TRISTAN and LEP are sensitive to the quark and gluon content of the photon (Fig.9). They cover a large region of parton fractional energies up to $x_\gamma = 1$. At small x_γ they are constrained by a lower limit which can be estimated from

$$x_\gamma > \frac{p_t e^{-\eta}}{2E_\gamma} \tag{52}$$

where

1. Comparisons with perturbative QCD calculations require parton transverse momenta above $p_t \approx 2$ GeV,
2. The rapidity η measurement of a particle or jet is limited by the detector acceptance,
3. The photon energy E_γ is limited by the available beam energies.

Typically, the parton fractional energies are above $x_\gamma = 0.01$ at HERA, and $x_\gamma = 0.1$ at TRISTAN, and $x_\gamma = 0.05/0.01$ at LEP1/2.

7.1 Particle cross sections

How large are the contributions coming from the different photon components, – direct, vector meson (vdm), anomalous – to the measured particle cross sections ? Do comparisons of data and QCD calculations give constraints on the quark and gluon distributions of the photon?

In Fig.49 a preliminary H1 analysis [HOP-95] is shown of the differential charged particle cross section $d\sigma/dp_t$ in comparison with a LO QCD calculation. The measurement was based on the 1994 data taking period with an integrated luminosity of 1.3 pb^{-1}. The event kinematics covers photon virtualities $Q^2 < 0.01$ GeV^2, and the scaled photon energy interval $0.3 < y < 0.7$ at average photon–proton CM energies of $\sqrt{s_{\gamma p}} = 200$ GeV. The cross section is shown for particles with transverse momenta above $p_t = 2$ GeV, integrated over the rapidity range $|\eta| < 1$.

The QCD calculation was based on the event generator PYTHIA with multiple parton interactions, using the GRV-LO parameterizations of the parton distributions for the photon

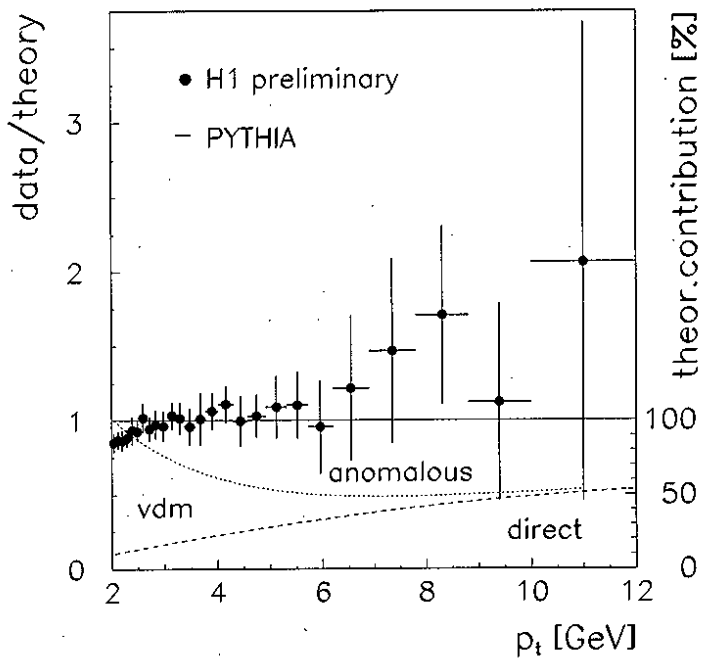

Figure 49: The ratio of the differential particle cross section $(d\sigma^{data}/dp_t)/(d\sigma^{theory}/dp_t)$ is shown from preliminary H1 data [HOP-95] and a LO QCD calculation. The theory part was calculated using PYTHIA with multiple interactions and the GRV-LO parton distributions of the photon and the proton. On the right axis, the relative contributions of the different photon components are indicated: the dashed curve is the calculation of the direct photon cross section. The dotted line indicates the sum of the direct and the vector meson (vdm) photon components which were normalized to the total calculation at $p_t = 2$ GeV. The vdm contribution was calculated using the GRV-LO parton distribution of the pion instead of the photon. The remaining cross section is assigned to the anomalous photon contribution.

and the proton. The data were normalized to the calculation of direct and resolved photon processes. The calculated cross section exceeds the data by 20% at transverse hadron momenta $p_t = 2$ GeV, and is compatible with the measurement above $p_t = 2.5$ GeV.

Also shown in figure 49 are the relative contributions of the direct, vdm and anomalous photon components. The vdm component was calculated using the parton distribution function

of a meson, instead of the photon. Here the GRV-LO parton distribution functions of the pion were used. At small scale $Q_o^2 = 0.25$ GeV^2, they have the same quark and gluon distribution as the photon, except for an overall normalization factor. The difference between the parton distributions of the pion and the photon at larger values of the scale results from the anomalous term in the inhomogeneous evolution equation (16) which is present only in the case of the photon. The vdm contribution was normalized, together with the direct photon component, to give the total calculated cross section at $p_t = 2$ GeV. The anomalous photon contribution then results from the difference between the total calculated cross section and the vdm plus direct photon components.

In this calculation the anomalous photon contribution amounts to 50% at transverse momenta $p_t > 6$ GeV. Above $p_t = 3.5$ GeV the photon components which are predicted by perturbative QCD (direct and anomalous) dominate the vdm contribution.

In Fig.50 the measured differential rapidity cross section $d\sigma/d\eta$ is shown for particles with transverse momenta above $p_t = 2$ GeV. The corresponding interval of the parton energy fraction can be estimated to be between $x_\gamma(\eta = 1) \approx 0.05$ and $x_\gamma(\eta = -1) \approx 0.4$ on average.

The data are compared to predictions of the PYTHIA generator with multiple interactions using two different parton distribution functions: GRV-LO (upper histogram) and LAC1 (lower histogram). The prediction using the GRV-LO parameterization gives a cross section which is too large at negative rapidities (large x_γ), and falls short at positive η (small x_γ). The calculation using LAC1 is compatible with the data at $\eta < 0$, but overshoots the measurement at $\eta > 0$.

The dotted histogram indicates the gluon contribution of the photon to the calculation: the steep rise of the gluon distribution, which is predicted by the LAC1 parameterization, is not supported by the data.

The particle spectra are insensitive to effects of multiple parton interactions at sufficiently large $p_t > 3$ GeV. Therefore, future comparisons of measured high p_t particle cross sections with NLO QCD calculations will give an important basis for the extraction of precise NLO quark and gluon distributions for the photon at small and large x_γ [BIN-96B]. Fragmentation functions of quark and gluons in NLO, which are needed for the calculations, are obtained from e^+e^- and $\bar{p}p$ data (see section 2.2).

In summary:

- The measured high p_t particle cross sections are sensitive to the quark and gluon distributions of the photon.

7.2 Jet cross sections

7.2.1 Inclusive differential jet cross sections

In this section comparisons of measured single inclusive jet cross sections from $\gamma\gamma$ and γp collisions with QCD calculations will be discussed with respect to the parton distributions of the photon.

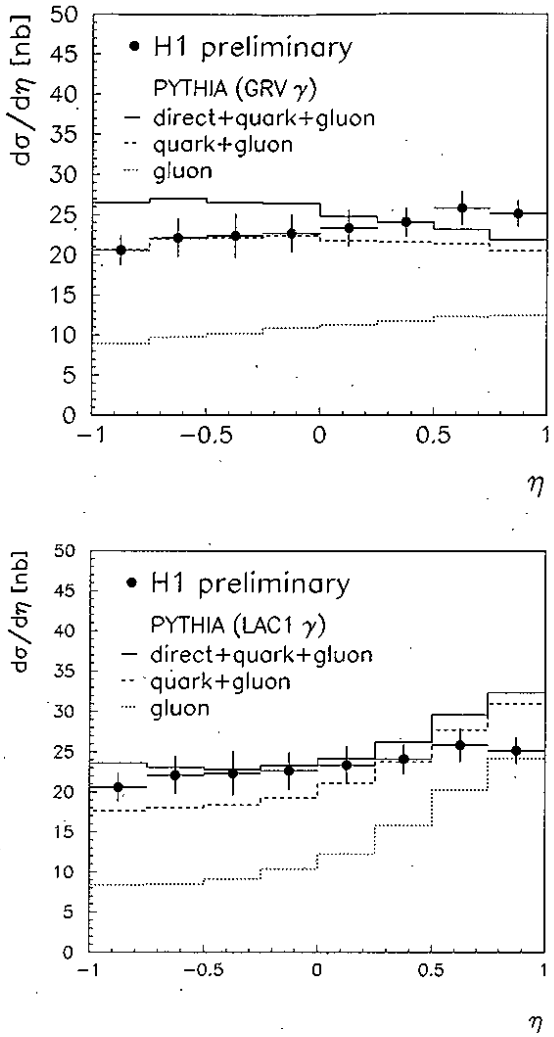

Figure 50: The differential particle cross section $d\sigma/d\eta$ is shown as a function of the particle rapidity η for transverse particle momenta above $p_t = 2$ GeV. The data are compared to predictions of the PYTHIA event generator with multiple interactions using two different photon distribution functions: in the upper (lower) histogram the GRV-LO (LAC1) parameterizations were used. The dotted curves represent the contribution of the gluon component of the photon. The dashed curves represent the calculations for the resolved photon contributions.

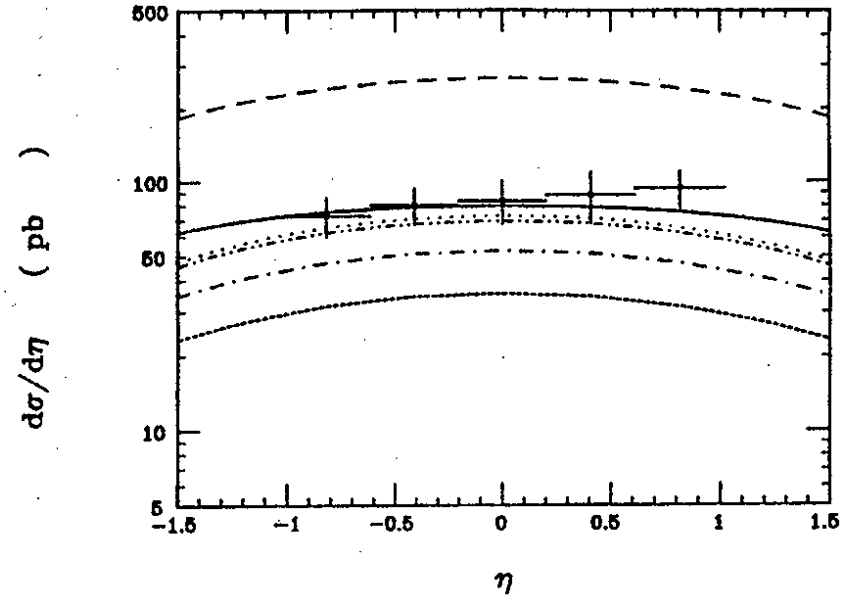

Figure 51: The measured inclusive differential parton rapidity cross section $d\sigma/d\eta$ is shown from the collision of two quasi-real photons for partons with transverse momenta $p_t \geq 2.5$ GeV (AMY Collab. [AMY-94]). The short dashed curve is the calculation of the Quark Parton Model. The other curves are LO QCD calculations using different parton distribution functions: long dashed=LAC3, full=LAC1, dash-dotted=LAC1 without gluons, dash-double-dotted=GRV, and dotted=DG).

Jet cross section in $\gamma\gamma$ scattering

In Fig.51 the differential parton rapidity cross section $d\sigma/d\eta$ from the collision of two quasi-real photons is shown from a jet analysis of the AMY experiment [AMY-94]. The data correspond to an integrated luminosity of 27.2 pb^{-1}. The virtuality of the photons was below $Q^2 = 10$ GeV^2, and the visible two-photon CM energy between $4 < \sqrt{s_{\gamma\gamma}} < 20$ GeV. The jets had transverse energies in the range $2.5 < E_t^{jet} < 9$ GeV, collected in a cone of size $R = 1$. The jet data were corrected for detector and fragmentation effects to the level of the scattered partons with transverse momenta $p_t > 2.5$ GeV. The measured cross section is around 80 pb at rapidity $\eta = 0$ and is consistent with being flat over the full measured rapidity range. $|\eta| < 1$.

In the same figure 51, LO QCD calculations are compared to the data, where different parameterizations of the parton distributions of the photon have been used. The corresponding fractional parton energy x_γ can be estimated from equation (47) to be around $x_\gamma \approx 0.2$ at the scale of $p_t^2 \approx 10$ GeV^2. In this kinematic range, the quark distribution of the photon has been measured by DIS $e\gamma$ scattering experiments. The direct photon contribution is predicted by QCD (see matrix elements: Tab.1). These two components together (dash-dotted curve)

amount to only 60% of the measured cross section, and show the need for a gluon contribution to the photon. Parameterizations of the parton distributions of the photon which rely on a gluon component similar to that of mesons result in QCD calculations which are compatible with the data (full=LAC1, dotted=DG, double-dot-dashed=GRV). A large gluon component of the photon at large parton energy fraction x_γ (dashed=LAC3) is excluded. This is compatible with the jet results of γp scattering [H1-93B]. The different photon contributions, direct photon (short-dashed), quarks (difference between dash-dotted and short-dashed), and gluons (difference between full and dash-dotted) all have similar shapes. Therefore this measurement is only sensitive to the total jet rate.

Jet cross section in γp scattering at high x_γ

How sensitive are the photoproduction jet data to the quark and gluon distributions of the photon ? In this paragraph, we concentrate on the region of large parton fractional energy $x_\gamma > 0.4$ where effects of the underlying event energy are small (Fig.47). This kinematic region corresponds to negative jet rapidities $\eta^{jet} < 0$.

In Fig.52 the differential jet ep cross section $d\sigma/d\eta$ is shown for photoproduction processes from ZEUS data. Here the rapidity projection of the data discussed in Fig.36 is shown for transverse jet energies $E_t^{jet} > 8$ GeV. The jets were corrected for detector effects, but not for fragmentation effects or underlying event energy effects.

The data are compared to an analytical NLO QCD calculation using the GRV-NLO parton distribution functions for the photon, and the MRSD$^-$ functions for the proton. Contrary to the two-photon calculations, the different photon contributions (short-dashed=direct γ, dotted=quark, dashed=gluon) have very different shapes. The region above $\eta^{jet} > 1$ cannot be compared directly, because the effects of the underlying event energy are large in the data, and are not included in the QCD calculations. This region will be discussed in the following paragraph. In the region $\eta^{jet} < 0$ the calculation overshoots the data by 30% at least, since the fragmentation effects tend to increase the cross section, and these effects are not included in the calculation.

In summary:

- The measured inclusive differential jet cross sections $d\sigma/d\eta^{jet}$ disfavour the NLO parameterizations of the quark distributions which extrapolate a steeply rising quark density at large x_γ (Fig.19). This region is poorly determined by DIS $e\gamma$ experiments and will be fixed by the γp data. Note that the LO parameterizations do not show the steep rise at large x_γ.

Jet cross section in γp scattering at small x_γ

Here we want to study the jet cross section at large rapidities η^{jet} which corresponds to small parton fractional energies x_γ. Two questions are of interest:

1. The QCD calculations of a single hard parton interaction per event fail to describe the underlying event energy (Fig.47). How large is the influence of the underlying event energy on the observed jet rate ?

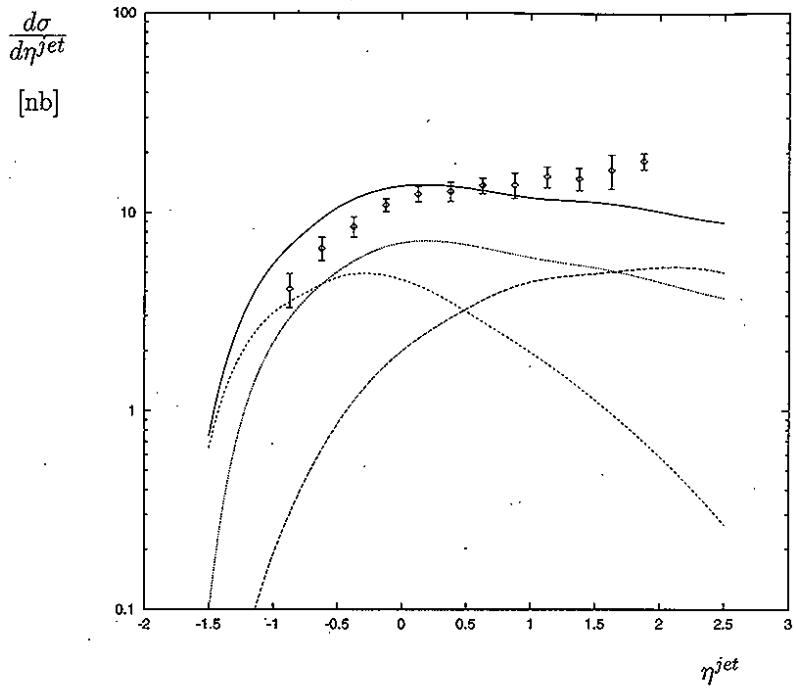

Figure 52: The inclusive differential ep jet rapidity jet cross section $d\sigma/d\eta^{jet}$ is shown for transverse jet energies above $E_t^{jet} > 8$ GeV from ZEUS data [ZEU-95A]. The measurements are compared to NLO QCD calculations. The full curve gives the complete calculation [KLA-95A]. The short-dashed curve is the contribution of the direct photon processes. The dotted (dashed) curves show the contribution of resolved photon processes with a quark (gluon) from the photon side.

2. Multiple parton interaction models describe the underlying event energy at small x_γ. How sensitive are comparisons between jet data and calculations with respect to the parton distributions of the photon ?

In Fig.53 the ratio of the measured differential jet cross section (H1 data, [H1-96A]) and the PYTHIA calculation with one hard parton scattering process per event is shown as a function of the jet rapidity: $(d\sigma^{(\mathrm{DATA})}/d\eta^{jet})/(d\sigma^{(\mathrm{PYTHIA})}/d\eta^{jet})$. The jets had transverse energies above $E_t^{jet} = 11$ GeV, summed in a cone of size $R = 1$. The event kinematics was determined by the tagged electron, where the virtuality of the photon was below $Q^2 < 0.01$ GeV^2 and the photon–proton CM energy was between $150 < \sqrt{s_{\gamma p}} < 250$ GeV. For the PYTHIA calculation

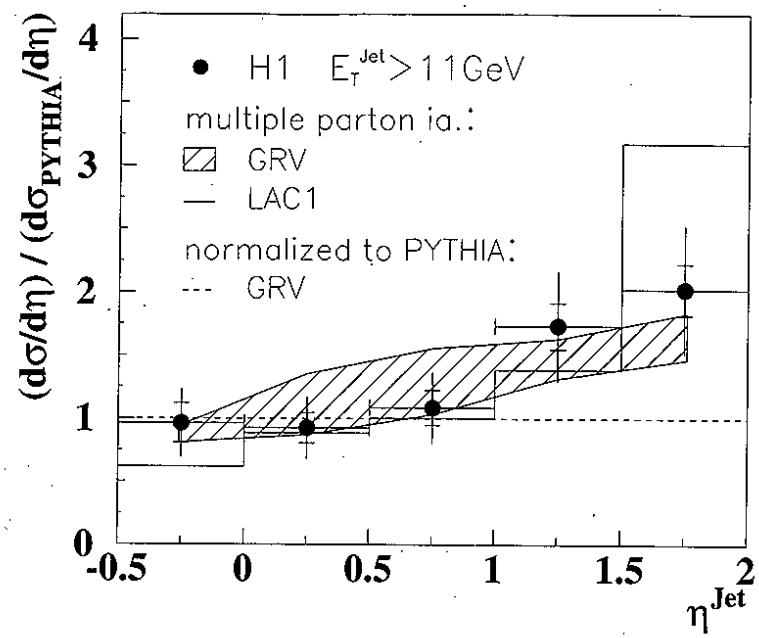

Figure 53: The ratio of the measured jet cross section and a calculation of the PYTHIA generator is shown as a function of the jet rapidity (full circles: H1 data [H1-96A]). The jets had transverse energies above $E_t^{jet} = 11$ GeV. The PYTHIA version without multiple interactions was used together with the GRV-LO parton distribution functions.
The hatched band shows the predictions of the PHOJET (lower edge) and PYTHIA (upper edge) generators, both including multiple parton interactions and both using the GRV-LO parton distribution functions. The histogram is the prediction of PYTHIA with multiple interactions using the LAC1 parton distribution functions.

the GRV-LO parton distribution functions for the photon and the proton were used. The average parton transverse momentum scale corresponded to $\langle \hat{p}_t{}^2 \rangle \approx 60$ GeV^2 which is well above the cut-off which was used here: $\hat{p}_t{}^2 = 4$ GeV^2.

The ratio of the data and the calculation in Fig.53 is compatible with one for jet rapidities below $\eta^{jet} = 1$. Here the underlying event energy and the rate of the measured jets are described by the calculation. At $\eta^{jet} > 1$ the measured jet cross section is about a factor of two above the calculation of the PYTHIA generator.

The effect of the underlying event energy on the jet rate is studied using two generators which include multiple parton interactions (PHOJET, PYTHIA). These calculations were normalized

to the same PTYHIA calculation as used for the data. The jet rate is increased by a factor 1.7 at large rapidities $1.5 \leq \eta^{jet} \leq 2$ due to the underlying event energy. Note that these calculations describe the measured underlying event energy (Fig.47: full, dash-dotted histograms) *and* the observed jet rate (Fig.53: hatched band).

Since the underlying event energy is described by these calculations, the rate of hard parton scattering processes can be studied to give information on the parton density in the photon. We are interested in studying the small x_γ region, therefore the LAC1 parton distributions of the photon were also used in the calculations. These have a much larger gluon density compared to the GRV-LO parameterization (Fig.19). The parton transverse momentum cut-off in PYTHIA was raised from $\hat{p}_t{}^{mia} = 1.2$ GeV (GRV-LO) to $\hat{p}_t{}^{mia} = 2$ GeV (LAC1) in order to describe the measured underlying event energy. The PYTHIA calculation using LAC1 is shown in Fig.53 as the histogram. It results in a rise of the jet rate at large jet rapidities which is much too steep compared to the measured jet rate [BUN-95].

In summary:

- The effect of the underlying event energy on the jet cross section is large: 40% at $E_t^{jet} = 11$ GeV and $\eta^{jet} = 2$. It has to be taken into account for meaningful conclusions on the low-x_γ parton distributions of the photon from jet data.
- Comparisons of the jet data with calculations, which describe the underlying event energy, show that the jet data are sensitive to the parton density of the photon at small x_γ. The calculations which use a moderately rising parton distribution function (GRV-LO) are compatible with the measured jet rate. A steeply rising parton density at low-x_γ (LAC1) is disfavoured.

7.2.2 Measurement of the gluon distribution

Instead of adjusting the jet underlying event energy in the QCD calculations to the level observed in the data, the data can be corrected. This procedure has the advantage that the parton distributions of the photon can be directly obtained from the data.

In Fig.46 it was shown that the observed large transverse energy is at most weakly correlated with the jets coming from the primary parton scattering process. Therefore the jet rate, which results from the large underlying event energy, can be subtracted on a statistical basis. In the following H1 analysis [H1-95B], the jet energies were corrected with respect to the underlying event energy E_t^{sia} which is expected from a single hard parton interaction per event. The jet energy correction E_t^{diff} was determined by a comparison of the transverse energy next to the jets in data, E_t^{data}, and the QCD calculation of the PYTHIA generator. It was parameterized as a function of the jet rapidity η^{jet}: $E_t^{diff}(\eta^{jet}) = E_t^{data}(\eta^{jet}) - E_t^{sia}(\eta^{jet})$, and amounted to $0.3 - 2.3$ GeV. The corrected jet energy $E_t'^{jet} = E_t^{jet} - E_t^{diff}$ was required to be above the jet energy threshold $E_t'^{jet} \geq 7$ GeV.

The di-jet event selection was based on an integrated luminosity of 0.29 pb^{-1} of the 1993 data taking period, requiring the electron to be detected in the small angle electron detector.

The kinematics correspond to quasi-real photon-proton scattering with $Q^2 \leq 0.01$ GeV^2 and $150 \leq \sqrt{s_{\gamma p}} \leq 250$ GeV. Both jets had rapidities between $0 \leq \eta^{jet} \leq 2.5$, and a rapidity distance between the two jets of $|\Delta\eta| \leq 1.2$ in order to prevent the photon remnant from being misinterpreted as one of the hard jets.

The data were corrected to the parton energy fraction x_γ of the LO parton level (eq.(37)). The parton momentum was first estimated from the two jets with the highest transverse energy in the event using formula (47) and then corrected by an unfolding procedure [BLO-84]. The procedure requires a correlation between the parton x_γ and the reconstructed x_γ^{jets} as input. This was calculated using the QCD generator PYTHIA with multiple interactions. The energies of the calculated jets were corrected for the additional underlying event energy resulting from the multiple parton interactions. The unfolding procedure modifies the input parton x_γ distribution of the QCD calculation so as to produce agreement between the predicted jet distribution and that seen in the data. The procedure is independent of the input parton distribution, and is controlled by the comparison of other jet observables between the data and the modified calculation [H1-95B].

In Fig.54 the two-jet distribution is shown as a function of the momentum fraction x_γ of the parton from the photon. The distribution shows two peaks which can be interpreted by a comparison with a LO QCD calculation, separating the three different photon components direct γ, quark and gluon contributions:

(a) The *resolved* photon-proton interactions with a *quark* on the photon side at the parton scattering process are shown as the full histogram in Fig.54. The matrix elements of the parton scattering are predicted by QCD, whereas the parton densities of the photon and the proton have to be taken from deep inelastic $e\gamma$, respectively ep experiments. Here the GRV-LO parameterizations were used [GLU-92C, GLU-95A]). Around $x_\gamma \sim 0.5$ this component alone is compatible with the jet data observed in the photoproduction events. Essentially, in this kinematic range, the photon splits into a quark and an anti-quark, each carrying half of the photon energy.

(b) The *direct* photon-proton cross section is predicted by QCD theory, except for the parton distributions in the proton. The dashed histogram above $x_\gamma \geq 0.77$ represents a LO QCD calculation using the GRV-LO parton distribution functions for the proton. When added to the resolved γ processes with a quark from the photon side, the result agrees with the data.

(c) Below $x_\gamma \leq 0.2$ the observed two-jet rate cannot be explained by the quark contributions of the photon, as measured by the deep inelastic $e\gamma$ experiments (Fig.17). This observed large jet rate above the quark contribution exhibits a significant *gluon* component of the *resolved* photon. Comparison with a calculated two-jet distribution including gluons in the photon gave the measured gluon momentum distribution in the photon shown in Fig.55.

The error bars on the gluon distribution measurement in Fig.55 result from uncertainty in the knowledge of the absolute calorimeter energy scale, from the uncertainty in the determination

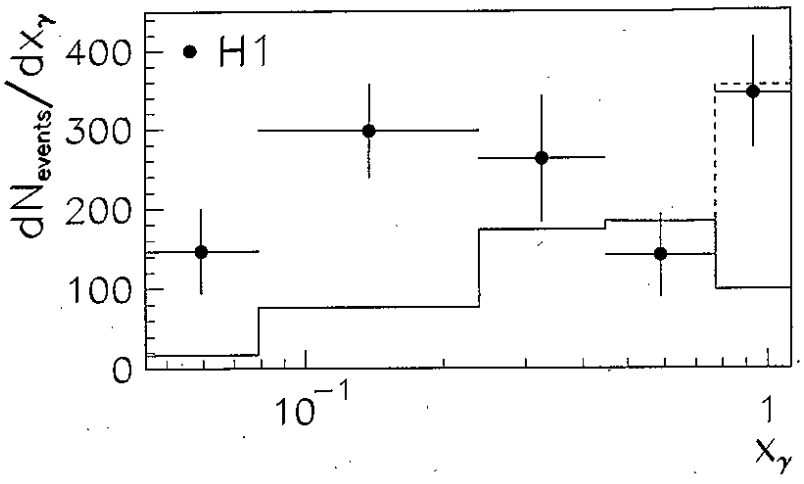

Figure 54: Distribution of the LO momentum fraction x_γ of the parton from the photon side from H1 data [H1-95B]. The full histogram is a LO QCD calculation of the PYTHIA generator using only the quark distribution function of the photon (GRV-LO parameterization). The dashed histogram shows the direct photon contribution. At small parton momenta, the difference between the data and the calculations shows a significant gluon contribution of the photon.

of the underlying event energy for the jet energy correction, and from the uncertainty in the quark distribution of the photon.

Three LO parameterizations of the gluon distribution of the photon are shown in the same figure (LAC1 = dashed, LAC3 = dotted, GRV-LO = full). In spite of the sizable error bars, the measured gluon distribution is neither very large at high x_γ (LAC3), nor steeply rising towards small values of x_γ (LAC1), but shows a shape and size which is, within error bars, reproduced by the GRV-LO parameterization which is based on the gluon distribution of π mesons.

In summary:

- For the first time, the LO gluon distribution of the photon was determined down to low parton momenta $x_\gamma \geq 0.04$ at the large average scale of $\langle p_t^2 \rangle = 75$ GeV^2.

Summary: parton distributions of the photon

- The two-photon and photoproduction jet data exclude a large gluon component in the photon at large fractional parton energies $x_\gamma > 0.1$ (LAC3 parameterization).

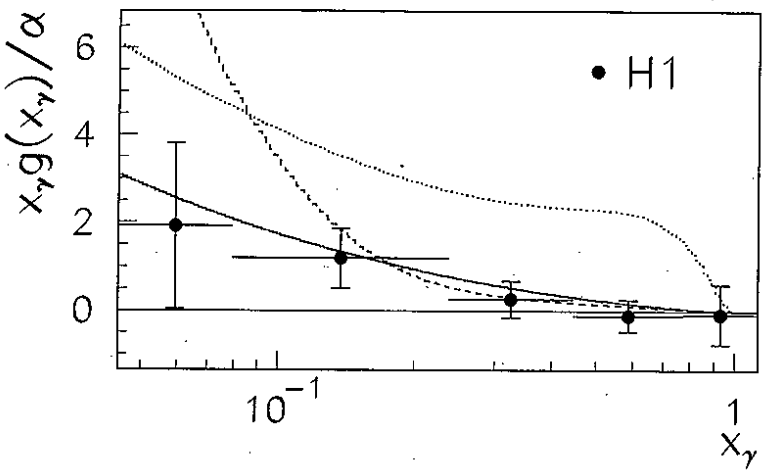

Figure 55: The measured LO momentum distribution of the gluon in the photon $x_\gamma g(x_\gamma)$ divided by α is shown from H1 data [H1-95B]. The average scale is $\langle p_t^2 \rangle = 75$ GeV^2. The curves represent parameterizations of the gluon distribution using the results of deep inelastic $e\gamma$ scattering experiments (full=GRV, dashed=LAC1, dotted=LAC3).

- The HERA γp jet data explore the parton distributions of the photon in the region around $x_\gamma \approx 1$: the comparisons of the inclusive jet cross sections with NLO QCD calculations show that the quark distribution of the photon does not rise steeply as $x_\gamma \to 1$ (e.g. GRV-NLO, AFG parameterizations).

- For the first time, the LO gluon distribution of the photon has been extracted from di-jet data for parton fractional energies $x_\gamma \geq 0.04$. The gluon component is not large at high x_γ. It also does not rise steeply towards low-x_γ (e.g. LAC1 parameterization), but shows a moderate rise (e.g. GRV-LO). Studies of the inclusive jet and particle cross sections confirm this measurement.

- Comparisons of measured jet cross sections with NLO QCD calculations at small $x_\gamma < 0.4$ are difficult, because the large observed underlying event energy is not included in the calculations, but has a large influence on the results. Comparisons of particle cross section measurements with NLO QCD calculations will provide a consistent way of extracting NLO quark and gluon distributions of the photon at small x_γ: these distributions are insensitive to the underlying event energy effects at sufficiently high hadron transverse momenta $p_t > 3$ GeV.

Part V

Status and future

Summary: hard photoproduction at HERA

The HERA machine together with the experiments H1 and ZEUS has turned out to be an important facility for the understanding of the photon. The experiments have already provided new information on the quasi-real photon, complementary and beyond the results obtained in photon-nucleon and two-photon experiments. All photoproduction measurements at HERA with large transverse energy E_t in the hadronic final state are compatible with the QCD picture of partonic scattering processes between the photon and the proton.

The presence of hard scattering in photoproduction processes at HERA was established by the following observations:

- Particles with large transverse momentum p_t: the inclusive charged particle cross sections were measured in terms of the rapidity and transverse momentum up to $p_t = 12$ GeV.

- Jet production: differential jet cross sections were measured as functions of the jet rapidity and transverse jet energy up to $E_t^{jet} = 40$ GeV.

The shapes of jets from γp collisions are very similar to those found in $\bar{p}p$ and $\gamma\gamma$ scattering. They show narrowing of the jet width with increasing transverse jet energy. The photoproduction jets and jets from $\bar{p}p$ and $\gamma\gamma$ collisions are related by a simple scaling law on the beam energies.

In the central rapidity region of the γp collision the underlying event energy next to the γp produced jets exceeds by far that expected from QCD calculations of a single hard parton-parton scattering process per event. Since the E_t^{jet} spectrum is falling so steeply, differences in the underlying event energy have a large influence on the jet cross sections. To gain information on the partonic scattering process from a comparison between the measured and calculated inclusive jet cross sections, the underlying event energy has to be taken into account.

To understand the relation between the measured jet cross sections and the underlying event, detailed studies of the transverse energy flow at large E_t in the photoproduction events were made, with special emphasis on the additional energy seen in the data:

- The differential transverse energy cross section shows a high E_t tail, as expected from hard scattering processes.

- The maximum transverse energy flow is observed in the central rapidity region of the γp collision ($\eta_{\gamma p} = 0$).

- The energy deposits in the central γp collision region ($\eta_{\gamma p} = 0$) are weakly correlated with the other energy depositions in the event.

- The transverse energy density at $\eta_{\gamma p} = 0$ outside of jets increases with decreasing fractional parton energies x_γ from the level of deep inelastic ep scattering events (direct γp processes) to the level observed in jet events of $\overline{p}p$ collisions.

These distributions are not described by models which calculate the exclusive final state from one hard parton–parton scattering process per event. A natural explanation for the observed transverse energy distributions are multiple parton interactions with up to three interactions on average per event. The γp results complement the measurement of double parton scattering processes, reported by $\overline{p}p$ experiments.

Basic QCD predictions were confirmed by the data:

- The direct interactions of quasi-real photons with protons have been confirmed by studying the 2-jet distribution of the fractional energy x_γ of the parton from the photon.
- The presence of resolved photon–proton processes was shown by the observation of the photon remnant.
- The distributions of the parton scattering angle in direct and resolved photon processes were found to be different, and are correctly predicted by QCD.
- The presence of higher order QCD effects were shown by the transverse energy imbalance in di-jet events and by the observation of multi-jet events.

Distributions of the partons from the photon were analysed:

- The distribution of the intrinsic transverse momentum k_t^γ of the partons from the photon was found to be harder than that of hadrons.
- Measurements of the single inclusive jet cross sections and the di-jet cross sections at large x_γ provide access to the extraction of information on the quark distributions of the photon at $x_\gamma \approx 1$.
- At small x_γ, measurements of di-jet production resulted in the first measurement of the leading order gluon distribution in the photon in the range $0.04 < x_\gamma < 1$ at a scale $\langle p_t^2 \rangle = 75$ GeV^2.

The results, reviewed in this paper, can be understood as a first successful round of high-E_t photoproduction analyses at HERA. Both experiments have delivered complementary results according to the strength of their detectors: the H1 experiment used the fine granularity calorimeter in the central rapidity region of the γp collision to study the effects of multiple parton interactions and the small x_γ parton content of the photon. The ZEUS experiment used the uniform coverage of the photon fragmentation region to study the photon remnant, direct photon interactions and the resolved photon processes at large parton fractional energies $x_\gamma \approx 1$.

Prospects: high energy photon interactions

This year, at LEP, electrons and positrons will be collided at center of mass energies up to $\sqrt{s_{ee}} = 190$ GeV (LEP2). Two-photon physics will be studied at CM energies up to $\sqrt{s_{\gamma\gamma}} = 100$ GeV [AUR-96]. The measurements of F_2^γ will then cover the large kinematical region $10^{-4} < x_\gamma < 1$ at scales between $3 < Q^2 < 10^3$ GeV^2. Within the next few years, the accuracy of these measurements is expected to be at the level of a few percent. The gluon will be studied in jet events in the region around $x_\gamma = 0.1$ at scales above $p_t^2 = 25$ GeV^2. Charm production may extend the region down to $x_\gamma = 10^{-3}$. New information will be obtained on the parton content of virtual photons. LEP2 also gives access to detailed measurements of the triple boson vertex γWW [GOU-96].

At HERA the integrated luminosity is expected to increase by $1-2$ orders of magnitude within the next few years. Cross section measurements with a statistical precision of a few percent are possible, e.g., for charged particles at high transverse momenta and for jets. An improved understanding of the detector effects is being achieved for such precision measurements. These data will allow the extraction of accurate NLO parton distributions of the photon (e.g. [BIN-96B]).

Studies of the parton distributions of virtual photons have recently been started [ZEU-95F] and are expected to shed new light on the transition region between photoproduction and deep inelastic lepton–proton scattering. Furthermore, the analysis of diffractive hard scattering processes revealed parton structure which can be assigned to the Pomeron (e.g. [H1-95C]). With the knowledge of the parton content in the photon already achieved, diffractive hard photoproduction processes provide a unique way of studying the gluon content of the Pomeron (e.g. [ZEU-95G]).

The next generation photon facility is already a very active field of experimental research and theoretical studies [MIL-95]: linear colliders will operate in ee, $e\gamma$, or $\gamma\gamma$ collision modes at center of mass energies between top–anti-top quark production and $\sqrt{s} = 2000$ GeV. They will act as clean W factories, and provide access to the very low x_γ parton content of the photon at high Q^2. If the Higgs boson is found in the few hundred GeV region, then the photon collider is an ideal place to measure its properties in order to confirm the standard model, or find new physics.

Acknowlegements

I wish to thank very much F. Eisele and Ch. Berger for numerous fruitful discussions on the interpretation of the photoproduction data and the analysis strategy. I thank all members of the H1 and ZEUS photoproduction groups for many important contributions. Special thanks go to M. Arpagaus, A. Buniatian, M. Colombo, A. DeRoeck, M. Gebauer, W. Hoprich, H. Hufnagel, R. Kaschowitz, G. Knies, H. Kolanoski, S. Levonian, P.O. Meyer, P. Pfeiffenschneider, H. Rick, A. Rostovtsev, C. Schwanenberger, U. Siewert, M. Steenbock, and W. Walkowiak. I have benefited from interesting discussions with P. Aurenche, J. Binnewies, J. Chyla, B. Kniehl, G. Kramer, S.G. Salesch, T. Sjöstrand, and A. Vogt. For constructive comments on this paper I thank S. Egli, F. Eisele, S. Maxfield, P. Schleper, G. Schuler, S. Söldner-Rembold and M. Werner. I am indebted to S. Maxfield also for the English corrections.

References

[ABR-91] H. Abramowicz, K. Charchula, A. Levy, Phys. Lett. B269 (1991) 458

[AFS-83] AFS Collab., T. Akesson et al., Phys. Lett. B128 (1983) 354

[AFS-87] AFS Collab., T. Akesson et al., Z. Phys. C34 (1987) 163

[AMY-94] AMY Collab. B.J. Kim, et al., Phys. Lett. B325 (1994) 248

[AUR-92A] P. Aurenche et al., Phys. Rev. D45 (1992) 92

[AUR-92B] P. Aurenche et al., Z. Phys. C56 (1992) 589

[AUR-94] P. Aurenche, J.P. Guillet and M. Fontannaz, Phys. Lett. B338 (1994) 98

[AUR-95] P. Aurenche, private communications

[AUR-96] P. Aurenche, G.A. Schuler, et al., '$\gamma\gamma$ Physics', in physics at LEP2, eds. G. Altarelli, T. Sjöstrand and F. Zwirner, CERN 96-01 (yellow report), hep-ph-9601317 (1996)

[BAU-78] T.H. Bauer, et al., Rev. Mod. Phys. 50 (1978) 261, Rev. Mod. Phys. 51 (1979) 407

[BAW-89] A.C. Bawa, W.J. Stirling, J. Phys. G15 (1989) 1339

[BER-83] Ch. Berger, PITHA 83/22 (1983), 'Int. Symp. on Lepton Photon Interactions', Ithaca, N.Y., -Publ. in Lepton/Photon Symp. (1983) 376

[BAL-88] A. Baldini, et al., Landolt-Börnstein's New Series I/12B (1988) 345

[BER-87] Ch. Berger and W. Wagner, Phys. Rep. 146 (1987) 1

[BIN-95] J. Binnewies, B.A. Kniehl and G. Kramer, Phys. Rev. D52 (1995) 4947

[BIN-96A] J. Binnewies, B.A. Kniehl, private communications

[BIN-96B] J. Binnewies, et al., to be published in the proc. of the workshop 'Future physics at HERA', Hamburg (1996)

[BLO-84] V. Blobel, DESY 84-118 (1984), Proc. of the 1984 CERN School of Computing, Aiguablava (Spain), CERN (1985)

[BOD-94] D. Bödeker, G. Kramer, S.G. Salesch, Z. Phys. C63 (1994) 471

[BOP-94A] F.W. Bopp et al., Phys. Rev. D49 (1994) 3236

[BOP-94B] F.W. Bopp et al., Comp. Phys. Commun. 83 (1994) 107

[BRO-79] S.J. Brodsky, et.al, Phys. Rev. D19 (1979) 1418

[BS-75] BS Collab., B. Alper et al., Nucl. Phys. B100 (1975) 237

[BUD-75] V.M. Budnev, et al., Phys. Rept. 15 (1975) 181

[BUN-95] A. Buniatian, PhD thesis, Hamburg, DESY internal report FH1K-95-04 (1995)

[BUT-95] J.M. Butterworth, et al., CERN-TH-95-83 (1995), Proc. of the conference 'PHOTON 95', Sheffield, England (1995) 175

[BUT-96] J.M. Butterworth, et al., to be published in the proc. of the workshop 'Future physics at HERA', Hamburg (1996)

[CAP-87] A. Capella et al., Phys. Rev. Lett. 58 (1987) 2015

[CAP-94] A. Capella et al., Phys. Rep. 236 (1994) 227

[CAP-74] P. Capiluppi et al., Nucl. Phys. B70 (1974) 1

[CAS-96] R. Cashmore, 39th Meeting of the DESY Physics Research Committee, Hamburg (1996)

[CAT-92] S. Catani, Yu.L. Dokshitser and B.R. Webber, Phys. Lett. B285 (1992) 291

[CDF-92] CDF Collab., F. Abe et al., Phys. Rev. D45 (1992) 2249

[CDF-93] CDF Collab., F. Abe, et al., Phys. Rev. D47 (1993) 4857

[CHE-75] M. Chen and P. Zerwas, Phys. Rev. D12 (1975) 187

[CHY-94] J. Chyla, Phys. Lett. B320 (1994) 186

[COL-84] P.D.B. Collins, A.D. Martin, 'Hadron interactions', Adam Hilger Ltd, Bristol, ISBN 0-85274-768-3 (1984)

[DAG-94] G. D'Agostini, Nucl. Instrum. Meth. A362 (1995) 487

[DEL-95] DELPHI Collab., P. Abreu, et al., Z. Phys. C69 (1996) 223

[DON-92] A. Donnachie, P.V. Landshoff, Phys. Lett. B296 (1992) 227

[DRE-85] M. Drees and K. Grassie, Z. Phys. C28 (1985) 451

[DRE-93] M. Drees, MAD-PH-797, Proc. of the '23rd Intern. Symp. Ultra-High Energy Multiparticle Phenomena', Aspen, Colorado (1993)

[DUK-82] D.W. Duke and J.F.Owens, Phys. Rev. D26 (1982) 1600

[E683-94] E683 Collab., D. Adams, et al., Phys. Rev. Lett. 72 (1994) 2337

[ENG-95] R. Engel, Z. Phys. C66 (1995) 203

[ENG-92] R. Engel et al., Phys. Rev. D46 (1992) 5192

[FIE-86] J.H. Field, F. Kapusta, L. Poggioli Phys. Lett. 181B (1986) 362

[FIE-87] J.H. Field, F. Kapusta, L. Poggioli Z. Phys. C 36 (1987) 121

[GLU-95A] M. Glück, E. Reya and A. Vogt, Z. Phys. C53 (1992) 127

[GLU-92B] M. Glück, E. Reya and A. Vogt, Z. Phys. C53 (1992) 651

[GLU-92C] M. Glück, E. Reya and A. Vogt, Phys. Rev. D46 (1992) 1973

[GLU-95] M. Glück, E. Reya, M. Stratmann, Phys. Rev. D51 (1995) 3220

[GOR-92] L.E. Gordon and J.K. Storrow, Z. Phys. C56 (1992) 307

[GOR-94] L.E. Gordon, J.K. Storrow, Phys. Lett. B291 (1994) 320

[GOR-95] L.E. Gordon and W. Vogelsang, Phys. Rev. D52 (1995) 58

[GOU-96] G. Gounaris, J.L. Kneur, D. Zeppenfeld, et al., 'Triple Gauge Boson Couplings', in physics at LEP2, eds. G. Altarelli, T. Sjöstrand and F. Zwirner, HEPPH-9601233 (1996)

[GRE-94] M. Greco, A. Vicini, Nucl. Phys. B415 (1994) 386

[GRI-71] V.N. Gribov and L.N. Lipatov, Yad. Fiz. 15 (1971) 781, (Sov. J. Nucl. Phys. 15 (1972) 438)

[H1-92] H1 Collab., T. Ahmed, et al., Phys. Lett. B297 (1992) 205

[H1-93B] H1 Collab., I. Abt, et al., Phys. Lett. B314 (1993) 436

[H1-94] H1 Collab., I. Abt, et al., Phys. Lett. B328 (1994) 176

[H1-95A] H1 Collab., T. Ahmed, et al. Nucl. Phys. B435 (1995) 3

[H1-95B] H1 Collab., T. Ahmed, et al., Nucl. Phys. B445 (1995) 195

[H1-95C] H1 Collab., T. Ahmed, et al., Phys. Lett. B348 (1995) 681

[H1-95D] H1 Collab., S. Aid, et al., Phys. Lett. B358 (1995) 412

[H1-95E] H1 Collab., S. Aid, et al., Z. Phys. C69 (1995) 27

[H1-96A] H1 Collab., S. Aid, et al., Z. Phys. C70 (1996) 17

[H1-96B] H1 Collab., I. Abt, et al., internal report DESY-96-01 (1996)

[HAG-95] K. Hagiwara, T. Izubuchi, M. Tanaka and I. Watanabe, Phys. Rev. D51 (1995) 3197

[HOP-95] W. Hoprich, diploma thesis, Heidelberg (1995)

[HOY-95] P. Hoyer, NORDITA-95-65-P (1995), Workshop on 'Deep Inelastic Scattering and QCD', Paris, France (1995)

[HUT-90] J. E. Huth et al., Fermilab-Conf-90/249-E (1990)

[HUF-95] H. Hufnagel, PhD thesis, Heidelberg (1994)

[KAP-89] F. Kapusta, Z. Phys. C42 (1989) 225

[KEN-96] B. Kennedy, private communication (1996)

[KLA-95A] M. Klasen, G. Kramer and S.G. Salesch, Z. Phys. C68 (1995) 113

[KLA-95B] M. Klasen and G. Kramer, DESY-95-159 (1995)

[KNI-94] B.A. Kniehl and G. Kramer, Z. Phys. C62 (1994) 53

[KNI-96] B.A. Kniehl, private communications

[KOL-84] H. Kolanoski, 'Two Photon Physics at e+e- Storage Rings' Publ. Springer Tracts in Mod. Phys. 105 (1984) 187

[KOL-87] H. Kolanoski and P. Zerwas, DESY-87-175 (1987), 'High Energy Electron-Postiron Physics', Ed. A. Ali and P. Söding, Singapore, Singapore: World Scientific (1988)

[KRA-94A] G. Kramer, S.G. Salesch, Z. Phys. C61 (1994) 277

[KRA-94B] G. Kramer and S.G. Salesch, Phys. Lett. B333 (1994) 519

[KRA-95] G. Kramer, private communications

[LEV-92] A. Levy, 'Photoproduction at HERA', DESY Academic Training Program (1992)

[MAR-84] G. Marchesini and B.R. Webber, Nucl. Phys. B238 (1984) 1

[MAR-88A] G. Marchesini and B.R. Webber, Nucl. Phys. B310 (1988) 461

[MAR-88B] G. Marchesini and B.R. Webber, Phys. Rev. D38 (1988) 3419

[MAR-92] G. Marchesini, et al., Comput. Phys. Commun. 67 (1992) 465

[MIL-95] D.J. Miller, DESY 95-183 (1995)

[NA14-86] NA14 Collaboration, E. Auge, et al., Phys. Lett. 168B (1986) 163

[OME-89] OMEGA γ Collab., R.J. Apsimon, et al., Z. Phys. C43 (1989) 63

[OWE-95] J. Owens, private communications (1996)

[PAU-91] E. Paul, DESY-92-026 (1992), 'Multiparticle Dynamics', Wuhan, China (1991) 267

[PFE-94] P. Pfeiffenschneider, diploma thesis, Aachen (1994)

[PLO-93] H. Plothow-Besch, Comput. Phys. Commun. 75 (1993) 396

[RIC-96] H. Rick, PhD thesis, in preparation (1996)

[SAK-60] J.J.Sakurai, Ann. Phys. 11 (1960) 1

[SAL-93] S.G. Salesch, DESY-93-196 (1993)

[SAL-95] S.G. Salesch, Manual for NLO QCD program 'JETSAM', H1 internal note (1995)

[SCH-93] G.A. Schuler and T. Sjöstrand, Nucl. Phys. B407 (1993) 539

[SCH-94] G.A. Schuler and T. Sjöstrand, CERN-TH-7193-94 (1994), Proc. of the conference 'Two-Photon Physics from DAPHNE to LEP200 and Beyond', ed. F. Kapusta and J. Parisi, Singapore: World Scientific, Paris (1994)

[SCH-95] G.A. Schuler and T. Sjöstrand, Z. Phys. C68 (1995) 607

[SCH-96] G.A. Schuler and T. Sjöstrand, Phys. Lett. B in press, hep-ph/9601282 (1996)

[SCHW-95] C. Schwanenberger, diploma thesis, Heidelberg (1995)

[SJO-87A] T. Sjöstrand, M. Bengtsson, Comput. Phys. Commun. 43 (1987) 367

[SJO-87B] T. Sjöstrand and M. van Zijl, Phys. Rev. D36 (1987) 2019

[SJO-94] T. Sjöstrand, CERN-TH-6488 (1992), Comput. Phys. Commun. 82 (1994) 74

[SJO-96] T. Sjöstrand, J.K. Storrow, A. Vogt, LU-TP-96-5 (1996), to appear in the proc. of the 'Durham Workshop on HERA Physics', Durham, England (1995)

[STE-96] M. Steenbock, PhD thesis, in preparation (1996)

[TOP-93] TOPAZ Collab., H. Hayashii, et al., Phys. Lett. B314 (1993) 149

[TOP-94A] TOPAZ Collab., K. Muramatsu, et al. Phys. Lett. B332 (1994) 477

[TOP-94B] TOPAZ Collaboration, R. Enomoto, et al., Phys. Rev. D50 (1994) 1879

[TPC-84] TPC/2γ Collab., M.P. Cain, et al. Phys. Lett. 147B (1984) 232

[TPC-87] TPC/2γ Collab., H. Aihara, et. al, Z. Phys. C34 (1987) 1,
Phys. Rev. Lett. 58 (1987) 97

[UA1-83] UA1 Collab., G. Arnison, et al., Phys. Lett. B132 (1983) 214

[UA1-87] UA1 Collab., C. Albajar et al., Z. Phys. C36 (1987) 33

[UA1-88] UA1 Collab., C. Albajar, et al., Nucl. Phys. B309 (1988) 405

[UA1-90] UA1 Collab., C. Albajar, et al., Nucl. Phys. B335 (1990) 261

[UA1-95] UA1 Collab., G. Bocquet, et al., CERN-PPE / 95-168 (1995)

[UA2-91] UA2 Collab., J.Alitti et.al. Phys. Lett. B268 (1991) 145

[VOG-94] A. Vogt, LMU-11-94 (1994), Proc. of workshop 'Two-Photon Physics at LEP and HERA', Ed. G. Jarlskog and L. Jönnson, ISBN 91-630-2886-7, Lund, Sweden (1994) 141

[WAR-94] OPAL Collab., J. Ward, Proc. of the conference 'Two-Photon Physics from DAPHNE to LEP200 and Beyond', ed. F. Kapusta and J. Parisi, Singapore: World Scientific, Paris (1994)

[WEB-84] B.R. Webber, Nucl. Phys. B238 (1984) 492

[WEI-34] C.F. von Weizsäcker, Z. Phys. 88 (1934) 612

[WIL-35] E.J. Williams, Kgl. Danske Vidensk. Selskab. Mat.-Fiz. Medd. 13 N4 (1935)

[WIT-77] E. Witten, Nucl. Phys. B120 (1977) 189

[ZEU-92] ZEUS Collab., M. Derrick, et al. Phys. Lett. B297 (1992) 404

[ZEU-93] ZEUS Collab., ZEUS internal note (1993)

[ZEU-94A] ZEUS Collab., M. Derrick, et al., Z. Phys. C63 (1994) 391

[ZEU-94B] ZEUS Collab., M. Derrick, et al., Phys. Lett. B322 (1994) 287

[ZEU-95A] ZEUS Collab., M. Derrick, et al., Phys. Lett. B342 (1995) 417

[ZEU-95B] ZEUS Collab., M. Derrick, et al., Phys. Lett. B346 (1995) 399

[ZEU-95C] ZEUS Collab., M. Derrick, et al., Phys. Lett. B348 (1995) 665

[ZEU-95D] ZEUS Collab., M. Derrick, et al., Phys. Lett. B354 (1995) 163

[ZEU-95E] ZEUS Collab., M. Derrick, et al., Z. Phys. C67 (1995) 227

[ZEU-95F] ZEUS Collab., M. Derrick, et al., Int. Europhys. Conf. on High Energy Physics, contributed paper EPS-0384, Brussels (1995)

[ZEU-95G] ZEUS Collaboration, M. Derrick, et al., Phys. Lett. B356 (1995) 129

Index